THE UNIVERSITY OF
WARWICK

Library Declaration and Deposit Agreement

1. STUDENT DETAILS

Please complete the following:

Full name: ………………………………………………………………………………………….

University ID number: ………………………………………………………………………….

2. THESIS DEPOSIT

2.1 I understand that under my registration at the University, I am required to deposit my thesis with the University in BOTH hard copy and in digital format. The digital version should normally be saved as a single pdf file.

2.2 The hard copy will be housed in the University Library. The digital version will be deposited in the University's Institutional Repository (WRAP). Unless otherwise indicated (see 2.3 below) this will be made openly accessible on the Internet and will be supplied to the British Library to be made available online via its Electronic Theses Online Service (EThOS) service.
[At present, theses submitted for a Master's degree by Research (MA, MSc, LLM, MS or MMedSci) are not being deposited in WRAP and not being made available via EthOS. This may change in future.]

2.3 In exceptional circumstances, the Chair of the Board of Graduate Studies may grant permission for an embargo to be placed on public access to the hard copy thesis for a limited period. It is also possible to apply separately for an embargo on the digital version. (Further information is available in the *Guide to Examinations for Higher Degrees by Research*.)

2.4 *If you are depositing a thesis for a Master's degree by Research, please complete section (a) below. For all other research degrees, please complete both sections (a) and (b) below:*

(a)   Hard Copy

        I hereby deposit a hard copy of my thesis in the University Library to be made publicly available to readers (please delete as appropriate) EITHER immediately OR after an embargo period of ………..................... months/years as agreed by the Chair of the Board of Graduate Studies.

        I agree that my thesis may be photocopied.   YES / NO (*Please delete as appropriate*)

(b)   Digital Copy

        I hereby deposit a digital copy of my thesis to be held in WRAP and made available via EThOS.

        Please choose one of the following options:

        EITHER   My thesis can be made publicly available online.   YES / NO (*Please delete as appropriate*)

        OR   My thesis can be made publicly available only after…..[date] (Please give date)
                                                                YES / NO (*Please delete as appropriate*)

        OR   My full thesis cannot be made publicly available online but I am submitting a   separately identified   additional, abridged version that can be made available online.
                                                                YES / NO (*Please delete as appropriate*)

        OR   My thesis cannot be made publicly available online.   YES / NO (*Please delete as appropriate*)

3. **GRANTING OF NON-EXCLUSIVE RIGHTS**

Whether I deposit my Work personally or through an assistant or other agent, I agree to the following:

Rights granted to the University of Warwick and the British Library and the user of the thesis through this agreement are non-exclusive. I retain all rights in the thesis in its present version or future versions. I agree that the institutional repository administrators and the British Library or their agents may, without changing content, digitise and migrate the thesis to any medium or format for the purpose of future preservation and accessibility.

4. **DECLARATIONS**

(a) I DECLARE THAT:

- I am the author and owner of the copyright in the thesis and/or I have the authority of the authors and owners of the copyright in the thesis to make this agreement. Reproduction of any part of this thesis for teaching or in academic or other forms of publication is subject to the normal limitations on the use of copyrighted materials and to the proper and full acknowledgement of its source.

- The digital version of the thesis I am supplying is the same version as the final, hard-bound copy submitted in completion of my degree, once any minor corrections have been completed.

- I have exercised reasonable care to ensure that the thesis is original, and does not to the best of my knowledge break any UK law or other Intellectual Property Right, or contain any confidential material.

- I understand that, through the medium of the Internet, files will be available to automated agents, and may be searched and copied by, for example, text mining and plagiarism detection software.

(b) IF I HAVE AGREED (in Section 2 above) TO MAKE MY THESIS PUBLICLY AVAILABLE DIGITALLY, I ALSO DECLARE THAT:

- I grant the University of Warwick and the British Library a licence to make available on the Internet the thesis in digitised format through the Institutional Repository and through the British Library via the EThOS service.

- If my thesis does include any substantial subsidiary material owned by third-party copyright holders, I have sought and obtained permission to include it in any version of my thesis available in digital format and that this permission encompasses the rights that I have granted to the University of Warwick and to the British Library.

5. **LEGAL INFRINGEMENTS**

I understand that neither the University of Warwick nor the British Library have any obligation to take legal action on behalf of myself, or other rights holders, in the event of infringement of intellectual property rights, breach of contract or of any other right, in the thesis.

Please sign this agreement and return it to the Graduate School Office when you submit your thesis.

Student's signature: ....……… Date: ....
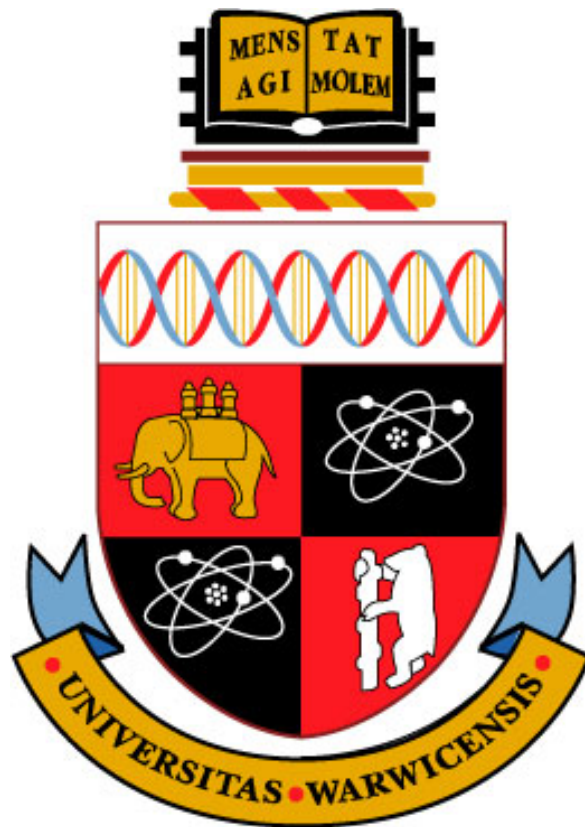
Optical Wireless Data Transfer for Rotor Detection and Diagnostics

by

Peng Huang

A thesis submitted in partial fulfilment of the requirements for the degree of Doctor of Philosophy in Engineering

School of Engineering

University of Warwick

May, 2012

Table of Contents

Acknowledgements

First and foremost, I would like extend my sincere thanks to my supervisor, Dr. Daciana Iliescu. It has been an honour to be her Ph.D student. I appreciate all her contributions to time, idea, patience, guidance and other helps throughout my PhD course. The joy and enthusiasm she has for her research was contagious and motivational for me, even during tough times in the Ph.D pursuit. Without her directions, the thesis would not have reached the present form.

I gratefully acknowledge the invaluable help of my second supervisor, Dr. Mark Leeson. His illuminating instructions always motivated me to develop further the ideas. With his enthusiasm in this field, his inspiration, and his great efforts to explain things clearly and simply, he helped to make mathematics fun for me. Throughout my thesis-writing period, he provided encouragement, sound advice, good teaching, good company, and lots of practical ideas. I would have been lost without him.

I would like thank my former supervisor, Prof. Evor Hines for his helpful advices in the early stage of the research. In addition, I wish to thank the secretaries and technical assistants in the engineering department, for helping the departments to run smoothly and for assisting me in many different ways. Kerrie, Phillips and Ian deserve special mention.

I wish to thanks my entire extended family for providing a loving environment for me. I am gratefully for my parents raised me with a love of science and supported me in all my pursuits.

I wish to thank my best friends, Paul, Ivan and Zheng, for helping me go through the difficult times, and for all the emotional support, camaraderie, entertainment, and caring they provided.

Last but not least, special thanks to the one that is always on my side and give me support, encouragement and joy though out the past four years, Yanqing, without her it would have been much harder to finish a Ph.D.

Declaration

This thesis is presented in accordance with the regulations for the degree of Doctor of Philosophy. All work reported has been carried out by the author except where stated otherwise, including the production of this document. No part of this work has been previously submitted to the University of Warwick or any other academic institution for admission to a higher degree.

Peng Huang

Abbreviations

3 D – Three dimensional

AC – Alternating current

ADC – Analogue to digital convertor

AGC – Automatic gain control

APD – Avalanche photodiode

BER – Bit error rate

CCTL – Capture/compare control register

CCR – Capture/compare register

CTL – Control register

CWR – Communication window ratio

DC – Direct current

DDI – Dual detection identification

DPIM – Digital pulse interval modulation

DR – Data receiver

DSP – Digital signal processor

DT – Data transmitter

EAM – Electroabsorption Modulator

EM – Electromagnetic

EMI – Electromagnetic interference

FEM – Finite element method

FIR – Fast Infrared

FM – Frequency modulation

FPGA – Field-program gate array

FSK – Frequency shift keying

GBW – Gain bandwidth product

IAS – Information Access Service

IM/DD – Intensity modulation and direct detection

IR – Infra-red

IrCOMM – Infrared Communication

IrLMP – Infrared Link Access Protocol

ISI – Inter-symbol interference

LED – Light emitted diode

LOS – Line of sight

MGF – Moment generating function

MIR – Medium Infrared

MPPM – Multi pulse position modulation

MZM – Mach–Zehnder modulator

OBEX – Object Exchange

OFDM – Orthogonal frequency-division multiplexing

OOK – On-off keying

OPPM – Overlapped pulse position modulation

Op-amp – Operational amplifier

OW – Optical wireless

PPM – Pulse position modulation

PSK – Phase shift keying

p-p – peak to peak

RF – Radio frequency

RFID – Radio frequency identification

RZI-OOK – Return-to-zero inverted on-off keying

SIR – Serial Infrared

TIA – Transimpedance amplifier

UART – Universal Asynchronous Receiver/Transmitter

VGA – Variable gain amplifier

List of Figures

List of Tables

List of Publications

Huang, P., Iliescu D.D., Leeson, M.S. and Hines, E.L. *Optical Wireless for Data Transfer in a Periodic Fast Fading Channel.* (To be submitted)

Abstract

A special application of optical wireless data transfer, namely on-line monitoring and diagnostic of rotors in turbines and engines, has been considered in this thesis. In this application, to maintain line of sight, i.e. data transfer, between a sensor placed on a rotating component inside the turbine and a monitoring point placed in a fixed position outside the turbine, a periodic fast fading channel is generated, which gives the transceivers more flexibility regarding their mounting location. The communication in such a channel is affected by the intermittency and variation of the signal power, which produces a unique channel condition that influences the performance of the optical transceiver.

To investigate the channel condition and the error rate of the periodic fast fading channel with signal fluctuation, a model is developed to simulate the optical channel by considering the variation of signal power as a result of the change in the relative position of the photodiode with respect to the Lambertian radiation pattern of the LED, in a simplified linear geometry. The error rate is estimated using the Saddlepoint approximation on a specific threshold strategy. The results show that the channel can afford the sensor data transmission and the performance can be improved by modifying several parameters, such as geometrical distance, transmitter power and load resistor. Compared to a normal channel, a higher load resistor on the photodiode front end has the advantage of decreasing the noise level and increasing the data capacity in the fast fading channel. The analysis of the automatic gain control amplifier indicates that a higher load resistor needs a lower loop gain and from the model of the Transimpedance amplifier (TIA), the bandwidth extension from the amplifier is more significant for a higher resistor.

In addition to the theoretical model, an experimental setup is built to emulate the channel in practice. The degree of similarity between the experimental setup and the theoretical model of the channel is estimated from the comparison of the generated

communication windows. Since it has been found that differences exist in the duration of the communication window and the variation of the signal power, scaling factors to ensure their compatibility have been derived. Transceiver hardware which implemented the modelled functionality has been developed and a protocol to establish the communication with the required error rate has been proposed. Using the hardware implementation, a detection method for both rising and falling edges of the signal pulses and a threshold strategy have been demonstrated. The device power consumption is also estimated.

What is more, the electromagnetic environment of a squirrel cage motor is simulated using the finite element method to investigate the interference and the possibility of providing power to the IR communication devices using power scavenging.

In the conclusion, the key findings of the thesis are summarised. A solution is proposed for sensor data transfer using an optical channel for rotor monitoring applications, which involves the design of the IR transceiver, the implementation of the developed protocol and the power consumption estimation.

1 Introduction

This thesis presents the theoretical analysis and practical implementation of a particular case of optical wireless (OW) communication channel, termed the periodic fast fading channel, in which the Line-of-sight (LOS) channel between a pair of transceivers is not persistent but appears and disappears periodically, caused by the rotation of one transceiver relative to the other.

Typically, OW communications transfer signals in continuous LOS channels. However, in some cases sustaining the LOS channel is difficult, especially for applications in which the transceivers are in relative motion. One type of applications in which such a situation arises is direct on-line monitoring and diagnostic of rotors in generators and motors. In such applications, as wired communication is extremely restrictive, wireless communication based on radio frequency (RF) signals has been attempted. Compared to RF signals, optical signals have the advantage of reduced susceptibility to Electromagnetic Interference (EMI) from the strong Electromagnetic (EM) field present inside the generator or motor but suffer from the lack of a continuous and reliable LOS channel. For these conditions, it is proposed that, if the LOS channel is present intermittently, optical communication is still possible and desirable, therefore a suitable solution should be found.

In the specific case of a generator in service, a point on the spinning rotor appears in the same position repeatedly in each cycle of rotation. Thus, if the optical transceiver placed on the rotor is pre-aligned with a transceiver in a fixed position, such as on the stator or the casing of the generator, the transceivers can establish a LOS channel when the position of alignment re-occurs in each cycle. In such a condition, the LOS channel is limited to an extremely short period of time in each cycle of rotation.

1.1   System Description

The geometry of the system that creates the non-continuous LOS channel is described schematically in Fig. 1.1.1. Two transceiver devices are necessary to transfer the sensor data from the rotor, each named according to its main function as the Data Transmitter (DT) and the Data Receiver (DR). The DT, located on the rotor, collects and transmits data from the sensor and the DR, located on the stator, receives the data from the DT for further analysis. When the DT is rotated to the position of alignment in each rotation cycle, as shown in Fig. 1.1.1, a LOS channel can be established for a short period of time when both optical receivers on the DT and the DR are located in the of each other's optical transmitters' radiation patterns, as shown in Fig. 1.1.2. The communication time in a cycle is determined mainly by the beam width of the optical transmitter. The analysis of the effects of location and geometry on the communication parameters will be discussed in section 3.1 and detailed further in Appendix I.
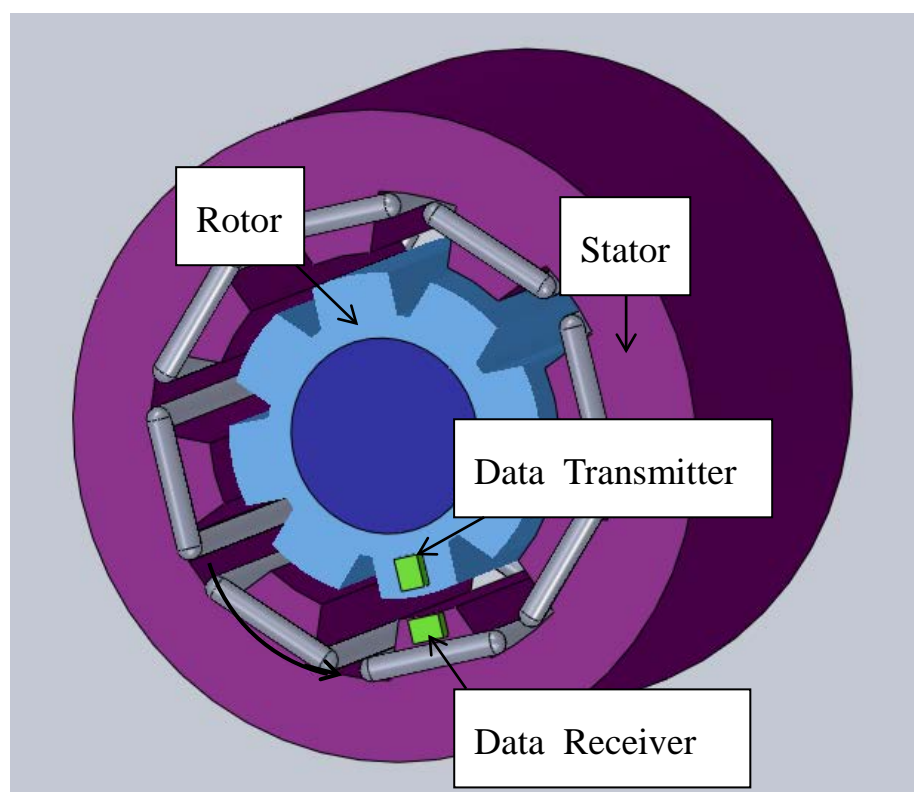
Fig. 1.1.1 The geometry of the intermittent fast fading channel
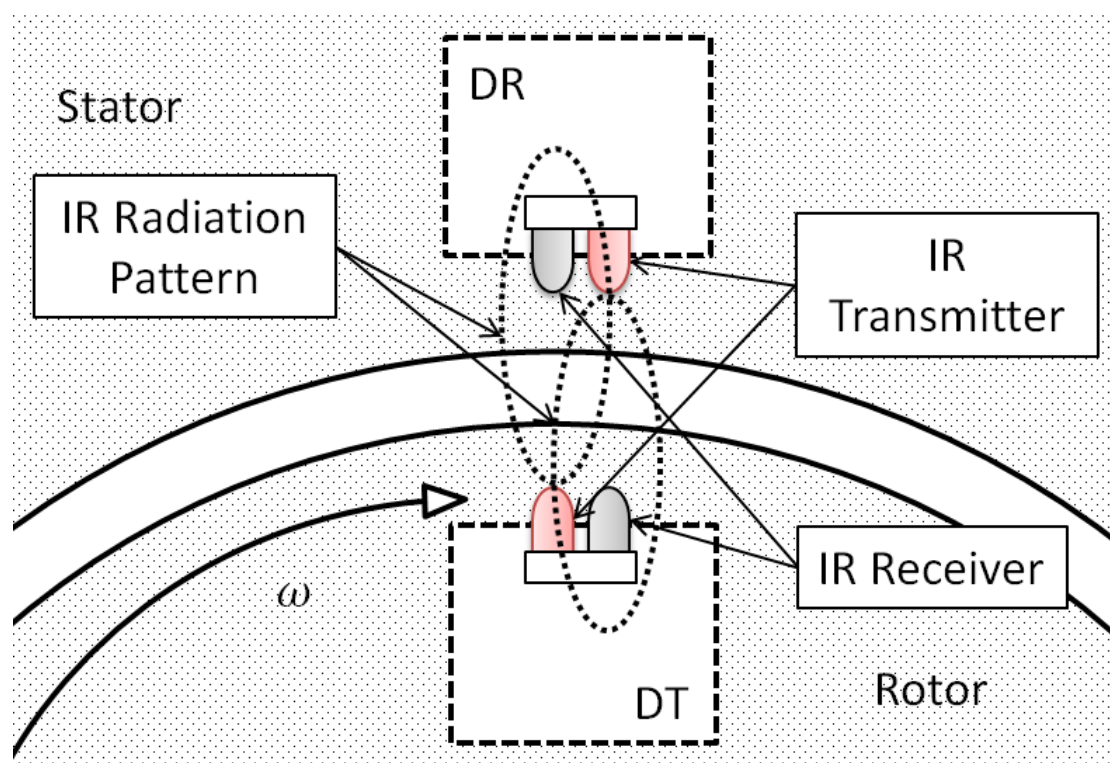
Fig. 1.1.2 The established LOS channel.

The dependence of the received signal power on the geometric parameters of the optical transmitter generates a unique signal condition in the periodic fast fading channel, compared to the typical optical channel in which the received signal power is either constant or regulated. The rotation geometry impacts the received optical power in the following two aspects:

1. When the optical transmitter and receiver are mounted in fixed positions on the rotor and, respectively, the stator, the time proportion of the communication relative to the rotation period remains constant. As the rotor accelerates and the rotation speed increases, the actual communication time becomes shorter. If the increased rotation speed results in a communication time that is insufficient for one frame of the data transfer, the communication cannot continue.

2. The beam divergence of the optical transmitter, especially for a Light Emitting Diode (LED), produces a radiation pattern in which the light intensity in a

specific location is determined by both angle and distance from the light source. As the DT approaches, then departs the DR, the variation of angle and distance between them introduces fluctuations in the signal power during the communication time.

In summary, the signal power condition determines the performance of the fast fading channel to a large extent.

What is more, since the DT has to be totally wireless due to the rotation, its power has to be supplied from a battery or scavenged from the surrounding environment and is, therefore, limited. The power efficiency of the DT should be taken into account when estimating its performance.

1.2   Thesis Structure

The thesis is organised as follows:

Chapter 2 provides the research background for the project. The chapter starts with an overview of the research and development of rotor monitoring and diagnostics techniques and states the contribution of the present project to this field. Further literature about Optical Wireless (OW) communication on fast fading channels is reviewed. In addition, the power condition of the DT device on the rotor is analysed and possible power supply and scavenging methods are introduced.

Chapter 3 includes the models that are developed to analyse the optical channel parameters and the signal processing options for the fast fading channel, using a simplified geometry. Performance and power efficiency parameters are derived from the simulation and a special threshold strategy is introduced to evaluate bit capacity of the channel for a specified error rate. The signal fluctuations are investigated and the corresponding performance of an Automatic Gain Controlled (AGC) amplifier is studied. Moreover, the influence of a Transimpedance Amplifier (TIA) on the bandwidth of the channel is presented.

Chapter 4 is based on an experimental demonstration of the proposed channel.

The rotating DT which creates the periodic optical channel is simulated in the experimental setup by a rotating a disc with a hole, which allows optical access for a small proportion of the disc's period of rotation. The difference between the experimental setup and the theoretical model is discussed and compared. A dedicated signal detection method is developed to predict the signal condition and the influence of the reduction in the modulation amplitude on the bit capacity is evaluated. The design of the communication devices, including hardware and software, is described. The channel performance results obtained from the experimental setup are discussed. At the end of the chapter, further developments based on the results will be proposed.

Chapter 5 includes a Finite Element Method (FEM) model using a stationary solver of a motor EM environment that investigates the interference and power harvesting from the EM source, in which the theory, design and results of the model are presented.

Chapter 6 is the conclusions of the thesis, providing the solution for the data transfer in the periodic fast fading channel. Further work is also described.

2 Background and Literature Review

2.1 On-line Rotor Monitoring and Diagnostics

The health of the rotor influences the performance of the motor or generator directly, therefore in current years, rotor monitoring and diagnostics received great interest from researchers. Due to the working condition of the rotor, sensor data for parameters such as temperature, current and voltage of the winding [1], cannot be easily transferred on-line. As a result, indirect monitoring methods that do not require detection on site or installation of detectors inside the machine have received significant attention. However, as RF and OW techniques are introduced for data transfer, direct monitoring and diagnostics have the advantages of real-time monitoring of rotor health, such as enhanced understanding of operating conditions and advanced warning if some operating limits are exceeded [2, 3].

2.1.1 Indirect Methods

Indirect rotor monitoring and diagnostics uses parameters from other easy access sources, such as current, voltage and resistance, to estimate the condition or defect of the rotor. Specific data analysis algorithms or modelling are necessary because the data does not indicate the rotor condition in a direct manner.

Current and voltage are the two most common references in rotor monitoring. One of the examples is the additive frequency component from the broken rotor bars to the current [4]. The related signal processing techniques for frequency analysis to detect the side band can vary depending on the mathematical operation [5, 6]. For a more accurate analysis that tolerates the disturbance from load and speed, the Vienna method has been investigated [7-9], in which two models, namely the current and the voltage model, shown in Fig. 2.1.1, are derived based on the space-phasor equations.

In the current model the rotor flux linkage $\underline{\lambda}_r$ is calculated from the stator current $\underline{i}_s$, the rotor reactance x_r and time constant τ_r, in which x_r and τ_r is derived from a fixed reference frame of the rotor and $\underline{i}_s$ is derived from measurement. The current model is used as reference. In the voltage model, the stator flux linkage $\underline{\lambda}_s$ is derived from stator current $\underline{i}_s$, stator voltage $\underline{v}_s$ and stator resistance r_s. As $\underline{i}_s$ and $\underline{v}_s$ of the voltage model are from measurement, the rotor faults affect the flux density and the flux linkage, therefore can be found by comparing to the current model.
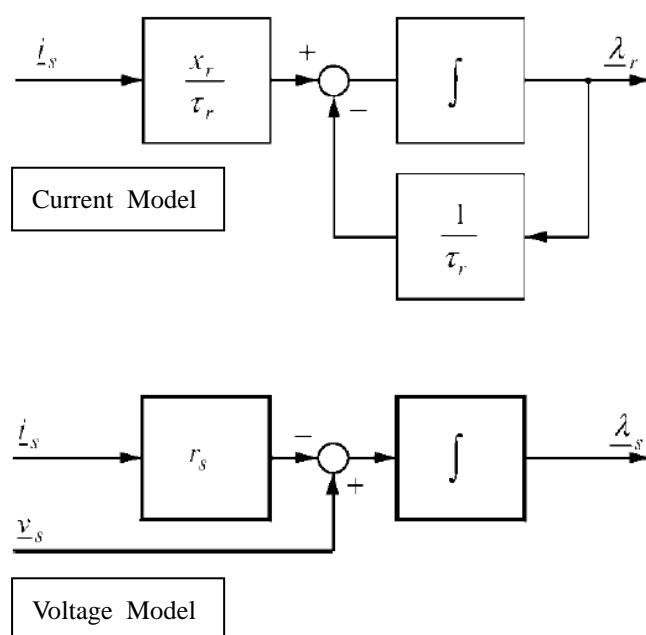
Adapted from [7]

Fig. 2.1.1 Current and Voltage Models of the Vienna Method

What is more, the rotor temperature can be estimated from the rotor resistance [10, 11], that can be formulated as:

$$R_2 = R_1 \frac{\theta_2 + k}{\theta_1 + k} \tag{2.1.1}$$

in which R_1 and R_2 are the resistances at temperatures (in degrees Celsius) θ_1 and respectively θ_2 and k is the temperature coefficient of the material. As some of the motors and generators are provided with cooling mechanisms, temperature models

include the effect from outer cooling by acquiring more parameters such as the stator current and voltage [12], or by combining measurements with parameter estimations [13]. Last but not least, a feedback based method by emitting acoustic waves for detecting friction faults that caused from vibrations can be found in [14].

Data from indirect rotor monitoring methods are usually derived and compared to a standard model that represents the normal condition, and a fault or defect is indicated if the data does not agree with the standard model. The monitoring algorithm can be implemented using standard computers or dedicated Digital Signal Processors (DSPs). The interface can be either local [15] or remote, such as over the Internet, realized by publishing the data acquisition server online [16]. Using computer assisted optimization design, the monitoring algorithm can be implemented on a Field-program Gate Array (FPGA) [17]. DSPs can be used for data processing either as signal interpreters for further processing [18] or as individual diagnostic systems [19]. Specific signal processing DSP chips, such as fuzzy logic [20] or discrete wavelet transform [17] can also be included. To add more intelligence and flexibility, artificial neutral networks have also been trained to detect rotor faults [21].

2.1.2   Direct Methods

Values of key parameters for rotor health can be acquired by sensors. With dedicated data transfer technology, the real time status of the operational rotor can be shown instantly with considerable accuracy. However, the difficulty of the direct monitoring using sensors is the implementation of data transfer from the rotating component to a component with no movement.

Compared to indirect methods, the number of monitoring parameters for direct methods is significantly reduced, for example in most cases, only one parameter (e.g. temperature) is needed. Current research shows great interests for temperature and vibration sensing [22-30]. In exceptional cases other parameters can also be measured. In [31] the rotor current is measured without sensors to diagnose the sparking of the rotor coils. In [32] a torque meter constructed by strain gauges offers

an easy setup that is mounted entirely on the shaft, with no other component mounted inside the machine frame on the rotor.

The data transfer technologies for direct rotor monitoring can be divided into three main categories, defined by the different signal carriers: contact, RF and optical. The rotor current measurement described in [31] uses slip rings to maintain metal contact between devices. A near field rotary transformer system is found in [33], which leaves a narrow air gap between the rotary and stationary modules of the antenna, therefore the power and electric signals are both transmitted without significant loss. RF communication is used for different applications, depending on the system configuration and required bandwidth. Rotor vibration sensor signals are directly modulated on RF signals, using a simple signal convertor [22]. A more general RF solution is summarized in Fig. 2.1.2, where the RF communication is performed by dedicated chips, which transform the sensor signals into RF signals that are specific to different protocols. Microcontrollers can be added to manage the data acquisition and conversion, therefore providing more options for the RF protocols (Route 1 and 2 in Fig. 2.1.2).
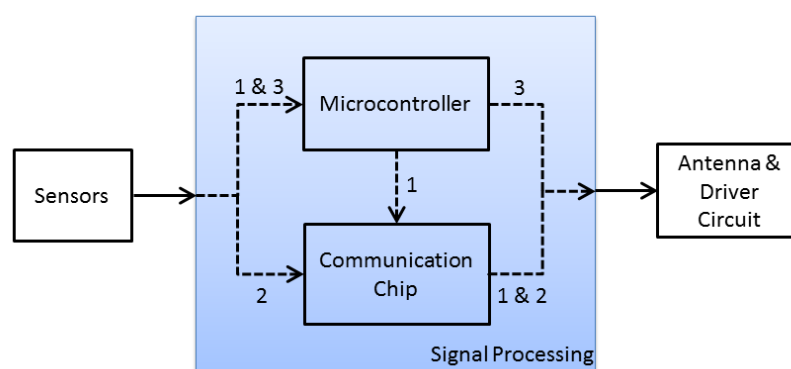
Fig. 2.1.2 A common RF solution for direct rotor monitoring. (Route 1: sensors → microcontroller → RF communication chip → antenna. Route 2: sensors → RF communication chip → antenna. Route 3: sensors → microcontroller → antenna.)

Examples of different techniques are the higher bandwidth ZigBee [23, 32] and WiFi [24] protocols, short range wireless Bluetooth [25] and RFID-S [26]. The influence of the EM field of the motor or generator on RF data transfer leads to more

power consumption and extra packet loss[27]. As a substitution, OW methods are used. The same configuration from Fig. 2.1.2 is also applied for data transfer using OW signals, where the LED and photodiode represent the optical antennas and the data transfer can be accomplished only by a microcontroller (route 3 in Fig. 2.1.2). Direct transmission on an infrared channel of digital signals from sensor data is demonstrated in [29], in which the received IR data needs to be re-formatted to adapt to the RS-232 interface. Differently, in [30] the IrDA Serial Infrared (SIR) protocol is introduced and the DR is not necessarily specially designed. In addition, an optical channel can be used for other purposes than data transfer, such as in a passive sensing application, presented in [34], in which the rotor temperature is detected by processing the optical fibre sensor reflection of the incoming optical signal.

The devices located on the rotor for contactless monitoring applications are completely isolated from the constant power supplies. Two power solutions presented in the literature have been reviewed in this section. Batteries of different kinds are stated in [22, 25, 27, 29, 32] as the power source. However, for some applications such as torque measurement [32], batteries cannot provide the solution for long-life power and power scavenging represents a better solution. Alternatively, wireless power supplies are described in [26, 28, 35], in which the power transformers convert and transmit power in AC coupling. The block diagram of the transformer demonstration from [35] is shown in Fig. 2.1.3.
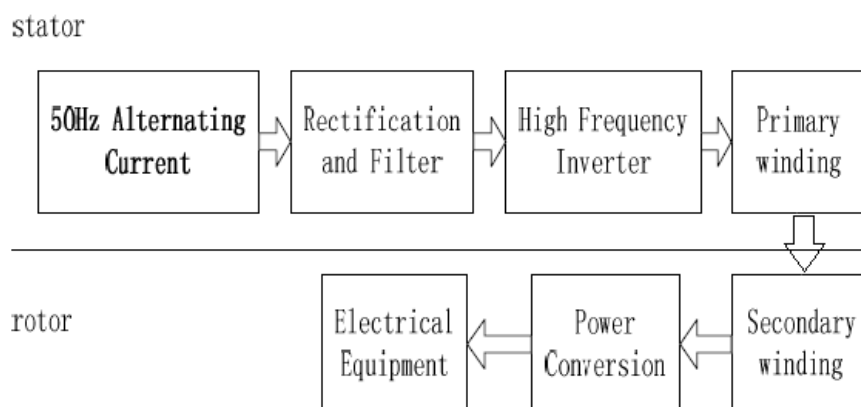
Adapted from [35]

Fig. 2.1.3 The block diagram of the power transformer.

In this diagram, the DC power supply of the device on the rotor is transferred and converted from the frequency raised power through two windings, from a normal 50 Hz supply. Analysis of the AC coupling power efficiency and corresponding simulation of a pair of ring shaped coupling coils is performed in [26]. The results indicate that with proper shielding, the power loss caused by eddy currents can be significantly reduced. Moreover, special design for low power consumption is required on the communication devices that uses wireless AC coupling power transfer in these cases, and from the literature, this technique does not appear in applications using OW transfer, which generates the uncertainty of whether the OW devices can sustain a long time transmission from an alternative power source other than using batteries.

Mounting locations of the wireless sensor data transfer devices using RF or OW on the rotor are restricted in order not to compromise the rotation. The location of the rings for power transfer of the RF data transfer device using AC coupling is discussed in [26]. The non-stop power supply is established by concentrically rotating one ring with the rotor. A similar problem exists in the OW applications when preserving the continuous optical LOS channel. Generally, constructing a constant link for power or optical signal between the device on the rotor and the one on the stator requires a special setup or positioning. In [29] and [30], the IR transmitter on the rotor is mounted on the shaft stub, as shown in Fig. 2.1.4

From [30]

Fig. 2.1.4 IR transmitter is mounted on rotor shaft stub. The IR LED and photodiode pair is placed on the shaft axis and the alignment is not disturbed even when the shaft is rotating.

Alternatively, the optical antenna with IR LED array is clamped around the shaft body [36], as shown in Fig. 2.1.5.
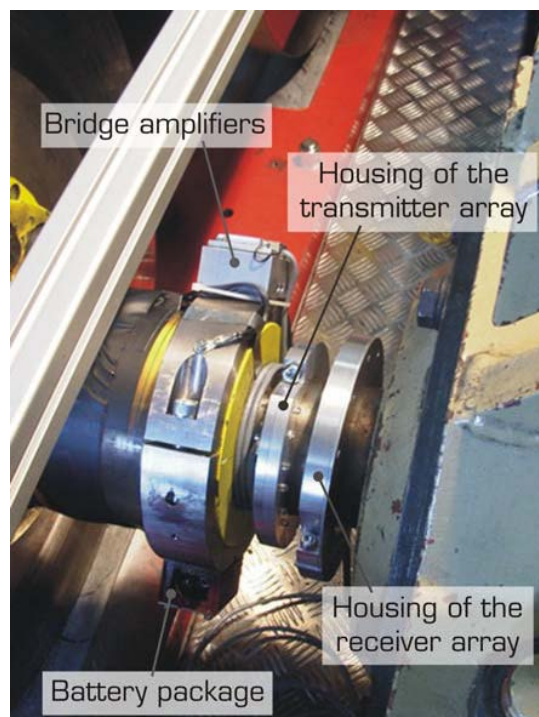
From [36]

Fig. 2.1.5 IR transmitter clamped on the shaft body. The transmitter ring and receiver ring produce a continuous link in the rotation circle.

2.1.3   Summary

Rotor monitoring and diagnostic methods, including the corresponding necessary parameters, modelling, data processing and transfer are presented in this section. Using indirect methods to detect broken bars and temperature share the advantage of no access to the interior of the machine, but needs more resource for data processing and modelling. For direct methods, temperature and torque sensing data are acquired and transmitted from a device on the rotor to a device in a fixed position. While wireless communication techniques, such as RF and OW, are introduced in the application. Problems with the power supply and LOS channel of OW are generated by the rotation of the DT device on the rotor. To solve these problems, limitations are

imposed on the mounting location of the devices, which involve AC coupling wireless power transfer technique for DT device on RF communication and continuous LOS channel on OW channel; batteries are used as the power supplies for most of the reviewed applications to overcome the problem of powering the device installed on the rotor.

2.2 Short Distance Wireless Infrared Communication

OW communication has been applied for short distance applications such as WLAN and other networks for indoor communications [37-40]. Some of the benefits of using OW instead of RF result from no RF frequency band occupation, freedom on the use of the spectrum without regulation and lower cost [41, 42]. Another benefit for the OW is the resistance to EMI for industrial applications in which the environmental EMI is strong [43] or close to a known EM field sources such as motor or generators [44-46]. The EMI influence on optical transceiver circuits has been investigated in [47, 48]. Successful industrial applications of OW have been described in section 2.1, with more examples of rotor health monitoring found in [36, 49, 50].

Long distance OW communications need to consider the environmental influences such as beam dispersion and attenuation due to the atmosphere [51]. The scatter effect from the atmosphere can be estimated using the model in [52]:

$$a_{scatt} \cong \frac{17}{S} \cdot \left(\frac{555}{\lambda}\right)^{0.195 \cdot S} \text{ (dB/km)} \qquad (2.2.1)$$

in which S is the human eye visibility, λ is the wavelength of the infrared signals.

In the short distance scenario, such as indoor communications, the scatter from (2.2.1) can be ignored for a communication distance of less than 1 m. There are two types of indoor channels: LOS and non-LOS, as shown in Fig. 2.2.1. The signal reception range from a non-LOS channel may be improved by reflecting the optical signals, but the loss from the reflection is also considerable. What is more, the loss of LED signal energy is proportional to the square of the distance, according to

Lambert's law, therefore significant [53, 54]. In consequence, LOS channels are preferred in practice, especially for applications using LED where the radiation angle is much wider than that of a laser diode.
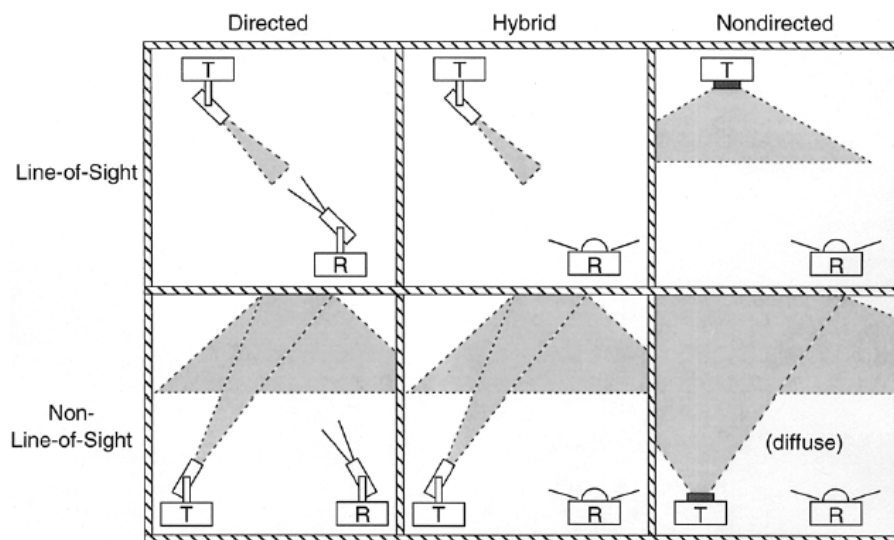
From [53]

Fig. 2.2.1 Indoor optical communication channels

2.2.1   Photodiode Signal Response

In an optical receiver where a P-i-N photodiode is the optical to electronic signal convertor, the bottleneck of the performance is from the diode capacitance that limits the bandwidth. Depending on the bias voltage, the response of a photodiode is different. In response to an optical signal, applying reverse bias to the photodiode produces a photoconductive current signal, while a photovoltaic voltage signal is generated with no bias.

A two-valley model of the photodiode photoconductive current response can be found in [55-61]. The equivalent circuit of a simplified model based on step function for the response of the pulse [55] is shown in Fig. 2.2.2.

The voltage $U(t)$ is given by:

$$U(t) = V_{CC} - RI(t) - RC\frac{dI}{dt} \qquad (2.2.2)$$

in which V_{CC} is the bias voltage, R is the load resistor and C is the diode capacitance, and the generated current from the photodiode $I(t)$ is mainly from photo current:

$$I = \frac{q\eta' P_R}{hf d_i}(v_n n + v_p p)$$ (2.2.3)

in which μ is the mobility of electrons and holes in the corresponding valley accordingly, n is the electron concentration and p is the hole concentration, V_d is the punch-through voltage, v_n and v_p are the velocities of electrons and holes:

$$v_{n,p} = \mu_{n,p}\left(\frac{U - V_d}{d_i}\right)$$ (2.2.4)

and η' is a coefficient from the photodiode quantum efficiency η:

$$\eta' = \frac{\eta}{(1 - e^{-\alpha d_i})}$$ (2.2.5)
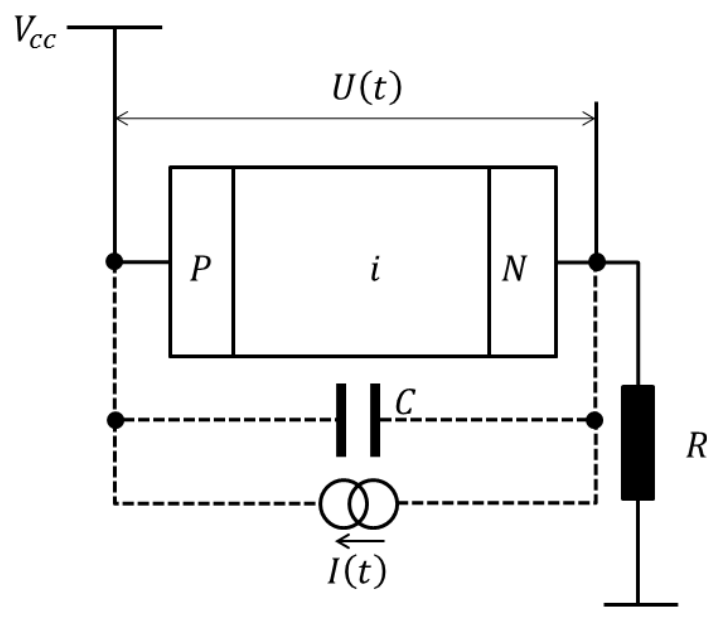
Adapted from [55]

Fig. 2.2.2 Equivalent circuit of the photodiode photoconductive model

In (2.2.5), d_i is the width of the i region of the P-i-N photodiode. In (2.2.4), n and p

of a pulse in the form of the step function $h(t - t_1) - h(t - t_2)$ is:

$$n(t) = \int_0^{d/v_n} [h(t_0 - t_1)$$
$$- h(t_0 - t_2)][1 - e^{-\alpha d_i} e^{\alpha v_n(t-t_0)}] d\, t_0 \tag{2.2.6}$$

$$p(t) = \int_0^{d/v_p} [h(t_0 - t_1)$$
$$- h(t_0 - t_2)][e^{\alpha v_p(t-t_0)} - e^{-\alpha d_i}] d\, t_0 \tag{2.2.7}$$

What is more, the photodiode photoconductive response in time $I(t)$ also includes the components of the displacement current. From this model, the expression for $I(t)$ can be simulated in software, which is based on the approximation of the electron and hole concentrations.

2.2.2   Noise Condition

Noise sources for short distance OW communication are mainly from the receiver front end, which produces Gaussian noise, shot noise and excess noise in general.

The noise from the electrical circuit of the photodiode front end is considered as thermal noise caused by the random thermally excited vibration of the charge carriers in a conductor, which exists in a conductor with a temperature above absolute zero [62, 63]. The thermal noise appears in any circuit component with resistance and can be evaluated in the Johnson–Nyquist noise model [64]. The available noise power is proportional to the bandwidth and temperature, which is:

$$P_n = kT_n \Delta f \tag{2.2.8}$$

in which $k = 1.38 \times 10^{-23}$ J/K is the Boltzmann's constant, T_n is the equivalent noise temperature and Δf is the noise bandwidth of the measuring system. The equivalent circuits are shown in Fig. 2.2.3, in which the noise is considered being the current source i_n in the Thevenin model or the voltage source U_n in the Norton model.
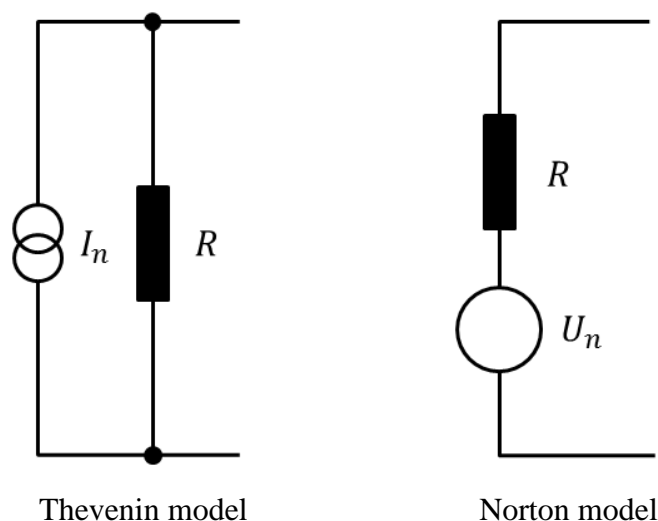
Adapted from [63]

Fig. 2.2.3 Thermal noise equivalent circuits

The corresponding current and voltage equations are:

$$i_n = \sqrt{\frac{4kT_n\Delta f}{R}} \tag{2.2.9}$$

$$U_n = \sqrt{4kT_nR\Delta f} \tag{2.2.10}$$

where R is the resistance. If the noise power per Herz is constant over the entire bandwidth, the thermal noise can be treated as 'white' noise. When the noise is approximated by a Gaussian distrubution, the variance σ^2 of the noise current is the product of the power spectral density S and the bit time T [65, 66]:

$$\sigma^2 = ST$$

$$= \frac{2kT_nT}{R} \qquad (2.2.11)$$

In signal processing, the noise is usually filtered and reduced. The filtered Gaussian noise is no longer white in spectrum. In this case, the power spectral density depends on the frequency response of the filter $H(f)$ [66]:

$$S = \int_0^{\Delta f} \frac{2kT_n|H(f)|^2}{R} df \qquad (2.2.12)$$

Another method to estimate the power spectral density is suggested in [67]. What is more, a transient noise model is discussed in [68] where the frequency dependent noise is included.

In addition, amplifiers introduce noise to the amplified signals. According to [69], the noise from the operational amplifier as pre-amplifier can be modelled as noise of 1/f characteristic that is given by the impedance frequency poles of the photodiode and amplifier circuit network. Various models are found to estimate the Op-amp noise that is from the inputs, in which [70, 71] take into account the correlation of the equivalent noise current input spectra and the equivalent noise voltage.

Noise is generated not only on electronic signals but also on signal conversion from optical to electronic. For example, shot noise appears in the converted electronic signals of the photodiode due to the random arrival of the photons [66]. Modelling the discrete stochastic events of the photon electrical response as a Poisson distribution, the ordinary photodiode current is derived [72, 73]:

$$I(t) = \sum_i g(t - t_i) \qquad (2.2.13)$$

in which t_i represents the random occurring time of the photoelectric signal $g(t)$ from the absorption of a photon. Generally speaking, different formats for the noise $g(t)$ produce different shot noise; in Fig. 2.2.4 some examples are shown.
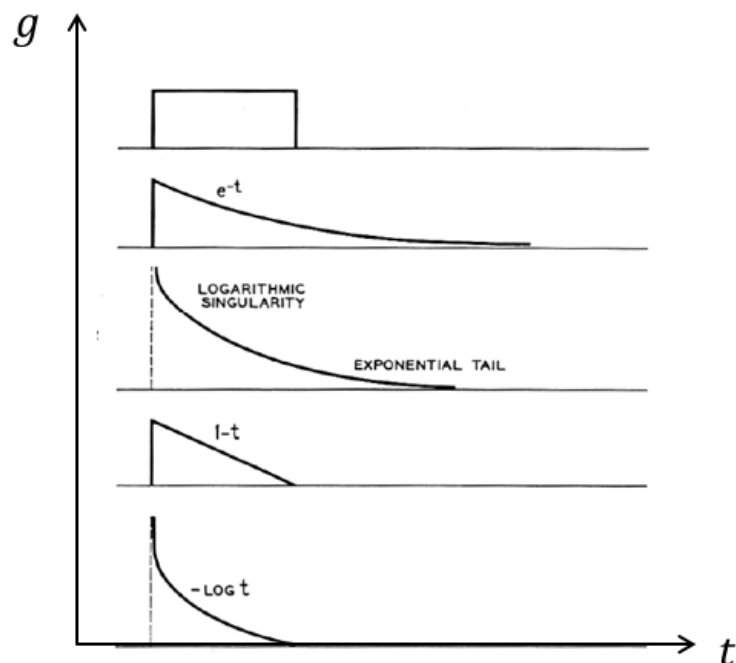
Adapted from [73]

Fig. 2.2.4 Shot noise shaping examples ($g(t)$).

Considering the photodiode response, therefore:

$$\int_{-\infty}^{\infty} g(t) = q \qquad (2.2.14)$$

in which q is the electrical charge. The average shot noise current is suggested in [74]:

$$I_n^2 = 2q(I + I_d)\Delta f \qquad (2.2.15)$$

where I is the photodiode signal current and I_d is the dark current.

   If an Avalanche Photodiode (APD) is the photoelectric converter of the receiver, excess noise is generated from the avalanche gain multiplication to the shot noise [75,

76]. From (2.2.13), the Poisson shot noise current with the random avalanche gain a_i becomes:

$$I(t) = \sum_i a_i g(t - t_i)$$
(2.2.16)

The noise factor of excess noise in the APD is [77, 78]:

$$F_e(M) = \kappa M + \left(2 - \frac{1}{M}\right)(1 - \kappa)$$
(2.2.17)

$$F_h(M) = \frac{M}{\kappa} + \left(2 - \frac{1}{M}\right)\left(1 - \frac{1}{\kappa}\right)$$
(2.2.18)

where $F_e(M)$ represents the electron injection, $F_h(M)$ represents the hole injection, M is the multiplication factor and κ is the electron initiated multiplication.

2.2.3 Signal Amplification for the Receiver Front End

Electronic signals converted from optical photons by the photodiode are usually too weak to be processed directly. As described in section 2.2.1, the photodiode frequency response is limited by the diode capacitance. Thus, the electronic signal amplifier for the photodiode front end has two functions: to amplify converted electronic signals at the photodiode front end and to compensate for the influence of the diode capacitor and extend the communication bandwidth. According to [79], two types of amplifier are able to perform these two functions, namely the TIA and the bootstrap amplifier. Considering a demonstrative amplifier solution, the TIA is more preferred to the bootstrap amplifier for the initial design. As the bandwidth of the TIA is limited by the open loop gain of the operational amplifier component [80], bootstrap amplifier may allow more bandwidth. However, both the bootstrap amplifier and the AGC amplifier uses positive feedback, implementing both may

increase the instability. What is more, bootstrap amplification can be combined in TIA to increase the bandwidth [81].

Moreover, due to the fact that the LED and the photodiode are in relative motion when the transceivers are connected to the optical channel in this application, fluctuations appear in the received signals, where an AGC amplifier is needed for the reduction of the fluctuation.

One example of a TIA which has been used in [82] and [83] is shown in Fig. 2.2.5.
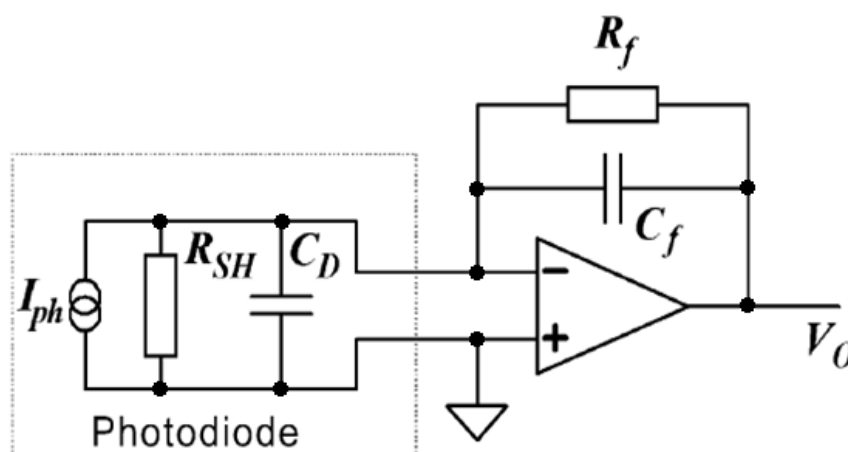
Adapted from [79]

Fig. 2.2.5 Example of TIA, in which I_{ph} is the photodiode current, C_D is the diode capacitance, R_{SH} is the shunt resistor, R_f is the feedback resistor and C_f is the feedback capacitor

The gain g_m of the amplifier is given by [82]:

$$g_m = -R_f \left(\frac{A_{OL}}{1 + A_{OL}} \right) \qquad (2.2.19)$$

in which R_f is the feedback resistor and A_{OL} is the Op-amp open loop gain. When $A_{OL} \gg 1$, the amplifier gain is approximately equal to $-R_f$. However, A_{OL} decreases at higher frequency and reaches 0 dB when the frequency is equal to the GBW of the Op-amp [84]. As a result, the Op-amp limits the performance of the TIA. What is more, the feedback capacitor aimed to reduce noise and overshooting generates a pole

with the feedback resistor and has a lower cut off frequency than that of the GBW as will be shown using a model of a simple TIA in Chapter 3.

The DC photon current may affect the TIA performance, in this application, the influence of DC photo current may not affect the performance to a level that needs to be compensated at the expense of power on additive components. If the influence is significant, the improved designs to reject DC photo current using active feedback loop can be found in [82, 85].

The AGC amplifier is an nonlinear system, for which two analytical models, one with and one without a logarithmic converter, are described in [86]. The generic AGC amplifier components for both models are shown in Fig. 2.2.6.
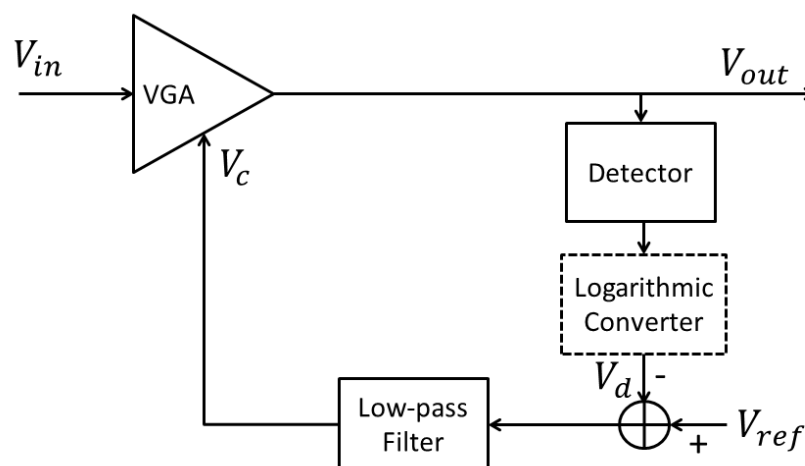
Fig. 2.2.6 Analytical model for the AGC amplifier

The gain control depends on the relationship between the gain of the Variable Gain Amplifier (VGA) and the control voltage V_c.

In the model with logarithmic converter, the gain of the VGA is:

$$g_{VGA} = K_1 e^{aV_c} \tag{2.2.20}$$

in which K_1 and a are constants of the VGA. Therefore, the transfer function of the model is:

$$V_{out} = V_{in}K_1 e^{aV_c} \tag{2.2.21}$$

Using a logarithmic converter between detector and V_d, the transfer function between V_{out} and V_d is:

$$V_d = ln(K_e V_{out}) \tag{2.2.22}$$

where K_e is the gain of the envelope detector. So V_c is related to V_{out} by:

$$
\begin{aligned}
V_c &= F(V_{ref} - V_d) \\
&= F[V_{ref} - ln(K_e V_{out})]
\end{aligned}
\tag{2.2.23}
$$

in which F is the response of the low-pass filter. These specific components compose an AGC amplifier that is linear in a decibel scale, which is:

$$ln[V_{out}(1 + aF(s))] = lnV_{in} + V_{ref}aF(s) \tag{2.2.24}$$

The decibel linearity also exists in a square-law detector that is modelled in [87], which defines the V_d of the logarithmic converter response from V_{out} as:

$$V_d = k_2 ln\left(\frac{V_0^2}{k_1}\right) \tag{2.2.25}$$

in which k_1 and k_2 are the constants of the logarithmic converter. A similar model containing more details of the AGC amplifier with logarithmic converter can be found in [88], which describes the settling time of this amplifier model.

If the logarithmic converter is not implemented in the AGC amplifier, the decibel linearity does not exist. The relation between V_{out} and V_{in} is in the form of $\frac{dV_{out}}{V_{out}}$

and $\frac{dV_{in}}{V_{in}}$ [86], based on which an iterative analysis is discussed in section 3.2.2. Modelling and design of the AGC amplifier with no decibel linearity is also described in [89]. What is more, [90, 91] uses the loop gain from V_{ref} to V_{out} to analyse the AGC amplifier. Since V_c generates positive feedback to the system, the studies of the resonance properties in [89] and [91] give the natural frequency ω_n and the damping factor ξ_d as:

$$\omega_n = \sqrt{K_1 K_2 K_d q_e} \qquad (2.2.26)$$

$$\xi_d = \frac{p}{2\sqrt{K_1 K_2 K_d q_e}} \qquad (2.2.27)$$

In which p_e and q_e are constants of the envelope detector transfer function:

$$H_e(s) = \frac{K_d q_e}{s + p_e} \qquad (2.2.28)$$

2.2.4   Signal Modulation

The signal modulation for indoor short distance optical communication channel with direct detection can be analogue or digital. Amplitude modulation is excluded from this discussion, since, in this application, large fluctuations exist in the amplitude of the original signal. According to [92], other available modulation techniques are Frequency Modulation (FM), Frequency Shift Keying (FSK) and Phase Shift Keying (PSK), as examples of analogue modulation techniques, and On Off keying (OOK) and Pulse Position Modulation (PPM) as examples of digital modulation techniques. The transferred data and corresponding optical signals of FSK and PSK are shown in Fig. 2.2.7.
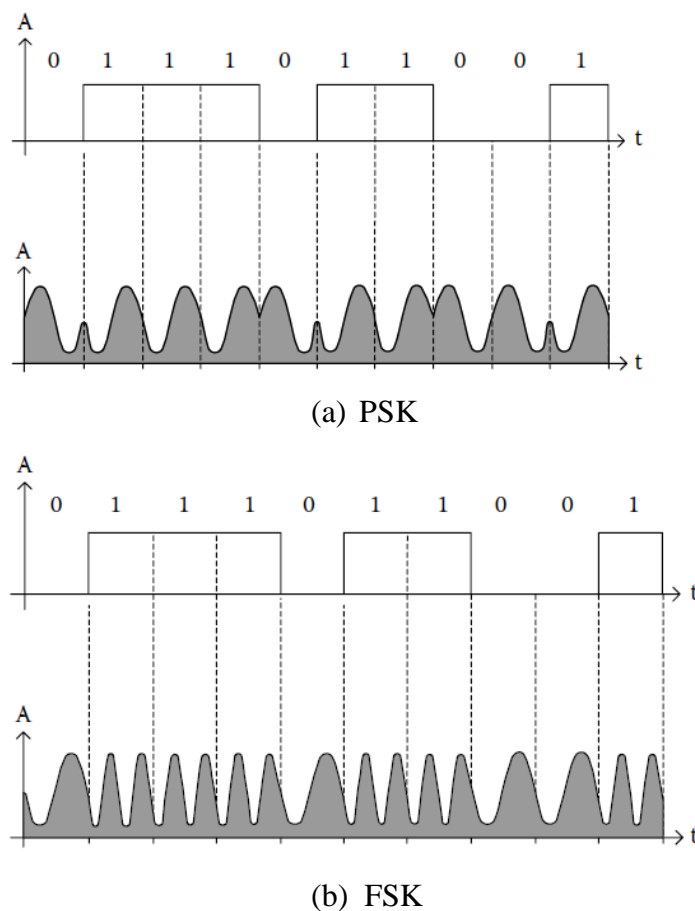
(a) PSK

(b) FSK

Adapted from [100]

Fig. 2.2.7 Examples of transferred data and corresponding optical signals of (a) PSK and (b) FSK

Early research of FSK in OW communications can be found in [93, 94] for multi-channel WLAN applications. PSK with a subcarrier has been investigated in [95, 96]. Thus, the channel reuse is an advantage of FSK and PSK. In an underwater application from [97], PSK can achieve higher data rate when compared to digital modulation, however, at the same time has the worst power efficiency. Moreover, PSK and FSK are also considered highly difficult to implement. In addition, Orthogonal Frequency-division Multiplexing (OFDM) became popular in optical communication recently because of the increase in bandwidth demand and the development of DSP that provides faster signal processing for OFDM [98].

In this application, the benefits of FSK, PSK and OFDM which come from channel reuse result in the capability to transmit more data during the limited communication period. This becomes important when the communication time of the

fast fading channel is not sufficient to transfer all the sensor data or the data comes from multiple sensors and needs to be transferred in one channel. However, the poor power consumption cannot be ignored, and, coupled with the implementation complexity, power efficiency may be further depressed on extra energy spent on the physical layer of the modulation (hardware). Considering power is more essential than a higher data rate for the application, digital modulation is preferred.

Digital modulation techniques are well developed for OW communications. One of the successful examples is the IrDA standard using OOK and PPM at different bit rates [99, 100]. Besides those two modulations, Digital Pulse Interval Modulation (DPIM) is a potential substitution of PPM, which eliminates unused time slots in PPM to gain higher transmission efficiency [101].

Based on the arrangement and number of pulses in a symbol as well as the symbol length, there are at least three major PPM schemes, namely traditional PPM (1-PPM), Multi PPM (MPPM) and Overlapped PPM (OPPM) [102, 103]. In a symbol period T_s that is sliced into n sub-slots, in 1-PPM only one slot is occupied by the signal pulse in those slots, in which the pulse interval is $\frac{T_s}{n}$. The pulse occupation of symbol slots on MPPM and OPPM are both more than one. The slots in use are not constrained and can be arbitrary in MPPM, while in OPPM those occupied slots are joint. What is more, more symbols can be generated if the total amount of slots can be different of 1-PPM and OPPM, namely Differential-PPM (DPPM) and Differential Overlap-PPM (DOPPM) [102, 104], and a combination scheme of MPPM and pulse width modulation is discussed in [105]. What is more, the modulation can be on the interval of the pulse, a symbol example of a digital pulse interval modulation with 4 symbols (4-DPIM) scheme is shown in Fig. 2.2.8, the difference between the symbols is from the amount of unoccupied slots. The pulse of DPIM can also be used for synchronization and does not require extra synchronizing pulse [106].

Adapted from [106]

Fig. 2.2.8 Example of 4-DPIM scheme without guarding slot

The power performance of the above modulations are compared with OOK as a benchmark in several references [102, 106, 107], in which the power ratio of one modulation over OOK in the same bit rate and Bit Error Rate (BER) is approximately the ratio of the minimum Euclidean distance between the two nearest symbols of the modulation over that of the OOK. As a result, the power ratios are:

$$\frac{P_{PPM}}{P_{OOK}} = \sqrt{\frac{2}{L \log_2 L}} \tag{2.2.29}$$

$$\frac{P_{MPPM}}{P_{OOK}} = \frac{2m}{\sqrt{nd \log_2 L}} \tag{2.2.30}$$

$$\frac{P_{OPPM}}{P_{OOK}} = \frac{2m}{\sqrt{2n \log_2 (n - m + 1)}} \tag{2.2.31}$$

$$\frac{P_{DPIM}}{P_{OOK}} = \frac{4\sqrt{\frac{L+1}{\log_2 L}}}{(L+3)\sqrt{2}} \tag{2.2.32}$$

in which $P_{(modulation)}$ represents the average power of the modulation, L is the total slots per symbol in MPPM and OPPM and the maximum slots in DPIM, n

is the total amount of symbols selected for the modulation scheme, m is the number of occupied slots in MPPM and OPPM, and d is the minimum Hamming distance between MPPM selected symbols. From the results in the literature [102, 106, 108], in a general manner the power requirement rating of the modulations can be summarized as OPPM > OOK > 1-PPM > DPIM > MPPM. The exact power depends on the preference of L, n and m. The selection and power analysis of the modulation for the fast fading channel will be presented in section 4.3.

2.2.5 The IrDA Standard

IrDA is a short distance wireless infrared communication standard for point to point half duplex communication released by the Infrared Data Association, dating back to 1993 [92]. From then on, the officially stated milestones of the IrDA development on data rates were: 4 Mbits/s in 1994, 16 Mbits/s in 1999 and 1 Gbits/s in 2009 [109]. As mentioned in section 2.1.2, the device in [30] has been developed for data transfer of rotor monitoring using the IrDA protocol. A considerable advantage of adopting this off-the-shelf technique is reducing the effort and uncertainty of the hardware development. This section investigates whether IrDA can be implemented on the fast fading channel.

The IrDA protocol has now developed beyond the early function of cable replacement into an application dependent wireless platform [110]. The protocol plays the role of interfacing between the user application and the wireless infrared communication, as can be shown from the summarized IrDA architecture in Fig. 2.2.9 [110-112]. According to the Infrared Data Association, the functions of the core layers are briefly described as [111]:

- Information Access Service (IAS): advertisement and discovery for remote devices
- Infrared Link Multiplexing Protocol (IrLMP): multiplexing services
- Infrared Link Access Protocol (IrLAP): link management
- Framer/Driver: interfacing physical devices

● Physical Layer: specification of physical devices

The physical layer can be further divided, based on the data rate, into: SIR up to 115.2 kbit/s, Medium Infrared (MIR) up to 1.2 Mbit/s and Fast Infrared (FIR) at 4 Mbit/s [116, 117]. Other layers, such as Object Exchange (OBEX), Infrared Communication (IrCOMM) and Tiny Transport Protocol (Tiny TP), are application specific and redirect the data to the targeted destination [112].
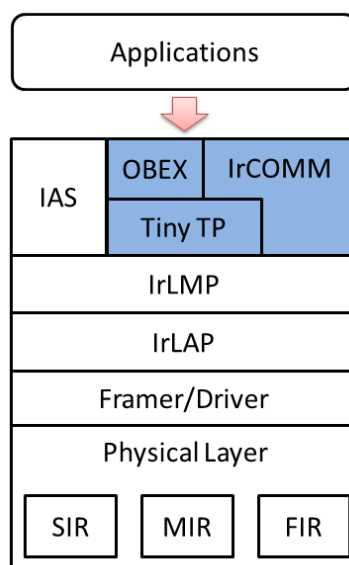
Fig. 2.2.9 A summarized IrDA architecture, with optional layers marked blue.

From the protocol introduction above, upper layers of the IrDA protocol define the interface of wireless infrared communication to different software applications. To investigate the possibility of using IrDA in this application, the IrLAP layer is considered at first to find if there is any conflict between the specific channel condition and the IrDA optical standard concerning throughput efficiency and burst transmission.

In general, the data rate of IrDA is sufficient for the intermittent communication in this application as it exceeds 1 Gbit/s. Even if the available communication period is only 1/1000th of a rotation cycle, the overall data rate is reduced from 1 Gbit/s to 1 Mbit/s. However, a high data rate may not result in high information rate when taking the turnaround time into account. The model in [113] indicates that higher data rates

transmit more data in one packet and results in a longer turnaround time, but higher throughput efficiency needs smaller turnaround time. What is more, even if the turnaround time can be fulfilled, the BER of higher data rates (16 Mbit/s in [114]) must be optimized or the performance becomes poor due to the retransmission of data frames [113-115]. This may lead to a situation where the poor throughput efficiency of a high data rate may produce a lower information rate than that of a low data rate in this application, due to the limited time and intermittency of communication.

According to the description of the communication discovery and negotiation of the IrDA standard in [111], several pairing steps should take place before the communication is established and useful data can be sent. These steps secure a private link for two transceivers when multiple transceivers might be present in the wireless channel. But in this application the wireless channel for two devices is guaranteed, therefore the pairing is not necessary and may cause failure of communication if pairing needs to be performed for each cycle. Moreover, the period for communication in one rotor spinning cycle may be too short to introduce the whole pairing procedure. For example, for an off-the-shelf chip, the primary device has to wait for up to 500 ms to ensure no other device is using the wireless channel; but considering a rotor speed of 1000 rpm, the rotation cycle is merely 60 ms, which means the devices waits more than 8 cycles before starting the communication.

From the IrDA definition for the physical layer, a data frame contains 8 bits of data with one start bit and one stop bit, in which SIR and MIR uses Return-to-zero Inverted On-Off Keying (RZI-OOK) and FIR uses 4-PPM [111, 116]. The definition of a SIR data frame and the corresponding UART frame is shown in Fig. 2.2.10. Taking into consideration that the speed dependent communication period of each rotation cycle is not identical in this application, the communication will be blocked randomly in a data frame. The direct impact of the random stop in the data frame is the following: if the communication is blocked inside an SIR frame, in the receiver all blocked bits will be detected as '1'.
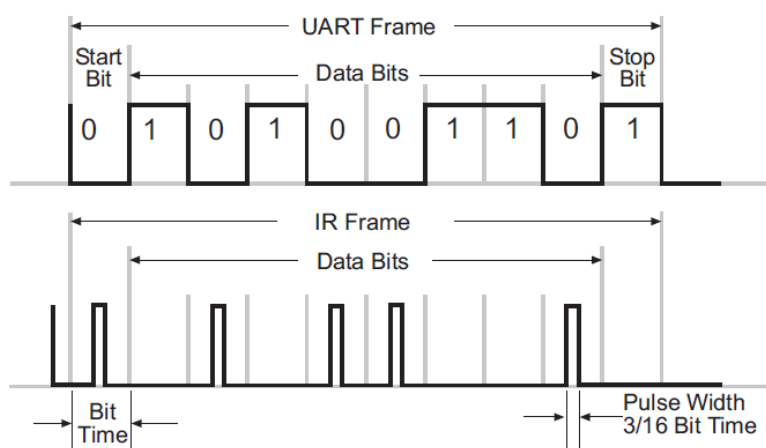
From [111]

Fig. 2.2.10 IrDA SIR data frame compared to UART data frame

In summary, the original IrDA protocol cannot be considered as a solution for our application as the protocol is based on a continuous optical channel. In the fast fading channel, the pairing procedure causes inefficiency and the data frame definition may results in extra errors. Therefore, the communication protocol in this application must be modified or redesigned to adapt to the circumstances created by the intermittency of the channel.

2.3 Power Supply of the DT Device

The most important advantage of a wireless communication system for the moving rotor is that the sensing is not impeded by wire connections, however, at the same time this raises the difficulty of power supply. Moreover, the solutions based on wireless RF communication have been shown, to different extent, to be affected by the strong EM field [117-119]. In this application the fact that the DT device on the rotor is subjected to a strong EM field and heat radiation from the surrounding environment can be exploited as sources of thermoelectric, electromagnetic and photovoltaic energy. Therefore these sources could potentially provide a solution based on power scavenging to sustain the DT device, providing that they can satisfy its power consumption.

2.3.1 Environmental Power Harvesting and Passive Sensing

In this section, it is attempted to find a possible power supply for the DT device from scavenging environmental sources, such as the EM field and heat, or by transferring power wirelessly via the photoelectric effect. What is more, the practicability of passive sensing is also investigated.

Thermoelectric

Compared to the chemical thermal batteries for the instant and high power requirements such as the backup power for rockets and aircrafts [120, 121], semiconductor generators are more adaptive to applications with low power requirements for a long life cycle. For example, 'Micropelt' has developed a series of long-lifetime, maintenance-free thermal generators [122].

The power conversion of the thermal generators is based on three related effects relating heat power with corresponding electron movements, discovered over 150 years ago by three scientists, namely the Seebeck effect, the Peltier effect and the Thomson effect. These effects, in general, are illustrated by the equations below [123, 124]. Assume two conductors of different temperatures, T_1 and T_2, connected in series, where $T_1 > T_2$. In (2.3.1), the electromotive force V, generated from the temperature difference of the conductors is related by the Seebeck coefficient α.

$$V = \alpha(T_1 - T_2) \qquad (2.3.1)$$

Moreover, as established from the Peltier effect [123, 124], this conversion is reversible. In (2.3.2), the ration of the current flow I_β and the reversible heat q_H is given by the Peltier coefficient β. This provides the device with an extra high efficiency heat sink effect, respectively. A specific product for cooling via electricity, named 'Peltier Cooler', is also presented by Micropelt [125]. In a sense, the thermal generator is potentially a solution for keeping the communication system within working temperature limits in the hot environment inside the motor or generator.

$$\beta = \frac{I_\beta}{q_H} \tag{2.3.2}$$

In (2.3.3) for a single conductor, if the temperature difference $\varDelta T$ exists on two ends, a current I_γ is generated and also results in reversible heat, where γ is the Thomson coefficient.

$$q_H = \gamma I_\gamma \Delta T \tag{2.3.3}$$

(a) Pseudo-module

Hot side

p-type segmented element   Cold side   n-type segmented element

Brass electrode

(b) Prototype module

Brass electrode

p-type segmented element   Hot side   n-type segmented element

Ag paste
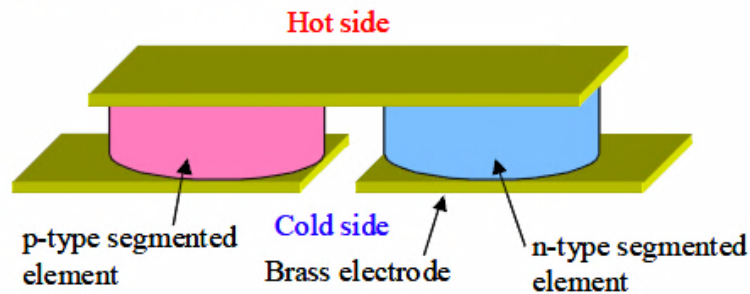
Cold side
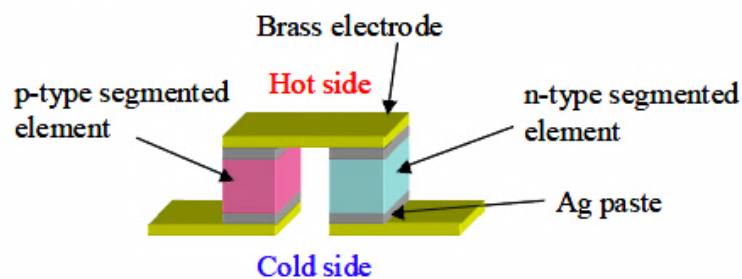
Adapted from [126]

Fig. 2.3.1 Two Peltier Cooler thermal generator modules.

The core module of thermal generators is shown in Fig. 2.3.1. The difference between the two modules is that the p− and n−type elements in (b) are segmented to decrease the electrical resistance when compared to (a), aiming at preservation of the temperature difference between the hot side and cold side [126, 127]. Such a simple structure can be fabricated at a small scale by MEMS to maximize the flexibility of the device size.

The power converting efficiency of the thermoelectric generators can be affected by many factors, such as the amount of modules as shown in Fig. 2.3.1 and the electric current [128], as well as the temperature difference. The latter is influenced, in turn, by the heat source which determines the temperature of the hot side and by the heat-harvesting device itself, which reduces the temperature difference. It has been demonstrated that the efficiency of most segmented thermal generators increases when the hot side temperature rises [129]. According to a test by Khluabwannarat et al. [130], the internal temperature of a motor in normal working condition is about 80 ℃, resulting in the thermoelectric energy converting efficiency of the temperature is most likely to be less than 10% [131, 132].

Photoelectric

Considering the optical signals in this application, the energy from the photodiode received optical power is far from sufficient for supplying the signal processing circuit or driving an IR LED, even using solar batteries for power harvesting [133].

To solve the problem, a source with high power density is necessary, such as a laser, which is a possible carrier of both information signals and energy. Without data transmission, laser beams are proved as power sources in applications like the NASA Space Elevator [134] and the high efficiency laser power cell [135]. Moreover, the power converting efficiencies are higher compared to the thermal generator, for example 40% for most of the examples from the Space Elevator project and 52% for the power cell's receiver structure after optimization. However, as the laser heats up the power receiver, the thermal resistance increases and subsequently the power converting efficiency reduces, even if the heat is sunk properly the energy lost from this effect is significant [136].

Electromagnetic

Generally speaking, the magnetic field is the most important power source that can be scavenged from motors and generators since it is strong and constant. As a pure power carrier, the magnetic field appears in the phenomenon of wireless self induction, like a separated pair of windings in a transformer. Some examples of applications are:

using the coupling windings to transfer power to support a micro-robot for an endoscope [137], stimulating a retinal prosthesis [138] and powering up a biomedical sensor [139]. The common features of all those medical applications are the short range and low power consumption, since the power efficiency decreases substantially when distance between the coupling coils increases [140, 141]. In addition, the method has also been demonstrated through the use of AC coupling, as described in section 2.1.2 [26, 28, 35].

In this application, the proposed solution is to scavenge power directly from the surrounding EM field rather than transferring it through couplings, due to the limitation imposed when implementing the coupling antennas, which have been discussed in section 2.1.2. Considering the strong dependence on distance, the harvesting antenna needs to be located in a strong EM field to gain enough power. At the same time, the EM field creates a potential interference on the communication device. Therefore, further research is needed to investigate the EM field distribution of the inner space near the rotor and stator structure.

Passive Sensing

Another possible solution is installing a system with only passive sensors and excluding any component that needs power support. As the feature of passive sensors is to modulate the signals going through them and to remove some of the signal energy that is converted from the measured physical property, the modulated signal is then returned and demodulated by the receiver [142]. However, research by Pothl et al. [143] shows that SAW sensors used in a passive sensing application are affected by interference from the EM field even when the signal transfer distance is short. An exceptional case has been found in the multiple sensor readout system developed by Taslakov & Simeonov [144], which uses an innovative approach to modulate the RF signals onto a laser beam using a modified Michelson interferometer. Alternatively, optical modulators like Electroabsorption Modulator (EAM) and Mach–Zehnder Modulator (MZM) are potential transformers for converting the RF passive sensor signal to optical signals. However, EAMs cannot modulate the analogue signals that

the majority of the passive sensors provide [145]. On the contrary, a MZM like modulator was adapted in a sensor structure by Norman et al. [146], in which the possibility to implement MZM in a passive detecting system was shown. What is more, a passive optical sensor system based on the optical absorption band shift at different temperatures has been previously discussed in [34] in section 2.1.2, which is an ideal solution for applications that do not require fast sampling rate.

Summary

The possible power sources and solutions for DT that have been reviewed above are summarized in Table 1, in which their advantages and disadvantages are compared.

Power sources	Advantages	Disadvantages
Thermoelectric	● Small and simple structure, flexible ● Constant heat resource ● Extra heat sink effect	● Comparatively low power efficiency
Photovoltaic	● High Power efficiency	● Only available during the communication window, overall power efficiency is reduced. ● Heat sink affects the performance.
Electromagnetic	● Simple ● The technique has been widely applied	● Efficiency highly depends on location ● May introduce interference
Passive Sensing	● No power consumption	● Cannot use existing sensors ● Optical modulation is to be demonstrated

Table 1 Comparison of the reviewed possible power supplies and solution

2.3.2   Power Consideration of the DT

Without considering the power requirement of the sensors, as shown in Fig. 2.1.2, the DT contains two parts: one is the signal processor; the other is the antenna

and driver, which is the optical transceiver circuit in optical communication. As discussed briefly in section 2.2.5, the IrDA protocol is not appropriate for our application and a new protocol has to be implemented. Therefore, implementation solutions containing dedicated protocol chips cannot be used in our case and the signal processor is assumed a microcontroller.

To transfer sensor data from the rotor with limited power, the communication controller should afford a sufficient data rate and minimize the power consumption of the whole system. The power consumption of the microcontroller simply depends on the type of processor used. If the preference is for more power saving than processing capacity, the MSP430 microcontroller shows great potential for our application. Successful use of this microcontroller for wireless infrared communication can be found in a few applications. The examples are: in [147, 148] the MSP430 as encoder/decoder for the IrDA protocols; in [116] the MSP430 controls the IrDA transceiver chip in the other. More examples of low power RF applications can be found in [149-151], especially in [151], where the microcontroller is used in a wireless rotor temperature sensing application. What is more, [152] shows a complete thermoelectric scavenging solution to power the MSP430. Therefore, from a power consumption aspect, using a microcontroller in this application is feasible.

In addition, the power for the optical transceiver circuit is critical in this application. According to [92, 153], the antenna and driver in OW communication include the functions of modulation and demodulation of electronic signal and optical signal and driving the LED transmitter and photodiode receiver. Considering OOK as the modulation and LED as the transmitter, the statistical average power consumed by the LED is half of the optical signal power 'on' [102, 106]. In practice the emitted optical power is approximately linearly related to the LED supply current [154]. Using the specification of an actual IR LED [155], the typical total optical power from radiation is 50 mW for a 100 mA supply current, which is an adequate emitted power for our application, as shown in the channel model later in section 3.1. As another example, the current suggested in the experimental result of [156] is 140 mA when the 5 V bias is applied. From the two examples, a typical average power

consumption of the LED P_{LED} on OOK modulation can be estimated as 250-350 mW. Assuming the communication is half duplex, the power dissipation is P_T when the device is in transmitter mode and P_R in receiver mode. P_T is the sum of P_{LED} and P_R:

$$P_T = P_{LED} + P_R \qquad (2.3.4)$$

In the applications that the rotor is at a stable speed, the start and time length of the communication window are predictable, therefore the transceiver can be turned off outside the window and power loss is largely prevented. In this case, the operating period of the transmitter and the receiver is approximately equal, the average power dissipation of DT being:

$$\bar{P} = r_T(P_{LED} + P_R) \qquad (2.3.5)$$

in which r_T is the ratio of the transmitting period over the whole time in one rotor spinning cycle.

In applications where the speed of the rotor is variable, the power condition is more critical, since the DT needs to hear from the DR when waiting for the communication period of another cycle, the receiver of DT is full-time active. Thus, the device consumes power all of the time, with extra power P_{LED} consumed when transmitting. The average power dissipation of the optical antenna and driver on the DT then becomes:

$$\begin{aligned} \bar{P} &= R_T P_T + (1 - R_T)P_R \\ &= r_T P_{LED} + P_R \end{aligned} \qquad (2.3.6)$$

Assuming the same circuit configuration in [156] is used, P_R is 25 mW. From the experimental result of [128], the power output of a thermal generator ranges from 5 mW to about 36 mW in the heat reservoir temperature range of 37 K to 90 K.

Assuming the thermal generator is adapted to supply the optical transceiver circuit, when generating the maximum power output and the unused energy is well preserved with no loss, r_T from (2.3.5) can be 0.37 to 0.48 using OOK, which is enough for the application that the rotor speed is stable. However, r_T from (2.3.6) is decreased to 0.031-0.044 if the rotor speed is not predictable, which means the data can only be transmitted between 3% and 4.4% of the rotation cycle. r_T decreases even further when the LED is on with no modulation, which has a power consumption double that of the OOK, resulting in the r_T: 1.5% ~2.2%. Considering the time proportion of the communication period in a spinning cycle and the half duplexing, r_T is still a satisfactory value. But this result is derived in the circumstance that the temperature difference between the generator's hot side and cold side needs to be 90 K.

Therefore, to fulfil the entire power requirement of the DT, including the microcontroller and optical transceiver circuit whilst maintaining full data rate, the microcontroller and the circuit need separate power supplies to maintain the full time operations of the microcontroller and the receiver.

3 Models

3.1   Optical Channel Performance

As described in section 2.1.2, the device installation location can be more flexible if sensor data is not necessarily transferred in a continuous optical link. A non-continuous link only requires that the receiver is in the radiation range of the transmitter LED when they are approaching and leaving each other, thereby it does not need a special antenna design or a specific mounting location. However, the time for the data transfer is severely limited without a continuous link, therefore the sensor sampling rate may need to be reduced if the sensor data cannot be fully transferred in the time limited channel. Moreover, from the fact that the IR LED radiation is diffusive and the power is stronger at the centre, the receiving power fades in and out when the receiver goes across the front of the transmitter LED, and this additional signal fluctuation also affects the data transfer. To investigate the practicality and explore the performance of the periodic fast fading optical channel, a numerical model is introduced.

3.1.1   Problem Definition

Here it is considered that the optical channel in an idealised case to some extent, by excluding the effects of the atmosphere (such as soot in the environment) and signal fluctuation caused by mechanical vibrations. The two examples of hardware setup are shown in Fig. 3.1.1. The rotor is spinning with a constant angular velocity ω. The transmitter IR LED is placed on the rotor and emits optical power at a certain level continuously on the rotor, and when it approaches the receiver, those signals are received by the photodiode. Because the diffusion of the IR LED starts from the radiative centreline to the outer space, when the LED moves past, the photodiode

position changes from the radiation edge to the centre and to the edge again, resulting in the received signal power fading in and out accordingly.

(a)

(b)
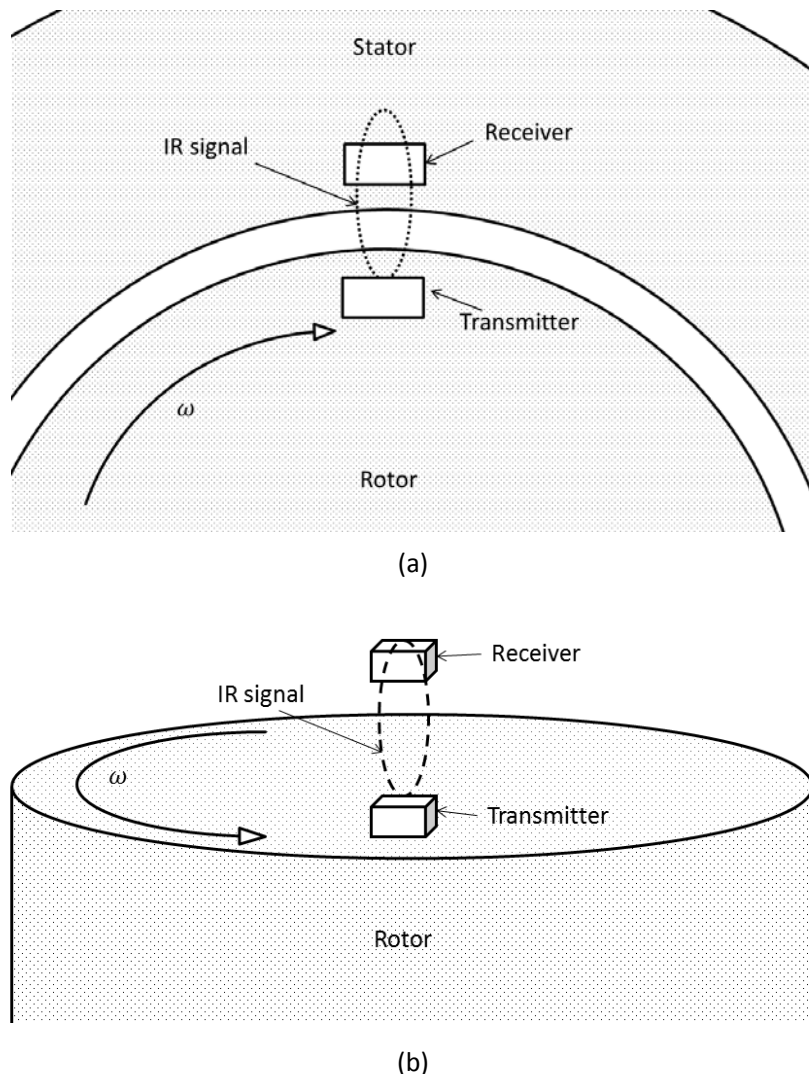
Fig. 3.1.1 Examples of hardware setup of an OW LOS channel where the transmitter is horizontal in (a) and vertical in (b)

Assuming OOK is used as modulation, the presence of optical radiation represents symbol '1' and absence of radiation represents symbol '0'. An illustration of the bit power of a '1' is shown in Fig. 3.1.2. The received signals appear in a communication window once in each cycle of the rotation, so the interval between two communication windows is $\frac{2\pi}{\omega}$. In each communication window, the actual communication session is restricted by the threshold strategy and a certain BER. For a set noise level and threshold, there is a power requirement for each bit to preserve a specific BER, since

error rates of bits with power near the threshold level are too high. Therefore, only those bits with sufficient power can be used. As a result, the communication session is shorter than the communication window, which is also illustrated in Fig. 3.1.2.
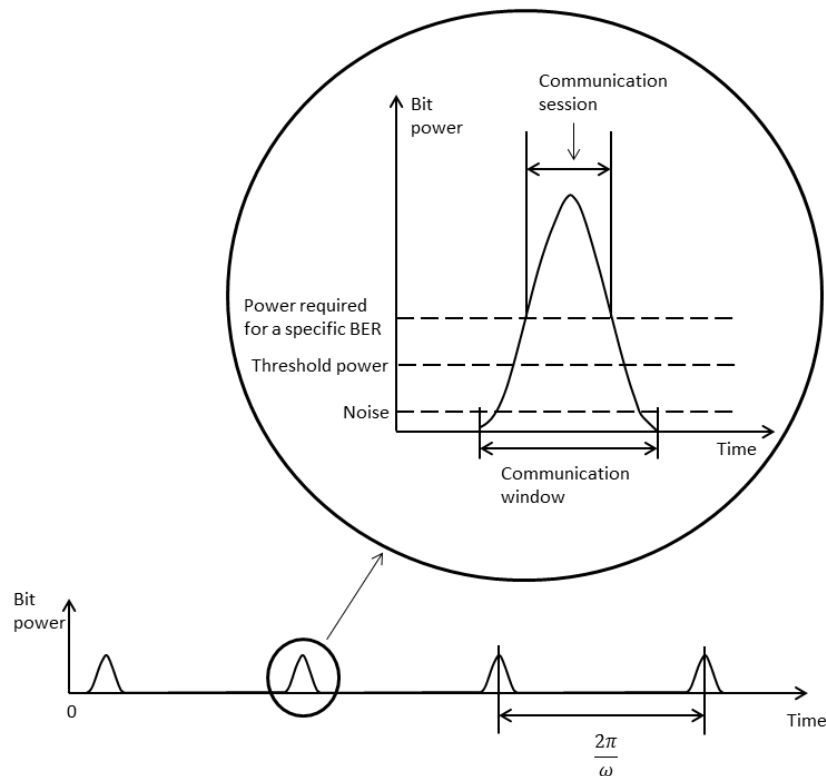
Fig. 3.1.2 The communication window and communication session of the periodic fast fading channel

The proportion of the communication window time in the associated cycle relative to the whole time cycle, termed Communication Window Ratio (CWR), remains the same at a stable speed because it is determined by the LED radiation pattern and the placement of the devices, which remains unchanged after the installation. In other words, the CWR is the same when no angular acceleration is present. If those cycles with acceleration are ignored, the sum of communication windows' width in a certain period is independent of the rotor's angular velocity, and the relative CWR is determined by the hardware configuration.

Consequently, the model investigates mainly two factors: the fading bit power and the corresponding effects on the channel performance. To describe the fading from motion, or more exactly from the position shift caused by the movement, the

Lambertian radiation pattern is used. The diffused power density of radiation from the LED can be quantified in the radiation pattern, knowing that the received power depends on the radiative angle and the distance from the light source in free space [54, 157]. The error rates are estimated using the Saddlepoint approximation, which has been applied in the analysis of photodiode receiver performance, based on received signal power, noise and threshold [65, 158-160].

3.1.2 The Numerical Model

1. Received power

Fast fading of the channel comes from power variation due to the relative position of the LED and photodiode during the rotor's rotation cycle. Thus, a simplified geometry, shown in Fig. 3.1.3, is designed to explain the time dependent relative positions. The idea of the simplificiation is to approximate the rotation to a linear motion, where the angular and circular parameters are reduced.
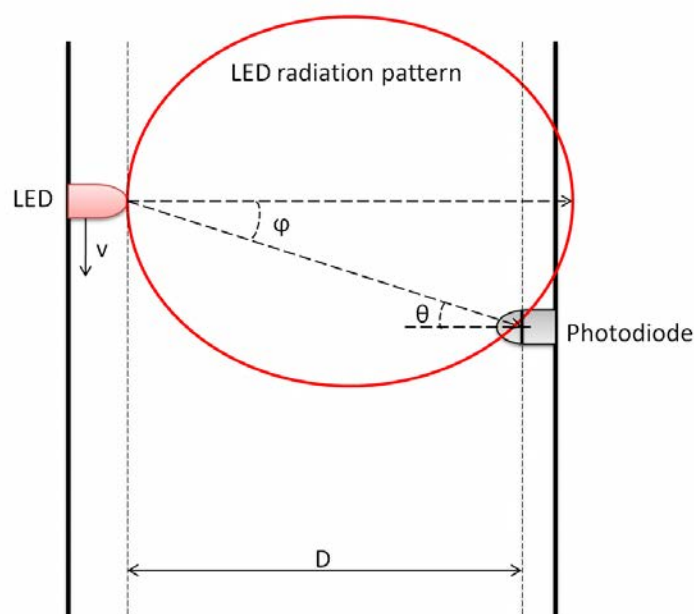
Fig. 3.1.3 A simplified geometry to explain the received power

The LED and photodiode are located on two parallel tracks at a distance D, facing each other in a perpendicular direction. When their rotation radiuses are comparatively

large, the tracks are nearly linear. Assuming the radiation of the LED is an ideal
Lambertian pattern, the received power from the photodiode effective collection area
P_R is described as [157]:

$$P_R = \frac{P_P A_{eff}}{d^2} \tag{3.1.1}$$

in which d is the distance between the LED and photodiode, P_P represents the
received power intensity and A_{eff} is the photodiode effective photon collection area,
defined as follows [9, 10]:

$$P_P = \frac{n+1}{2\pi} P_E \cos^n(\varphi) \tag{3.1.2}$$

$$A_{eff} = A_r \cos(\theta) \tag{3.1.3}$$

$$d = \frac{D}{\cos(\varphi)} \tag{3.1.4}$$

where P_E is the emitted power intensity, φ is the angle between the LED's radiation
centreline and the direction to the photodiode, in the range of $(-\frac{\pi}{2}, \frac{\pi}{2})$, A_r is the photo
collection area of the photodiode, $\cos(\theta)$ is the angular factor of the photodiode
efficiency. The mode number n of the Lambertian radiation pattern determines the
beam width. If the rotation radiuses of the LED and the photodiode are much larger
than D, φ and θ are approximately the same, as in Fig. 3.1.1 (a). In applications with
small rotation radius, due to the limitation of space, the devices are more likely to be
placed as in Fig. 3.1.1 (b), in which $\varphi = \theta$. When the LED is moving with a constant
speed v and t_0 is defined as the moment the LED is at the shortest distance from the
photodiode, those angles are:

$$cos(\varphi) = cos(\theta) = \frac{D}{\sqrt{D^2 + v^2(t - t_0)^2}} \tag{3.1.5}$$

Replacing relevant parameters in (3.1.1) using (3.1.2)-(3.1.5), the power received by the photodiode in time becomes:

$$P_R = \frac{n+1}{2\pi} P_E A_r \frac{D^{n+1}}{[D^2 + v^2(t - t_0)^2]^{\frac{n+3}{2}}} \qquad (3.1.6)$$

2. Thermal noise and -3 dB frequency of the photodiode front end

The photodiode front end of the model is shown in Fig. 3.1.4, in which I_P is the photo current, C_d is the diode capacitance and R_L is the load resistor. Since the photodiode shunt resistance R_{sh} (considering the leakage dark current in the previous model of section 2.2.1) is significantly higher than R_L, the shunt resistance is ignored in this model.
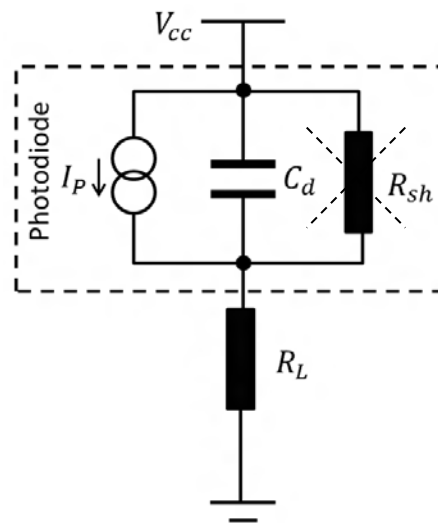
Fig. 3.1.4 The photodiode front end

The thermal noise from the electronic circuit of the photodiode front end is caused by "the random thermally excited vibration of the charge carriers in a conductor" [62, 63]. Using the Johnson noise model, thermal noise can be modeled by a Gaussian distribution, for which the variance σ^2 is defined as [65, 66]:

$$\sigma^2 = S_n T_b \qquad (3.1.7)$$

In (3.1.7) T_b is bit time and S_n is the two-sided equivalent noise power spectral density that is calculated by:

$$S_n = \frac{2kT_n}{q^2 R_L} \tag{3.1.8}$$

in which $k = 1.38 \times 10^{-23}$ J/K is Boltzmann's constant, T_n is the equivalent noise temperature, $q = 1.6 \times 10^{-19}$C is the electrical charge and R_L is the noise source resistance. As $R_{sh} \gg R_L$, the noise current from the photodiode shunt resistance is much smaller than that from the load resistance, therefore the thermal noise current from the shunt resistor is ignored. The load resistance also affects the performance of the channel by influencing the -3 dB frequency, which is given by:

$$f_{-3dB} = \frac{1}{2\pi R_L C_d} \tag{3.1.9}$$

From the definitions of thermal noise and -3 dB frequency, the common trade off is reflected in the selection of the load resistor: a higher load resistance results in lower noise current and better BER performance, and at the same time, it is restricted by a lower bandwidth limit from the -3 dB frequency.

3. Optical noise and the Saddlepoint approximation

According to [66], shot noise is presented in the photonic signal received by a photodiode. The shot noise can be explained by a Poisson distribution that the expected number of photons m in a pulse of time length T_b started at t_0 is:

$$m = \int_0^{T_b} \frac{\eta P_R(t + t_0)}{hf} dt \tag{3.1.10}$$

in which η is the quantum effeciency of the photodiode, $h = 6.6261 \times 10^{-34} \, W s^2$ is Planck's constant and f is light wave frequency. Therefore in the Saddlepoint approximation, the moment generating function (MGF) of the Poisson events is:

$$\Psi_m(s) = \exp[m(e^s - 1)]$$

$$= \exp\left[(e^s - 1)\int_0^{T_b} \frac{\eta P_R(t + t_0)}{hf}dt\right] \quad \text{(3.1.11)}$$

and the MGF of the Gaussian thermal noise is [17]:

$$\Psi_n(s) = \exp\left(\frac{s^2\sigma^2}{2}\right) \tag{3.1.12}$$

where the σ^2 is defined by (3.1.7) and (3.1.8). The MGF of symbol '1' is the product of (3.1.11) and (3.1.12), and that of '0' is (3.1.12).

3.1.3 Methodology

In general, the overall BER result from the Saddlepoint approximation is an average of the error rates of symbols '1' and '0', so that the noise condition of the whole channel is reflected. However, BER varies according to the position of bit '1' in time due to the power fluctuation, but BER of bit '0' stays the same. Therefore the evaluation method needs an alternative to specify the performance.

Instead of evaluating the channel performance from the BER directly, the bit capacity is used and the BER is set to a fixed satisfactory value, which is 10^{-6}. The BERs of '0' and '1' are both required, independently, to reach 10^{-6}.

For symbol '0', for which the IR signal is absent, only Gaussian noise is present and the MGF is approximated by (3.1.12), and previous work suggests 6σ as the threshold value to maintain a 10^{-9} error rate [161]. For a 10^{-6} error rate, the threshold calculated from the approximation is 4.76σ, which can also be found by another demonstration, as follows.

According to [106] and [162], the BER of a modulation scheme is dominated by the two nearest symbols:

$$BER = Q\left(\frac{d_{min}}{2\sqrt{S_n}}\right) \tag{3.1.13}$$

in which N is the power spectrum of Gaussian white noise and d_{min} is the minimum Euclidean distance between two symbols, defined as:

$$d_{min}^2 = \min_{i \neq j} \int \left[x_i(t) - x_j(t)\right]^2 dt \tag{3.1.14}$$

The definition of the Euclidean distance between the two symbols of OOK by definition is:

$$d_{min}^{OOK} = P_R\sqrt{T_b} \tag{3.1.15}$$

Inserting (3.1.15) and (3.1.7) into (3.1.13),

$$BER_{OOK} = Q\left(\frac{P_R T_b}{2\sigma}\right) \tag{3.1.16}$$

$P_R T_b$ also represents the bit energy of '1', and in the Gaussian noise channel, the best threshold energy of OOK can be calculated as the average energy of the two symbols:

$$E_{td} = \frac{P_R T_b + 0}{2} \tag{3.1.17}$$

As a result,

$$BER_{OOK} = Q\left(\frac{E_{td}}{\sigma}\right) \tag{3.1.18}$$

From $Q(6) \approx 10^{-9}$, it can be verified that the threshold of OOK reaching an error rate of 10^{-9} is 6σ in the Saddlepoint approximation using (3.1.18). Likewise, $Q(4.76) \approx$

10^{-6} has the agreement of 4.76σ threshold for the error rate of 10^{-6}.

When symbol '1' has sufficient power and the corresponding error rate is dropped under 10^{-6}, the communication session begins. Likewise, the communication session ends when the signal power decreases to a value for which the error rate is above 10^{-6}.

Thus, the minimum threshold used was 4.76σ, and based on this threshold the communication session was determined. BT is introduced as the bit capacity, where T is the time length of the communication session and B represents the bandwidth, given by the inverse of the bit time T_b:

$$B = \frac{1}{T_b} \qquad\qquad (3.1.19)$$

Because the symbol rate of OOK is one, BT represents the maximum amount of bits that is allowed in one communication session. To describe the power efficiency of a channel, the energy per bit is introduced, which is defined as:

$$E_b = P_e T_b = \frac{P_e}{B} \qquad\qquad (3.1.20)$$

As discussed in section 3.1.1, the CWR is determined by the hardware setup regardless of the angular velocity, therefore the overall bit rate b_W can be defined as:

$$b_W = \frac{BT}{T_R} \qquad\qquad (3.1.21)$$

where T_R is the period of a rotation cycle. For a given sampling rate for the sensor r, the bit rate required is:

$$b_r = \frac{\gamma r}{\beta} \qquad\qquad (3.1.22)$$

in which β is the code rate, which is defined as the information rate (net bit rate) over

the bit rate, and γ is the analogue to digital convertor (ADC) resolution for the analogue sensor signal amplitude; here γr is the required information rate for transferring the sensor data. Thus, $b_W > b_r$ shows that the channel can transmit the sensor data completely.

3.1.4 Results and Discussion

The key issue for employing a periodic fast fading channel is whether it can sustain a sufficient sensor sampling rate. As shown above, the sensor data rate should be smaller than the bit rate. In turn, the bit rate is related to the CWR. In a real application, besides the factors discussed in Problem Definition, CWR depends on the LED's maximum radiation angle, the rotation radius of the LED and the distance between the LED and the photodiode. Smaller radiuses extend the communication window, but in practice the specific placement of the devices restricts it. Since CWR depends on a number of parameters and is too difficult to be defined in a general manner, here it is assumed conservatively that it is 1:1000. A more precise model that considers more parameters is presented in Appendix I, in which the CWR can be estimated if the required parameters are given.

The channel is considered in an environment with high speed of rotation and set up a reference using the following parameters, as shown in Table 2. The consequent bit power $P_R T_b$ of a communication window for a transmission bandwidth of 1 MHz is shown in Fig. 3.1.5. For a speed of 3000 rpm and $\mathrm{CWR} = 10^{-3}$, the period of a rotation cycle is 20 ms and the communication window is 20 μs. In the following sections, the influence of some of the parameters from the table above on the channel performance and its optimization is considered.

There are two typical examples for sensor data acquisition and ADC [30, 36]. The first is sampling the sensor intermittently between certain intervals, and converting the collected data to digital signals to be transferred. An example is the temperature detection in [30], in which the sampling rate of temperature sensor is 10 Hz with 10 bit ADC resolution. According to (3.1.22), the required bit rate for this sensor sampling

working on the periodic fast fading channel is 200 bit/s. The second example is non-stop sensor sampling and collecting continuous analogue signal, in which the data is modulated at the frequency of the digital signals. An example involving torque measurement is shown in [36], in which the ADC sampling rate is 10 kHz, resulting in a Nyquist bit rate of 20 kbit/s.

Parameter	Value
A_r	1 mm^2
CWR	1:1000
T_n	300K
P_E	25 mW
D	0.2 m
η	0.89
IR LED wavelength	850 nm
C_d	11 pF
n	20
Rotational Speed	3000 rpm

Table 2 The parameters used as the reference setup
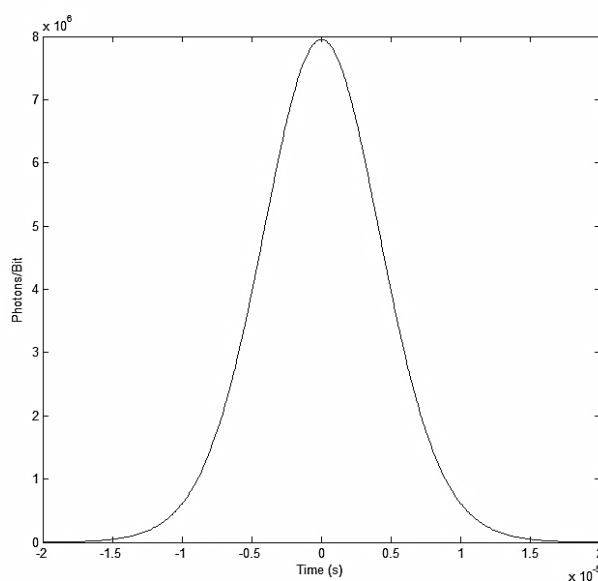
Fig. 3.1.5 The sample of communication window for a transmission bandwidth of 1 MHz

1.   Load resistor front end and temperature effect

Assuming all other parameters to be constant, this section considers only the influence of the load resistor (R_L in Fig. 3.1.4) and bandwidth on the bit capacity of the channel. By calculating the resulting bit capacities from the combination of values, for which the range of R_L is from 50 Ω to 500 kΩ and the bandwidth range is from 100 kHz to 100 MHz, the optimal values can be found. In Fig. 3.1.6, two bandwidth limiting effects are shown: (i) the cutoff frequency for higher resistor values and (ii) the power requirement for the dedicated error rate, resulting in lower bit capacity for lower resistor values at higher bandwidth. The 110 Ω of R_L represents an optimal value for the load resistor for this channel. Since higher R_L values translates in lower bandwidth as the resistor value increases in a certain Gain Bandwidth Product (GBW). But the bit capacities of values lower than 110 Ω decrease eventually as bandwidths increase, the peak bit capacities of these R_L values appear in lower bandwidths. A special case should be pointed out in the fast fading channel, which is shown in Fig. 3.1.7 (a).
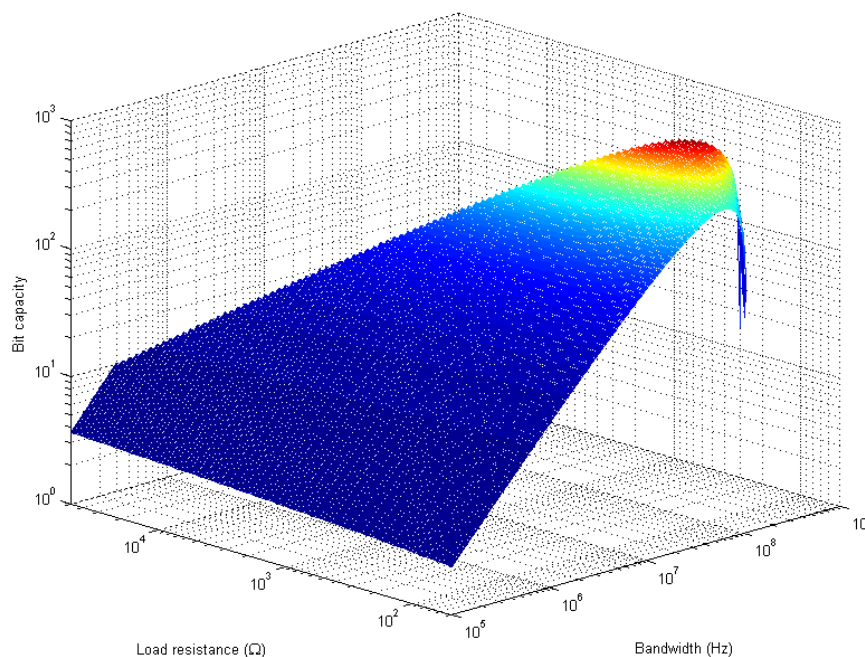
Fig. 3.1.6 Bit capacities for different load resistors and bandwidths
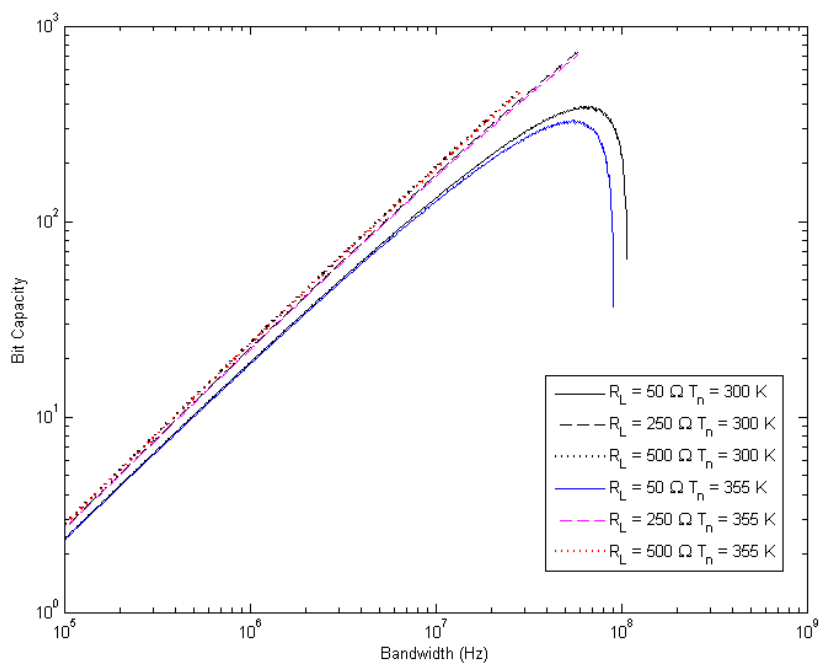
(a)
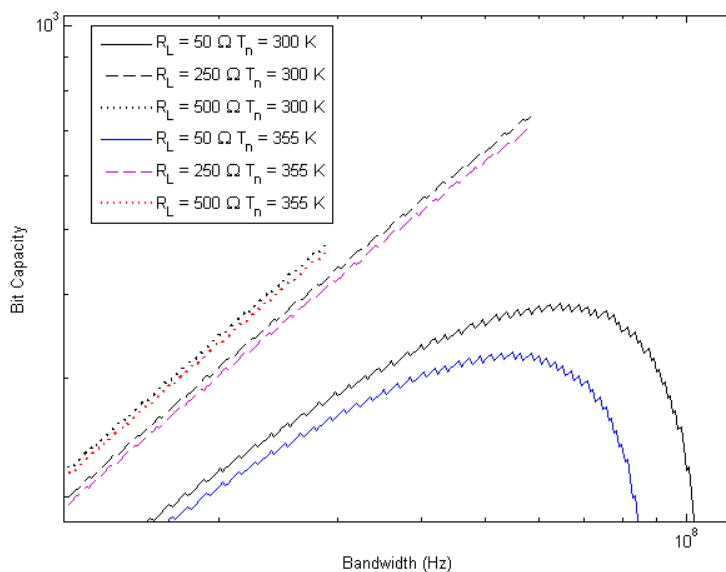
(b)

Fig. 3.1.7 Bit capacities of channels with load resistors 50 Ω, 250 Ω and 500 Ω

The black lines of bit capacities of the three resistor values, namely 50 Ω, 250 Ω and 500 Ω, are extracted from those in Fig. 3.1.6. The bit capacity for 250 Ω and 500 Ω can be higher than that for 50 Ω, even if the bandwidth is lower. The bit capacity for 50 Ω is affected by insufficient power, and the bandwidth extension of the channel requires higher emitted power or shorter distance between DT and DR to enhance received

power. The bandwidths for 250 Ω and 500 Ω are cut off due to the -3 dB frequencies, in which the frequency response can be compensated by amplifiers, as described in section 2.2.3. As a result, the channel performance improvement from bandwidth is more effective for high load resistors. There is a trade off in increasing power consumption, either spent on the LED emitted power or the power for the additive amplifier, since the amplifier constant power may be more than the intermittent extra power needed on the LED.

What is more, Fig. 3.1.7 also shows the temperature effect on the channel, considering the increase on temperature raises the thermal noise level. As mentioned in section 2.3.2, the temperature of the motor interior can be 80 ℃. The non-black lines show the results of which the temperature of the receiver front end is modified to be 355 K (from the original 300 K).The temperature rise of 55 K only generate remarkable difference in the 50 Ω channel when approaching the peak bit capacity value, since the channel is more sensitive to the raised thermal noise level compared to the 250 Ω and 500 Ω (Please refer to Fig. 3.1.7 (b) for a clear comparison of the differences at peak values.).

Emitting more power from the LED directly increases the bit capacity of the channel for any load resistor. However, in a real application, the wireless DT is mounted on the rotor, which means it must be powered either by battery or from energy harvested from the environment. Therefore, the power supply on the DT is critical and the transceiver system needs to be power efficient.

Fig. 3.1.8 indicates how the channel can be improved by increasing the power of the emitting LED from 10 mW to 50 mW. The improvement is more significant for the 50 Ω channel. The results show that the 50 Ω channel overtakes the other two with higher resistors at about 37 mW. In another aspect, it also shows that the performance improvement resulting from the emitted power becomes less effective as the load resistance is higher.
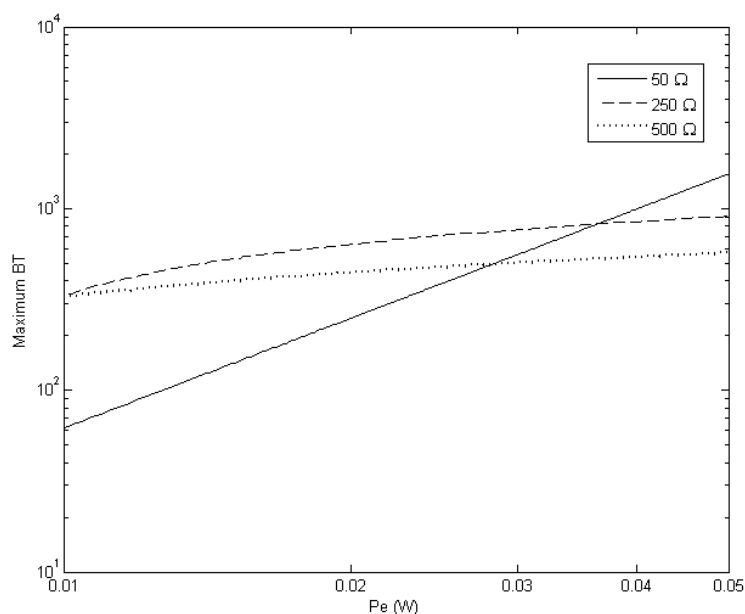
Fig. 3.1.8 Maximum bit capacities (BT) of channels with load resistors 50 Ω, 250 Ω and 500 Ω on emitter power from 10 mW to 50 mW

Taking the power efficiency into account, Fig. 3.1.9 shows the distribution of the maximum bit capacities of the channels with load resistors of 50 Ω, 250 Ω and 500 Ω in the energy per bit scale. The energy usage of the channel with low resistor (lower than 110 Ω in Fig. 3.1.6) is different to that cut off by the -3 dB frequency. The energy per bit decreases when the maximum bit capacity increases for the 50 Ω channel, which is more power efficient when less energy is invested in a bit. On the contrary, energy consumption tends to be higher at higher bit capacities for the 250 Ω and 500 Ω channels. Therefore, for achieving the best performance in the channel, lower load resistors are more power efficient.

In a real application, the power efficiency needs to be considered in another way. To preserve power, a good way is to find out which channel brings more benefit when consuming the same power to transmit the same amount of data. The power and bandwidth combination of the three channels to achieve the same bit capacity with the same power efficiency are shown in Fig. 3.1.10, in which the curves of the three channels at the 20 kbit/s bit rate in [36] are indicated. The straight line represents the 10^{-9} J energy per bit. The intersections of the straight line and the curves are the power

and bandwidth combinations of the three resistors at 20 kbit/s using the same energy. Higher resistance requires lower emitted power and less bandwidth, which means possibly greater distances between the DT and the DR.
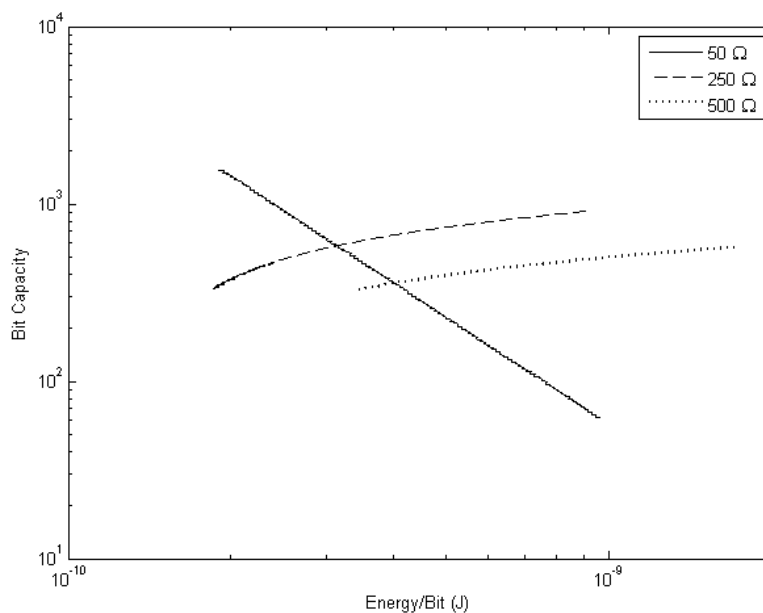
Fig. 3.1.9 Power efficiency distribution of maximum bit capacities of channels with load resistors 50 Ω, 250 Ω and 500 Ω
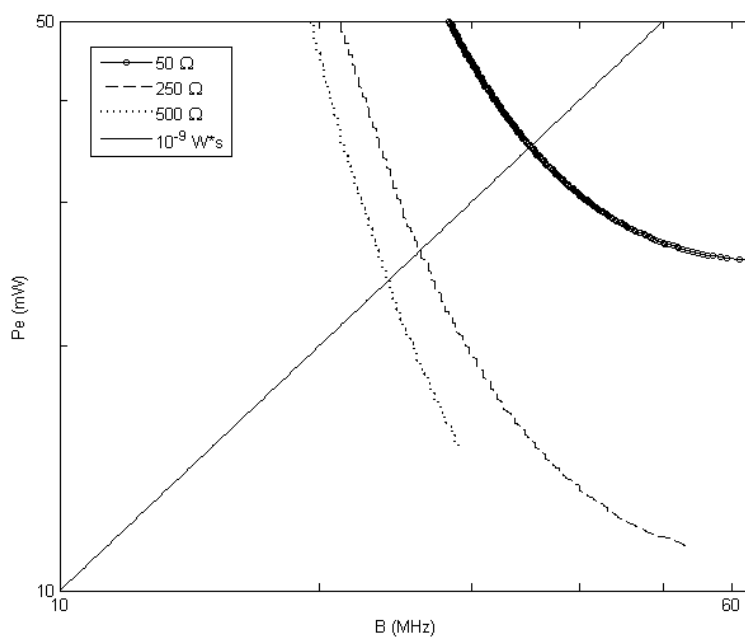
1`

Fig. 3.1.10 Power and bandwidth combinations of channels with load resistors 50 Ω, 250 Ω and 500 Ω at bit rate of 20 kbit/s

2.   LED beam width and distance

The modification of the LED beam width and the distance between the LED and the photodiode can result in more power allocated per bit and thereby higher bandwidths without increasing the emitted power. Nevertheless, the sacrifice is the width of the communication window, because the power is more concentrated.

A higher Lambertian mode number *n* generates a narrower beam width with the same radiation power. In Fig. 3.1.11, the communication channel of several LED beam widths and the related bit capabilities for a 50 Ω load resistor are shown. The channel using a wider LED beam generates a longer communication window, resulting in higher bit capacities for lower bandwidths. For higher bandwidths, the power concentrated narrow beams have higher bit capacities since they can allocate more power into each bit.
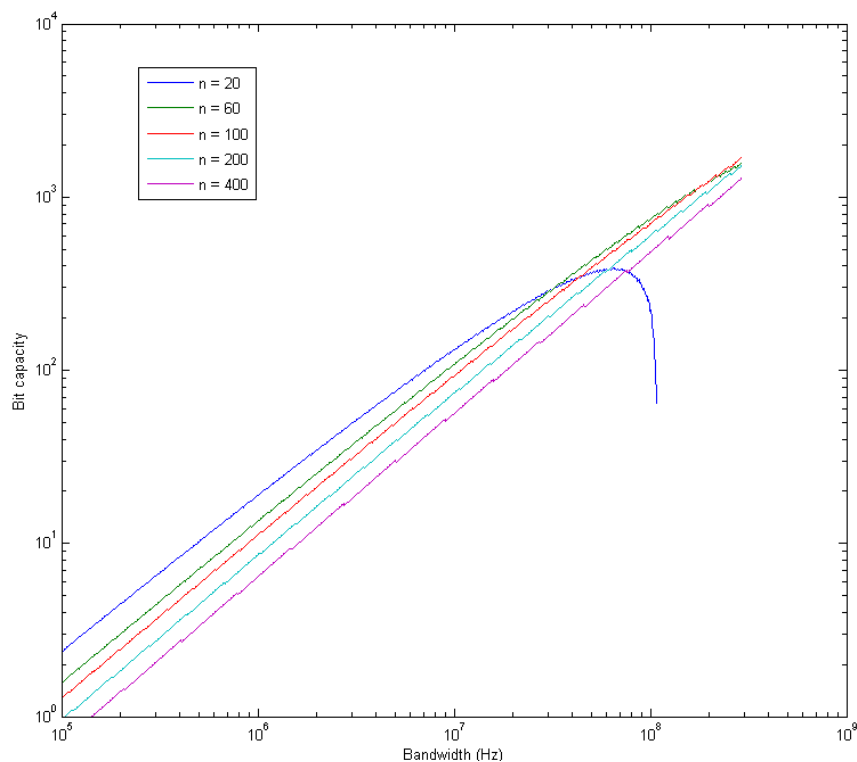
(a) Bit capacities of different bandwidth on different beam widths
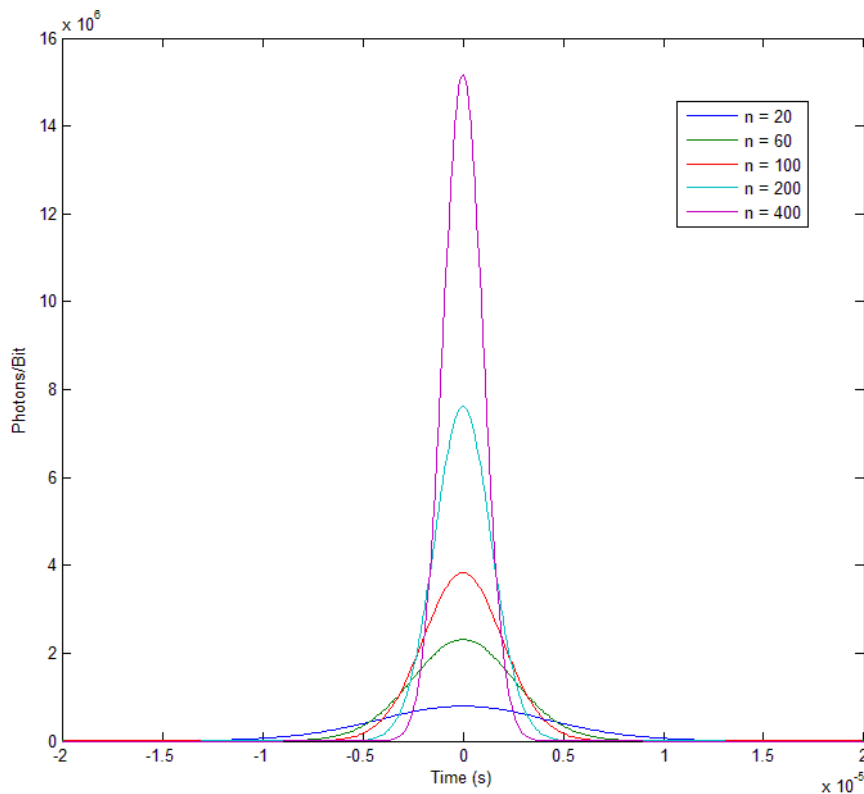
(b) The communication windows of different beam widths

Fig. 3.1.11 Effects of LED beam width on bit capacity; $R_L = 50\,\Omega$.

For the received signal of the model, higher power intensity results in higher possible bandwidth but shorter communication window. The strategy of LED selection with respect to the beam width depends on the bandwidth required. Those narrow beam LEDs, allowing higher power intensity to the received signal, are only necessary to provide a higher bandwidth, which is not available on wide beam ones. Moreover, the adoption of a laser (with its narrow beam) is only necessary when the bandwidth demanded is beyond the capability of LEDs. The distance D between the LED and the photodiode affects the bit capacity, which has been shown in (3.1.6). The diffusion of radiation power results in wider beam width and lower power intensity as distance increases, as a result, the effect of a shorter distance is similar to that of a narrower beam.

Fig. 3.1.13 and Fig. 3.1.13 show the results for bit capacity versus distance and bandwidth for load resistors 50 Ω and 500 Ω.
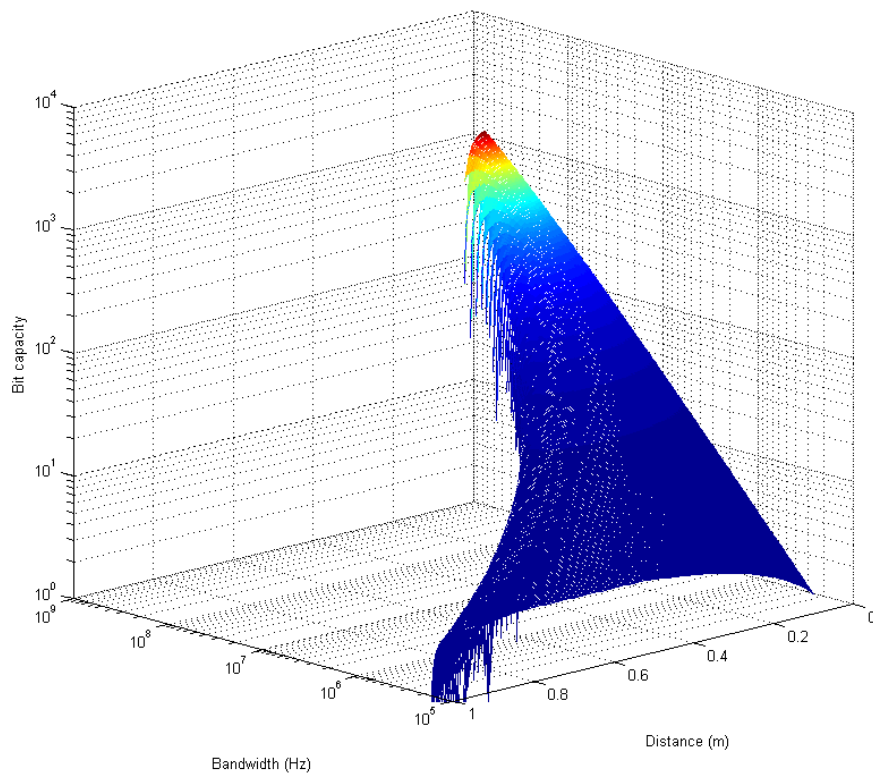
Fig. 3.1.12 Distance effect of 50 Ω on bit capacity.
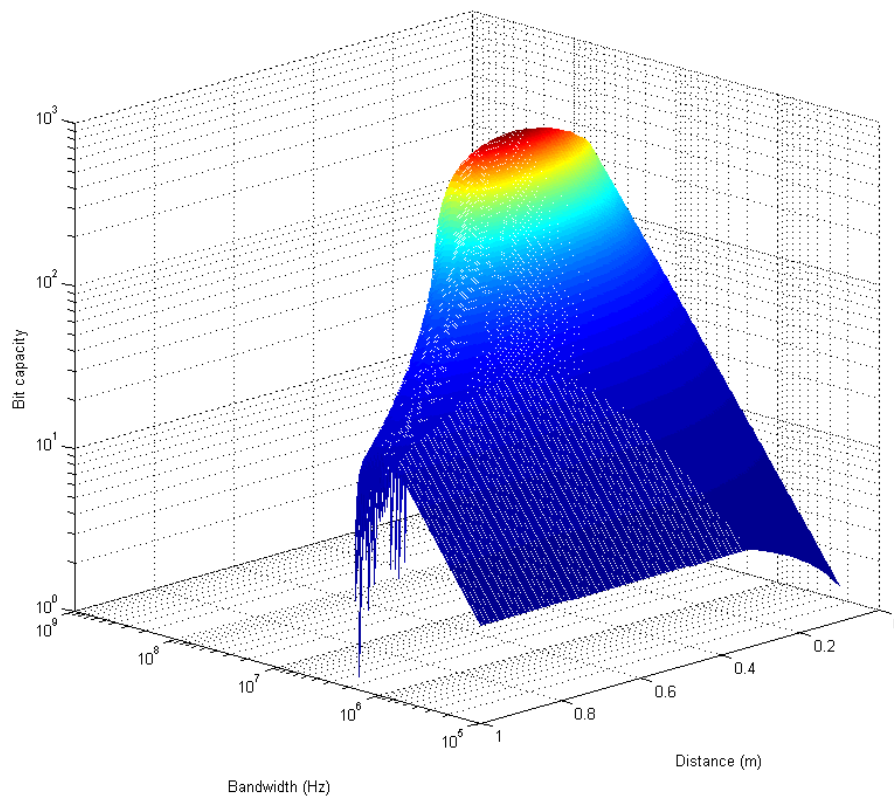
Fig. 3.1.13 Distance effect of 500 Ω on bit capacity.

In the receiver with 50 Ω load resistor, the bit capacity is highly sensitive to distance and drops significantly as distance increases. In contrast, the bit capacity with 500 Ω can sustain longer distances with a satisfactory performance.

3.   Summary

In Fig. 3.1.14, a summary of the bit capacity improvements from all the effects described above, is shown in comparison with the benchmark channel with 50 Ω load resistor (all parameters for the benchmark are given in Table 2). These improvements can be split into two categories using the benchmark as a boundary. On one hand, increasing the load resistance and the LED emitted power both result in absolute improvement on channel performance, showing performances that are always above the benchmark. On the other hand, extending the bandwidth with narrowed LED beams and shorter distances between the LED and the photodiode, since the communication windows become shorter, the bit capacity can only be enhanced in the bandwidth range that is higher than the cutoff of the benchmark channel.
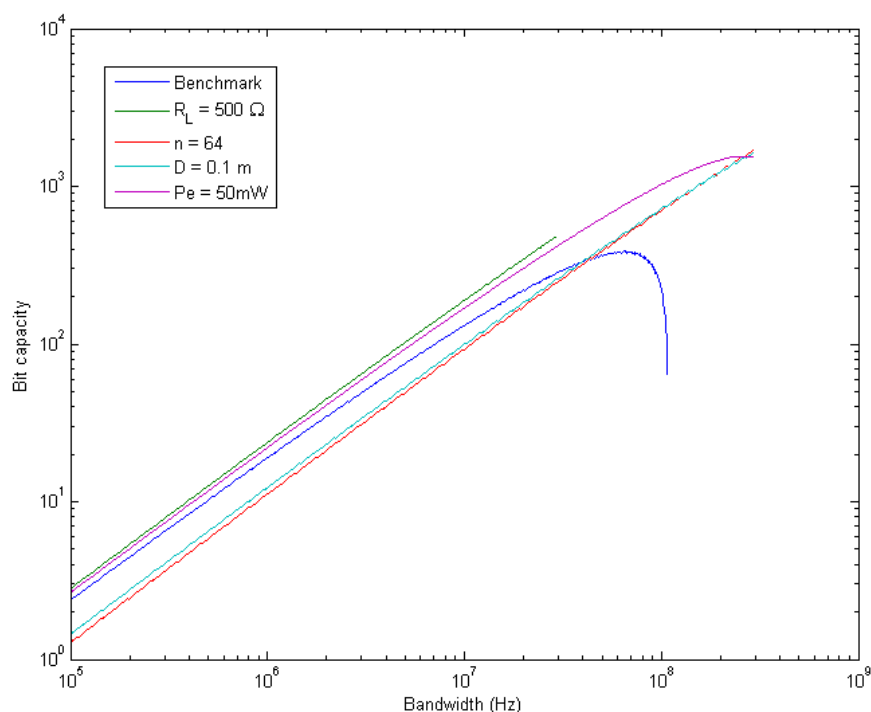
Fig. 3.1.14 Bit capacity improvement from different effects compared to the benchmark channel

The bit rates corresponding to the bit capacities shown in Fig. 3.1.14 can be

generated using (3.1.21). The maximum bit rate of the benchmark is the 15 kbit/s at 56 MHz. This can be enhanced to 22 kbit/s at 29 MHz by changing the load resistor from 50 Ω to 500 Ω. At 72 MHz, the increased power level of 50 mW gives the best value, equal to 78 kbit/s. Changing to a narrow LED beam width and shortening the distance between LED and photodiode from 0.2 m to 0.1 m produce similar results, delivering bit rates of around 80 kbit/s.

Therefore, the periodical fast fading channel is able to sustain the data rates similar to those presented in [30] and [36], which are 200 bits/s and 20 kbits/s. Theoretically speaking, the channel with fast fading signal power will maintain the sampling rate of a 10 bit resolution ADC at 4 kHz, when the channel capacity is 0.5.

3.2   Amplifier Performance

Because the IR LED radiation is diffusive and the power in the radiation centre is higher, a large signal fluctuation is introduced in the received signal when the receiver photodiode passes across the front of the transmitter LED. The significant signal fluctuation causes two problems in the signal processing when optical signals are converted into electronic signals. On one hand, if a large amplitude difference is introduced in the electronic signal, the valid communication session may be narrowed if not all the amplitudes of the signals are within the input region that amplifier can produce linear gain, as signals with too high or too low amplitudes may be seriously distorted and become unusable. On the other hand, for higher signal frequencies approaching the -3 dB frequency of the photodiode front end, the response of the photodiode to the incoming IR signal has significant influence on the received pulse shape; when these amplitude varied signal pulses are threshold with a certain level in the signal processing circuit, considerable width difference may occur between pulses, which causes unexpected pulse edge position shifts in time. To a digital communication system that uses pulse edges for synchronization and symbol recognition, the width difference may lead to failure of synchronization or additional bit errors.

The influence of signal fluctuation can be reduced by applying an AGC amplifier.

However, since the load resistor and the bandwidth determine the converted voltage signal amplitude from the photodiode output current, as well as noise level and threshold, the receiver front ends with different load resistors produce different signal amplitudes. Therefore, the performance of the AGC amplifier is also affected by the selection of load resistor and bandwidth.

3.2.1 Amplitude Difference of Fast Fading Signal Power

1. The Dynamic Range

The optical pulses with fast fading power are converted to electronic current in the photodiode front end. Considering a circuit of photodiode front end, the converted voltage from the load resistor is:

$$V = \frac{q\eta P_R}{hf} R_L \tag{3.2.1}$$

As described in section 3.1.4, the lowest threshold for the fast fading channel can be 4.76σ suggested using Saddlepoint approximation for retaining a 10^{-6} error rate for bit '0'. Therefore the minimum power that drops the error rates of bit '1' to 10^{-6} is 9.52σ, based on the same method. And from (3.1.2), the maximum received power corresponds to the moment when the photodiode is facing directly the LED:

$$P_{R(\text{max})} = \frac{n+1}{2\pi D^2} P_E A_r \tag{3.2.2}$$

The dynamic range of the corresponding electric signals is:

$$\frac{V_{in(max)}}{V_{in(min)}} = \left(\frac{q\eta P_{R(\text{max})}}{hf}\right) \Big/ 9.52\sigma B \tag{3.2.3}$$

Solving (3.2.1) with (3.2.2) and (3.2.3) gives:

$$\frac{V_{in(max)}}{V_{in(min)}} = \frac{q\eta(n+1)P_E A_r}{19\pi D^2 hf} \sqrt{\frac{R_L}{2kT_n B}} \qquad (3.2.4)$$

As a result, the dynamic range of the fast fading signals is load resistor and bandwidth dependent because they determine the minimum power for useable signals.

2. Results and discussion

In Fig. 3.2.1 the dynamic range of the three load resistors, calculated using (3.2.4), are shown against the bit capacities, corresponding to a bandwidth between 100 kHz and 100 MHz. A higher load resistor has a lower noise level, therefore pulses with lower amplitude can be used. However, it also produces a higher dynamic range. What is more, extending the bandwidth requires a higher threshold, resulting in a smaller dynamic range. As dynamic range is smaller for higher bandwidth, the combination of higher load resistors and higher bandwidth is the preferred option for reducing the dynamic range for signal amplifying.
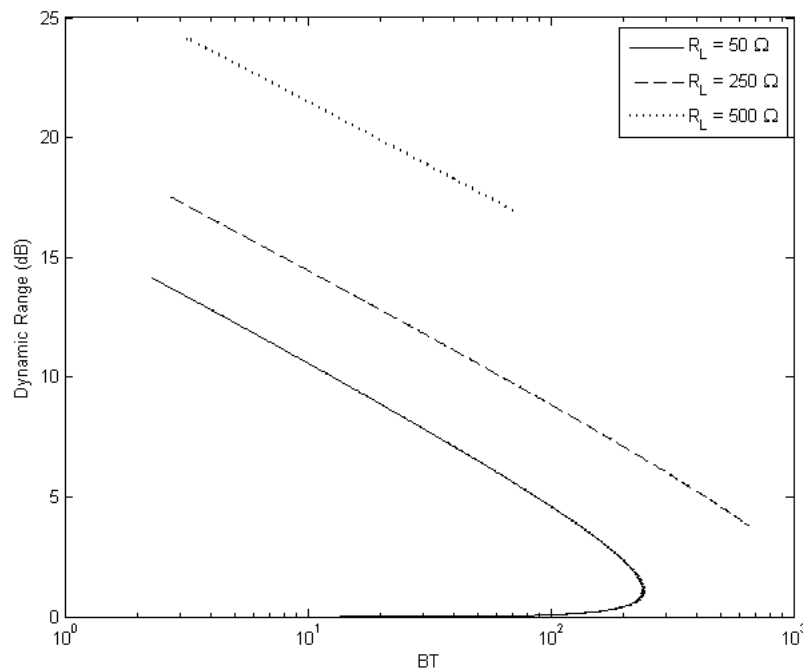
Fig. 3.2.1 Dynamic ranges of channels with load resistors 50 Ω, 250 Ω and 500 Ω with bandwidth ranging from 100 kHz to 100 MHz

3.2.2   The Model for the AGC Amplifier

1.   AGC amplifier model

The AGC model is illustrated by the block diagram shown in Fig. 3.2.2. The gain of the variable gain amplifier (VGA) is controlled by the product of the feedback gain control input V_c and a constant gain K_1, in which V_c is low pass filtered from the difference V_d between V_{out} and a reference V_{ref}, extracted by the envelope detector. The low pass filter in this case is the integrator that the transfer function is $\frac{K_2}{s}$. According to [89] and [91], the response of the envelope detector is:

$$H_e(s) = \frac{K_d q_e}{s + p_e}$$

(3.2.5

Assuming V_{out} is at lower frequency than the pole frequency of the envelope detector, the gain of the envelope to V_{out} is $\frac{K_d q_e}{p_e}$. Therefore V_d is:

$$V_d = \frac{K_d q_e V_{out}}{p_e}$$

(3.2.6)

The relation between the input and output of the AGC amplifier can be described as [86, 88]:

$$\frac{dV_{out}/V_{out}}{dV_{in}/V_{in}} = \left(1 + FV_{in} \frac{dP}{dV_c}\right)^{-1}$$

(3.2.7)

in which F is the gain of the feedback loop in Laplace transform and P is the VGC gain, in the model:

$$F = \frac{K_2 K_d q_e}{s p_e}$$

(3.2.8)

$$\frac{dP}{dV_c} = K_1 \qquad\qquad (3.2.9)$$

Solving (3.2.7), (3.2.8) and (3.2.9), the output of the AGC amplifier to a small input signal change is as follows:

$$\Delta V_{out} = \frac{\Delta V_{in} V_{out} e^{-KV_{in}t}}{V_{in}} \qquad\qquad (3.2.10)$$

where $K = \frac{K_1 K_2 K_d q_e}{p_e}$, represents the AGC loop gain.
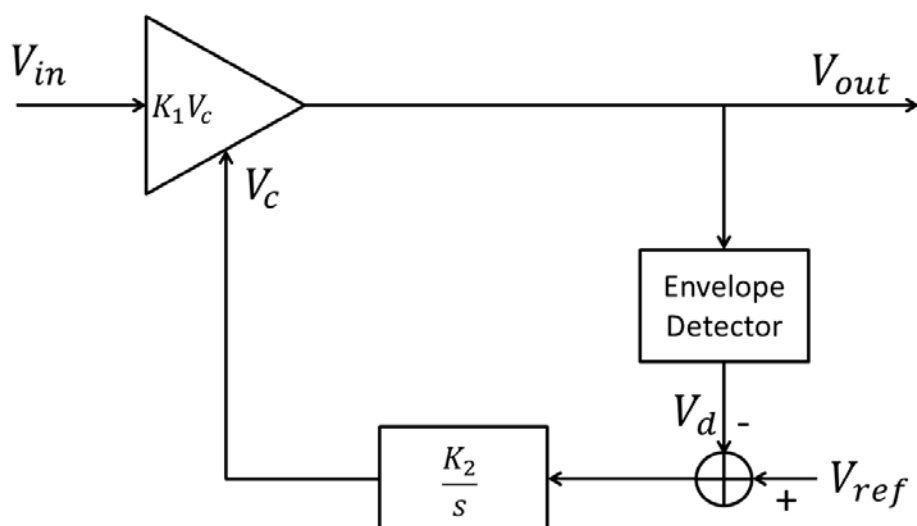
Fig. 3.2.2 The model for the AGC amplifier

Therefore, the expression of the signal power in the AGC amplifier can be obtained using an iterative method indicated in (3.2.8) when the initial condition is defined and the boundaries are given. For a real circuit component, the range of values for V_c of the VGA is limited by the sensitivity and gain linearity. The boundaries based on the AGC operational gain can be:

$$g_{VGA} = (K_1 V_{cmin}, K_1 V_{max}), \left(V_{max} = \min(V_{cmax}, V_p)\right) \qquad (3.2.11)$$

in which V_p is the power supply voltage, because the maximum output from an

operational amplifier (Op-amp) integrator is the power supply voltage, by which the AGC gain will be further limited if the V_{cmax} is higher than V_p. If V_{in} produces $V_c < V_{cmin}$, g_{VGA} stays at $K_1 V_{cmin}$, likewise, $g_{VGA} = K_1 V_{max}$ when $V_c > V_{cmax}$.

      Here V_{in} is assumed the output voltage of the load resistor front end when the LED emits optical signals with constant power in the communication window. The ideal relation between V_{in} and V_{out} of the AGC amplifier with an operative range from V_1 to V_2. is shown on the left of Fig. 3.2.3. To match the dynamic range of V_{in} on the right of the Fig. 3.2.3 in this range, the preferred value is $V_{in(min)} = V_1$. If $V_{in(max)} < V_2$, the gain of V_{out} in the communication session is under the control of the AGC amplifier.
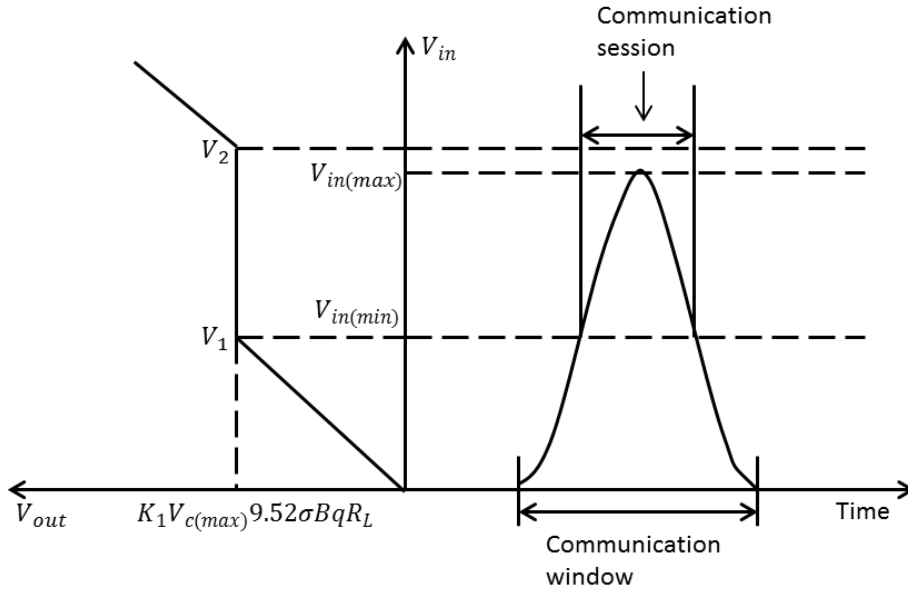
Fig. 3.2.3 The ideal relation of AGC amplifier voltages and communication session signal voltages

Here V_1 is referred to the integrator input $V_{ref} - V_d$. As V_{in} becomes higher, when $V_{ref} - V_d < 0$, the integration decreases and results in the reduction of V_c, which produces a smaller g_{VGA} and the increase of V_{in} is controlled. Therefore in ideal circumstances, V_1 is at the point $V_{ref} = V_d$, and the relationship among V_d, V_{out}^0 and V_{ref} can be found:

$$K_1 V_{in(min)} V_{c(max)} = V_{out}^0 \tag{3.2.12}$$

$$V_{ref} = V_d = \frac{K_d q_e V_{out}^0}{p_e} \tag{3.2.13}$$

Removing V_{out}^0:

$$V_1 \geq V_{in(min)} = \frac{p_e V_{ref}}{K_1 K_d q_e V_{c(max)}} \tag{3.2.14}$$

Due to the cumulative effect of the integrator, there is a time delay between the negative input appears to V_c, and V_c is reduced to the value that the VGA maintains a stable output, resulting in $V_1 > V_{in(min)}$. The period of this delay depends on the integrating speed that can be reflected in (3.2.10), in which KV_{in} is the relevant time constant. The higher boundary V_2 is at the level where g_{VGA} reaches the minimum value $K_1 V_{c(min)}$.

To achieve an entire gain controlled amplification from the signal received by the photodiode, $g_{VGA} = K_1 V_c$ must at least offer a larger gain control input range from V_1 to V_2 than the dynamic range from $V_{in(min)}$ to $V_{in(max)}$. From the ideal condition, the desired output must satisfy (3.2.12) and

$$K_1 V_{in(max)} V_{c(min)} = V_{out}^0 \tag{3.2.15}$$

Therefore,

$$\frac{V_{in(max)}}{V_{in(min)}} \leq \frac{V_{c(max)}}{V_{c(min)}} \tag{3.2.16}$$

Which means the dynamic range of the input signals should be smaller that of the VGA sensitivity.

The key factors of AGC amplifier in the fast fading channel can be summarized as:

1. The ideal V_1 starts at the input voltage level that satisfies the error rate,

$$V_{in(min)} = \frac{p_e V_{ref}}{K_1 K_d q_e V_{c(max)}}$$

2. The VGA should be able to provide a gain control input range as shown in (3.2.16) to match the signal dynamic range in the communication session in the operational range of the VGA.

3. The performance of the amplifier depends on the loop gain K in (3.2.10), which determines the response to signal change and the actual V_1.

3. Results and discussion

The AGC amplifier input (V_{in}) from the 250 Ω load resistor, the output (V_{out}) and the relative desired output level ($K_1 V_{in(min)} V_{c(max)}$) are shown in Fig. 3.2.4. The role of the AGC amplifier to reduce the dynamic range of the signals within the communication session and to maintain the output amplitude constant when the input is changing creates a flat top signal shape. This flat top level is determined by the value of V_1. The difference between the flat top level and the desired output level reflects the difference between V_1 and $V_{in(min)}$.

As discussed in the model, the time delay that resulting in $V_1 > V_{in(min)}$ depends on the integrator time constant KV_{in}. Assuming the communication between the DT and the DR happens only in the period that the output of the AGC amplifier is stable. If the low loop gain results in a long delay in the communication session, the bit capacity will be affected. The relations of the loop gain K and the delay ratio $r_D = \frac{Delay}{Communication\ session}$ for the load resistors 50 Ω, 250 Ω and 500 Ω are shown in Fig. 3.2.5. When reaching the same bit capacity, r_D for higher load resistor starts decreasing at lower loop gain than lower load resistor.
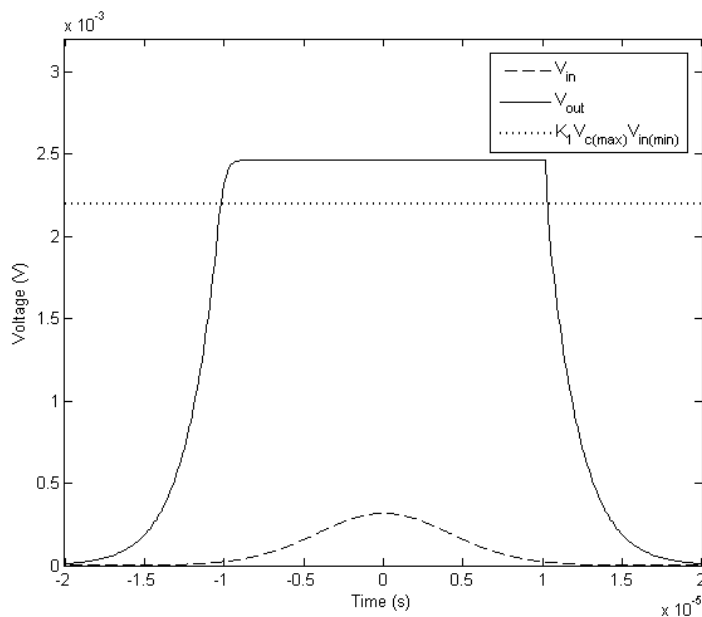
Fig. 3.2.4 The amplitudes of the V_{in} and V_{out} and $K_1 V_{in(min)} V_{c(max)}$ in time
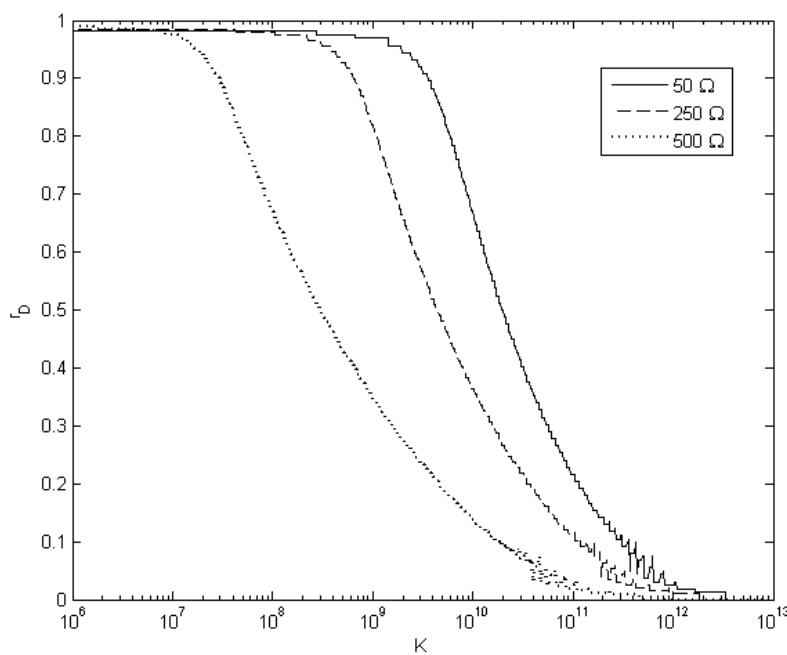
Fig. 3.2.5 AGC loop gain and delay ratio of channels with load resistors 50 Ω, 250 Ω and 500 Ω at a bit capacity of 50 bit

3.2.3   Transimpedance Amplifier

From the conclusions of the previous two sections and section 3.1, increasing the load resistance value results in a trade off for the bit capacity since the bandwidth will be more limited. If the bandwidth of channels with higher resistors can be extended, the loss of bit capacity will be compensated and higher resistors will be more desirable since the noise is lower, therefore the distance between the DT and the DR can be longer. The required loop gain of the AGC amplifier is lower. What is more, the case that the application requires a longer distance than the range of the low load resistor but a bit capacity that high load resistor cannot achieve, the bit capacity of the high load resistor front end needs to be increased. Therefore applying a TIA in the photodiode front end may be a better option to expand the bandwidth. However, as the bandwidth extension granted by the TIA is limited by the gain of the Op-amp [80, 83], described in section 2.2.3, in the following section a model is introduced to estimate the enhancement of bit capacity from the TIA.

1. The model of TIA

A simplified Op-amp based TIA model is illustrated in Fig. 3.2.6, with the corresponding equivalent circuit for the amplifier noise shown in Fig. 3.2.7.
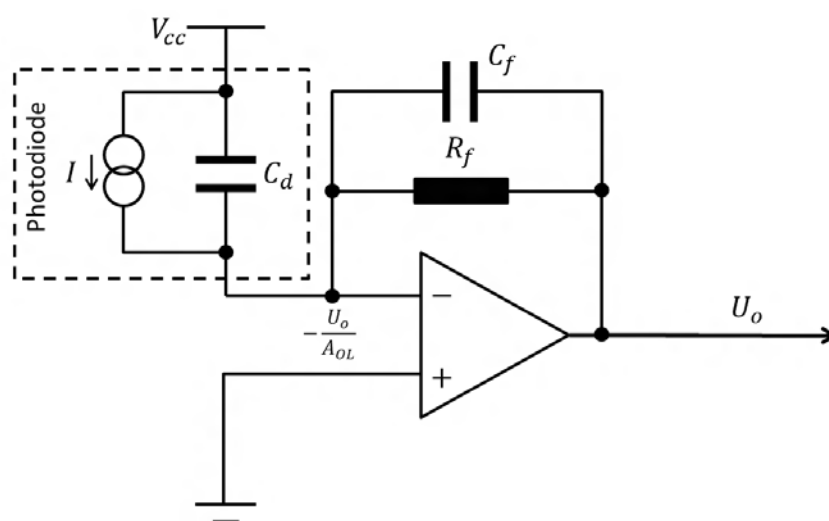
Fig. 3.2.6 A simplified transimpedance Op-amp amplifier model
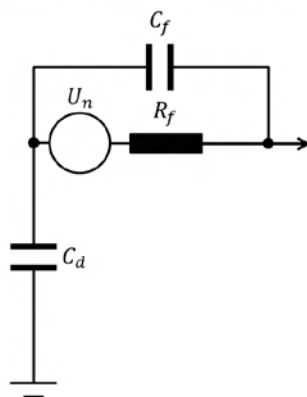
Fig. 3.2.7 Equivalent circuit for the noise of the amplifier in Fig. 3.2.6

Here the input capacitance of the Op-amp is assumed to be small compared to that of the photodiode and can be neglected. According to Kirchhoff's law, the current function of the Op-amp inverted input (where the voltage is $-\frac{U_o}{A_{OL}}$.) is

$$\frac{U_o}{\frac{R_f}{1+sR_fC_f}\left(\frac{A_{OL}}{1+A_{OL}}\right)} = -I + \frac{U_o sC_d}{A_{OL}} \qquad (3.2.17)$$

From the fact that $\frac{U_o sC_d}{A_{OL}}$ is small in value and neglected, (3.2.17) appears in the form as [163, 164]:

$$\frac{U_o}{\frac{R_f}{1+sR_fC_f}\left(\frac{A_{OL}}{1+A_{OL}}\right)} = -I \qquad (3.2.18)$$

in which A_{OL} is the Op-amp open loop gain. In the operating frequency band of the Op-amp, $\frac{A_{OL}}{1+A_{OL}} \approx 1$. Therefore, the transimpedance of the amplifier is given by:

$$g_m = \frac{U_o}{I} = -\frac{R_f}{1+sR_fC_f} \qquad (3.2.19)$$

And the gain of the amplifier to $-IR_f$ is:

$$g = \frac{1}{1 + sR_f C_f} \tag{3.2.20}$$

From (3.2.20), the -3 dB frequency of the TIA output is $\frac{1}{2\pi R_f C_f}$.

The noise current function of the Op-amp inverting input is:

$$\frac{U_o - U_n}{\frac{R_f}{1 + sR_f C_f}} = U_n s C_d \tag{3.2.21}$$

in which U_n is the noise voltage. The noise gain g_n from (3.2.21) is:

$$g_n = \frac{U_o}{U_n} = \frac{1 + sR_f(C_f + C_d)}{1 + sR_f C_f} \tag{3.2.22}$$

Thus, the performance of the amplifier is limited by the feedback capacitor. To maximize the amplifier bandwidth, an optimal value is suggested at the frequency cross point f_X of the Op-amp open loop gain and the noise gain, which is then defined as:

$$C_f = \sqrt{\frac{C_d}{2\pi R_f GBW}} \tag{3.2.23}$$

in which GBW is the gain bandwidth product of the Op-amp.

Considering for an Op-amp a of the frequency response model with one pole, the open loop gain is given by:

$$A_{OL} = \frac{A_0}{1 + \frac{s}{\omega_p}} \tag{3.2.24}$$

in which A_0 is the open loop gain at 0 Hz, ω_p is the pole angular frequency. With the expression of A_{OL} from (3.2.24), the current expressed in (3.2.18) becomes a second order transfer function [165]. The natural frequency ω_o and the damping factor Q of the TIA are [166]:

$$\omega_o = \sqrt{\frac{(A_0 + 1)\omega_p}{R_f(C_f + C_d)}} \tag{3.2.25}$$

$$Q = \frac{\sqrt{\dfrac{(A_0 + 1)\omega_p}{R_f(C_f + C_d)}}}{\omega_p\left(1 + \dfrac{A_0 C_f}{C_f + C_d}\right) + \dfrac{1}{R_f(C_f + C_d)}} \tag{3.2.26}$$

For a detailed analysis of the second order model, please refer to Appendix III. According to [166], when C_f approaches the value derived from (3.2.23), overshooting appears in the signal since $\omega_o \approx 2\pi f_X$, . The solution in [166] suggests that g_m decreases by 3 dB from f_p to f_X, which gives the value for C_f $\sqrt{2}$ times larger than that in (3.2.23):

$$C_f = \sqrt{\frac{C_d}{\pi R_f GBW}} \tag{3.2.27}$$

A simulation result of the TIA front end response is shown in Fig. 3.2.8 in which it is shown that, choosing the value for C_f given by (3.2.27) results in a more effective damping of the overshooting than when C_f is given by (3.2.23). The frequency response of the noise gain can be found in Fig. 3.2.9. The noise gain starts increasing from the zero frequency $f_z = \frac{1}{2\pi R_f(C_f + C_d)}$ to the pole frequency $f_p = \frac{1}{2\pi R_f C_f}$.

The noise condition of the TIA is different from that of the load resistor front end in the circuit model in section 3.1. Due to the RC effect of R_f, C_f and C_d, the noise is not white. According to [62] and [66], the variance of the noise in the TIA becomes:

$$\sigma^2 = T_b^2 \int_0^{\Delta f} \frac{2g_n^2 kT}{q^2 R_f} df \qquad (3.2.28)$$

in which Δf is the noise frequency.

What is more, the excepted value of the shot noise current I_s in the bit time T_b with the expected number of photons m is [66]:

$$\begin{aligned} E[I_s(t)] &= q\frac{m}{T_b} \\ &= \frac{q\eta P_R(t)}{hf} \end{aligned} \qquad (3.2.29)$$
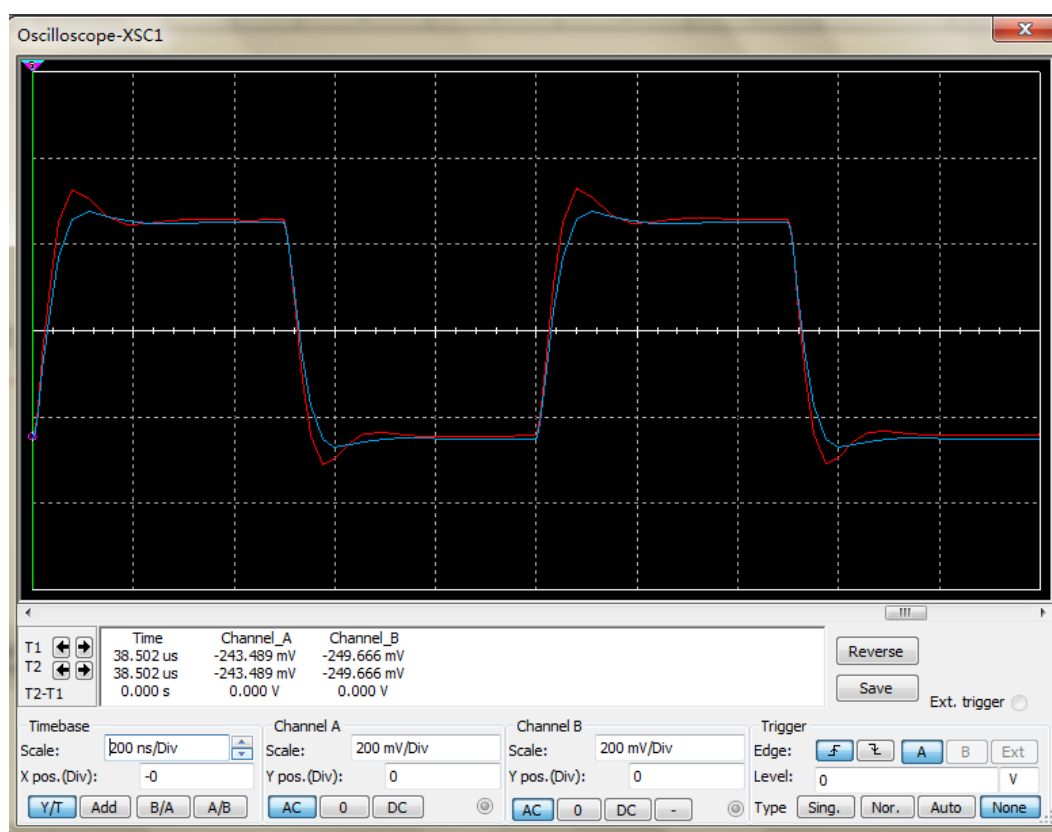
Fig. 3.2.8 Simulation of TIA front end for C_f values given by (3.2.23) (red line) and (3.2.27) (blue line). For the details of the simulation, please see Appendix III)
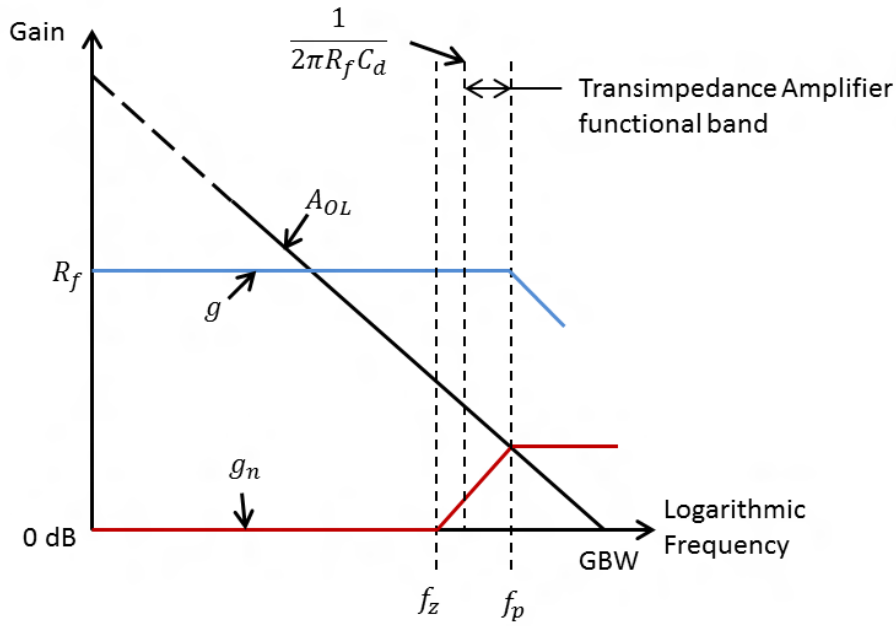
Fig. 3.2.9 The frequency responses of g (blue line) and g_n (red line)

From (3.2.18), for frequencies between 0 and f_p, the transresistance   of the TIA is R_f and is similar to the front end in Fig. 3.1.4, which is R_L. Considering $R_f = R_L$, the actual functional transimpedance amplifying frequency band is from the load resistor cutoff frequency $\frac{1}{2\pi R_f C_d}$ to the pole frequency f_p, of the amplifier, which is also the band in which the noise has increasing gain, as shown in Fig. 3.2.9. As the threshold is determined by the noise level in the periodic fast fading channel, the gain on bit capacity from the extended bandwidth will be counteracted by the raised threshold for higher noise level.

2. Results and discussion

Here the load resistor is used as a benchmark for the TIA in the case of $R_f = R_L$. The estimation introduces 500Ω, 5 kΩ and 50 kΩ resistors for comparison. The value of 50 Ω was not used because the TIA has no effect for lower resistors at higher bandwidth.

The gain of the signal g_m and that of noise g_n from the TIA under different feedback resistors is shown in Fig. 3.2.10 and the feedback capacitors for these resistors from (3.2.27) is shown in Table 3.
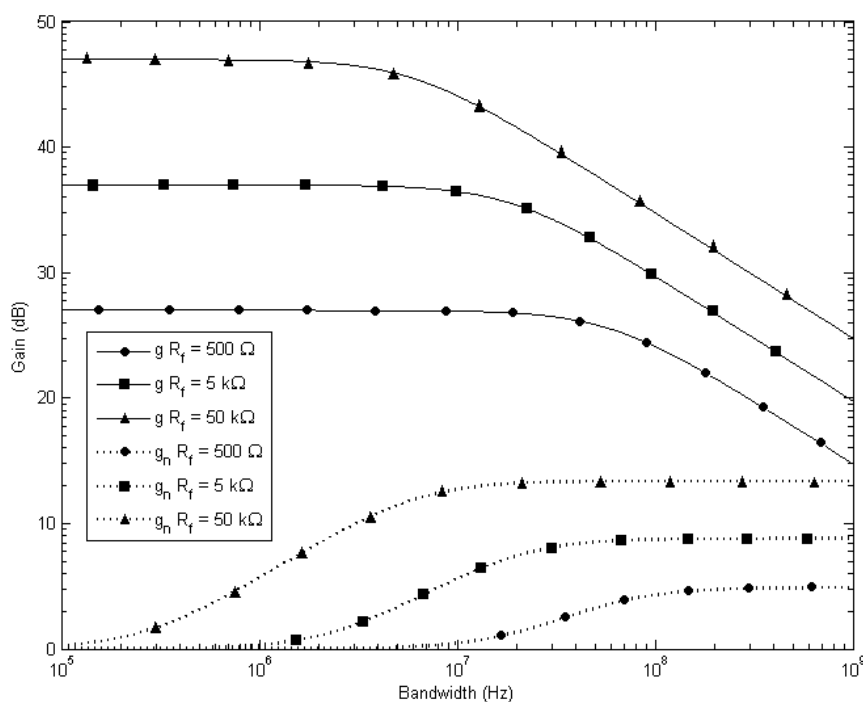
Fig. 3.2.10 Noise frequency responses of TIA with different feedback resistors

R_f	500 Ω	5 kΩ	50 kΩ
C_f	5.3 pF	1.7 pF	0.5 pF

Table 3 The feedback capacitors from (3.2.27)

The noise gain of the higher feedback resistor starts increasing at a lower frequency and is raised to a higher level. This means that, on the extended bandwidth from the TIA, the noise level is higher, which requires a higher threshold than that of the load resistor front end to maintain the same error rate, and the raise of threshold is more significant on higher feedback resistor.

The resulting bit capacities of the feedback resistors are shown in Fig. 3.2.11, with broken lines used for TIA graphs and solid lines for load resistor front end graphs, for the condition that $R_f = R_L$. The extension of bandwidth and the corresponding bit capacity improvement for the TIA is more pronounced for higher resistor values, since the value of C_f cannot be small enough to achieve a higher bandwidth from small values of R_f, as in (3.2.27). From the three channels, this results in a small

improvement on the 500 Ω channel only. The channels with TIA and $R_f = 5$ kΩ and 50 kΩ perform much better than those without. The amplified 50 kΩ channel even exceeded the 5 kΩ that is not amplified. Therefore, the TIA benefits the channels through the fact that the combination of R_f and GBW allows a small value for C_f for bandwidth extension.
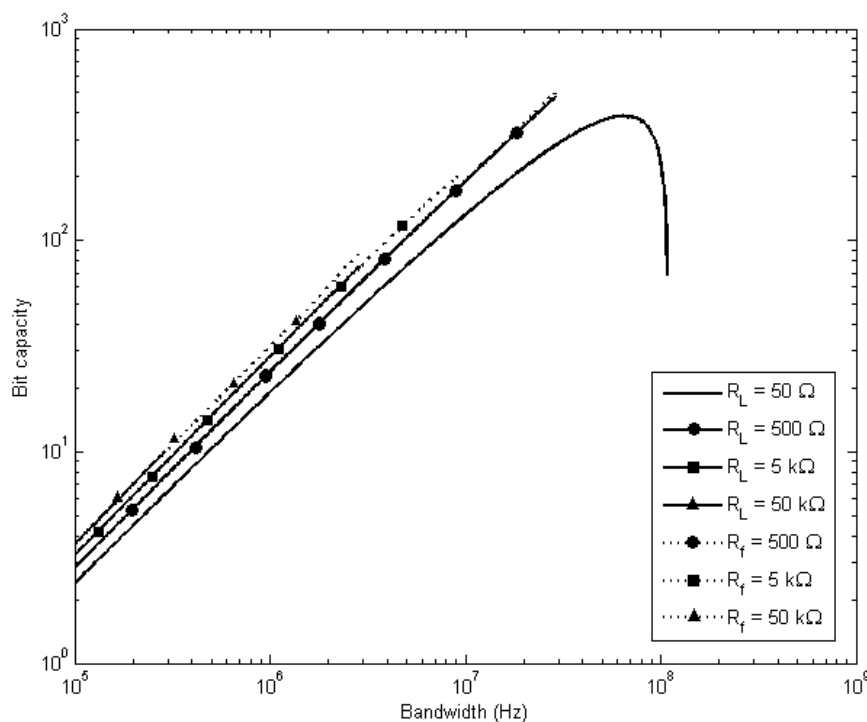
Fig. 3.2.11 The performance comparison of TIAs and front end for different load resistors. Solid lines superposed on broken lines illustrate the performance of load resistor front ends when $R_f = R_L$.

In Fig. 3.2.12, the maximum bit capacities of channels with TIA are shown. In extended bandwidth, the channel with the 5 kΩ load resistor obtains about four times increase in maximum bit capacities, and 50 kΩ increases more than that. In addition, the power usage is more efficient when a TIA is introduced.

But the amplifier does not maximize the bit capacities of the two channels on higher load resistors to reach the required bit rate of 20 kbit/s in Fig. 3.1.10. The benefit of the amplifier goes more to applications that do not require high bit rate for non-stop sampling, in which the channels with higher resistors are still capable of

reaching the required bit rate for the sensor data, they can transfer the same amount of data with equal power consumption as lower resistors, but require less LED emitted power.
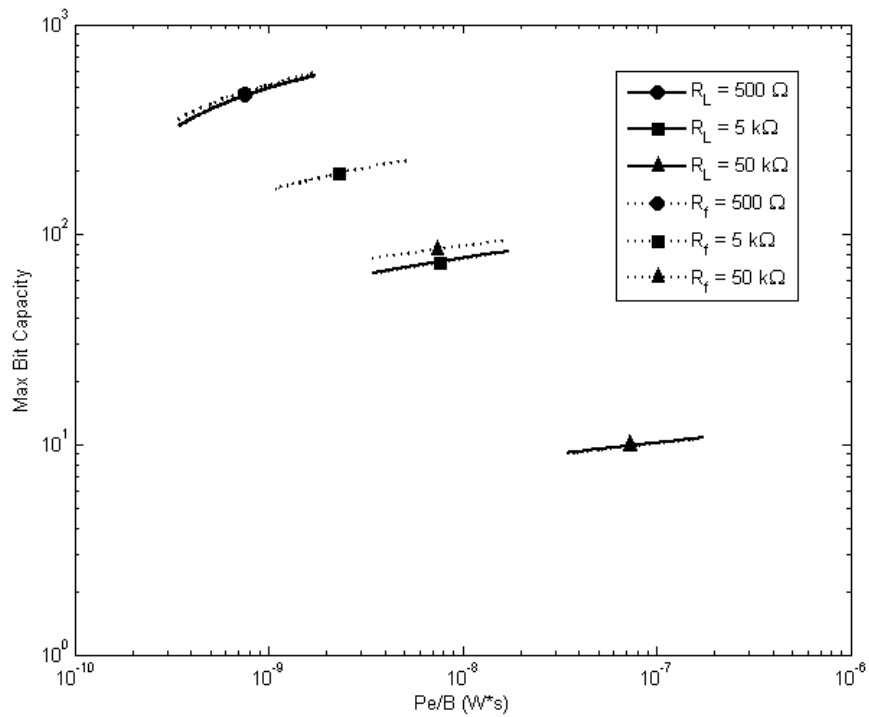
Fig. 3.2.12 Maximum bit capacities of channels with R_L = 500 Ω, 5 kΩ (without TIA) and 50 kΩ and R_f = 500 Ω, 5 kΩ and 50 kΩ (with TIA)

4 Applications

To investigate practically the communication of the intermittent fast fading optical channel, an experimental setup was implemented in a laboratory environment. The difference between the experimental setup and the theoretical model is analysed and the design and function of the IR transceiver circuit for demonstration purposes are discussed. Based on the experimental setup and the transceiver circuit, the technique of detecting the beginning and ending of the communication session is developed and demonstrated, and the power efficiency of the related modulation is discussed. What is more, the key components of programming the baseband protocol on the communication controller are presented. Finally, the results of the circuit, the communication efficiency of the communication controller and the power consumption are shown with discussions.

4.1   Experimental Environment

4.1.1   Hardware Setup

In the examples of the two setups for the OW LOS channel in Fig. 3.1.1, it is shown that the DR is located in a fixed place while the DT is in rotation with the rotor. To simulate the windowed communication in a laboratory environment, an alternative setup is introduced.

The whole setup is shown in Fig. 4.1.1 (Please see Appendix IV for the design of the motor and the disc). Two IR LED and photodiode pairs are installed in fixed positions, where the LED on one transceiver is aligned against the photodiode on the other, forming the LOS optical access. Instead of rotating the transceiver, the periodic channel is represented by spinning a disc between the transceivers, blocking the access for most of the time. A hole drilled in the disc is calibrated to align with the LOS

channel of the transceivers; in each rotation cycle the optical access is only available through the hole in the disc. As a result, the LOS channel for the IR transceivers is available for a short period when the hole allows the optical signals to go through, and signal power varies when the hole moves in the radiation cone, blocking different amount of signal power, which approximates the signal condition in the theoretical model.
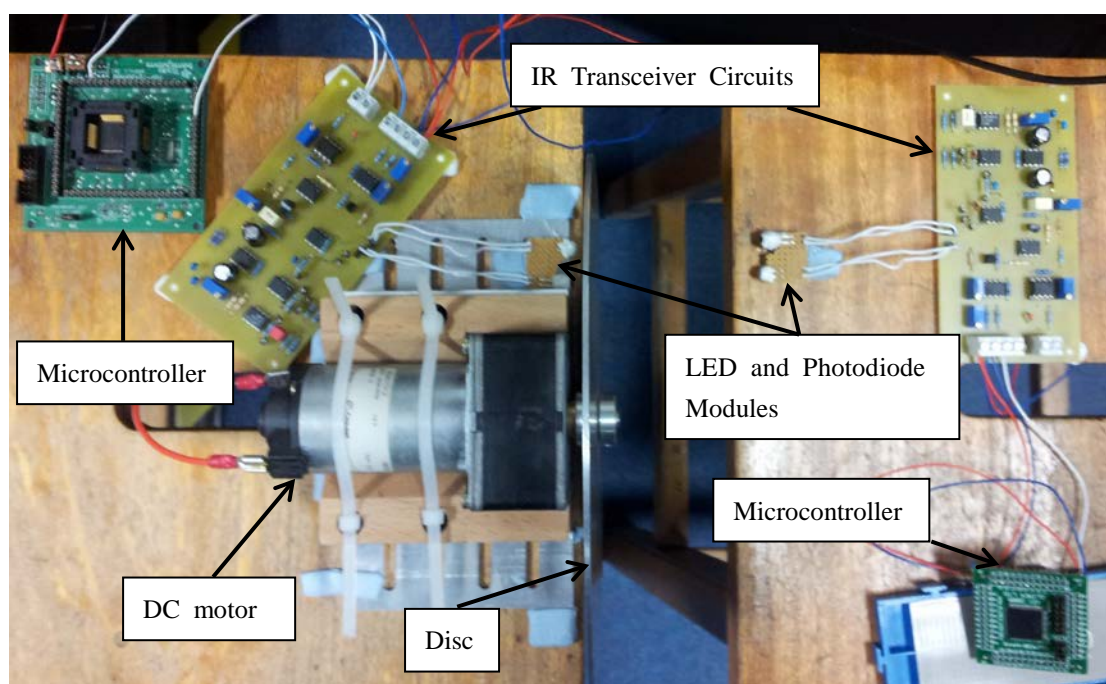
Fig. 4.1.1 The hardware setup for demonstration of the windowed communication.

4.1.2 Analysis of the Difference between Signal Variation in the Experimental Setup and the Theoretical Model

Because the periodic channel is generated using a different configuration in the experimental setup, the variation of optical power received by the photodiode is changed accordingly. The deviation of the optical power variation between the experimental setup and the model can lead to differences in the performance analysis of the signal processing circuits and communication protocols. Therefore, the variation should be investigated and estimated.

Similar to the modelling of the actual optical channel in section 3.1.2 the analysis of the experimental setup also approximates the rotation to a linear motion using a simplified geometry, which is shown in Fig. 4.1.2.
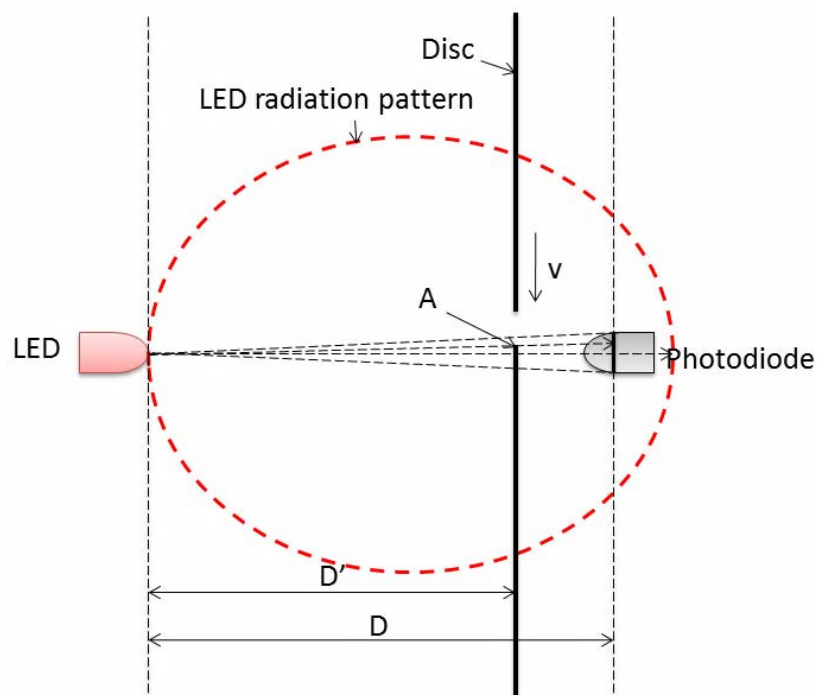
Fig. 4.1.2 A simplified geometry to model the received power of the experimental setup

The received optical power fluctuates due to the change in the effective photon collection area of the photodiode because it becomes shielded as a result of the motion of the disc hole in the cone of the LED radiation. Therefore, the received power can be expressed as the sum of photonic power collected by the unshielded area. From (3.1.1) and (3.1.2), the power becomes:

$$P_R = \frac{n+1}{2\pi D^2} P_E S_R \cos^{n+3}(\varphi) \tag{4.1.1}$$

in which S_R is the effective photons collection area as shown in Fig. 4.1.3, which is the intersection of the photon collection area and the projection of the hole over the LED radiation pattern.
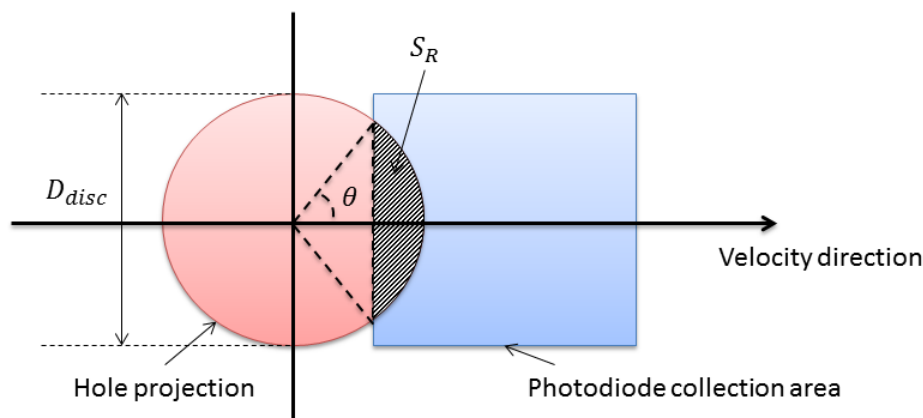
Fig. 4.1.3 Definition of the geometric parameter of the hole projection approaching the photodiode collection area

S_R depends on the velocity of the hole projection. The whole process can be divided into three stages. In the first stage, S_R increases as the projection moves towards the collection area and becomes better aligned with it, as described mathematically in (4.1.2). In the second stage S_R reaches the maximum value when the entire projection is in the photon collection area, as described by (4.1.3). In the third stage the projection moves away from the collection area, which causes the decrease in S_R, as shown in (4.1.4). To reduce the difference between the setups of the experiment and the model, the second stage should be minimized because S_R remains the same and does not produce power variation. The ideal scenario of the first stage (shown in Fig. 4.1.3) is when the diameter of the hole projection is equal to the width of the photon collection area, in which case the maximum power appears only at the moment of perfect alignment. In the real demonstration, this scenario can be obtained by adjusting the distance between the photodiode and the disc. If the widths of the projection and the photon collection area do not match, the second stage, when the signal power is constant, is extended. Minimizing the signal of the second stage gives the closest approximation to the ideal scenario.

Assuming the photodiode collection area is square and the hole is round, the effective area S_R for the three stages (i.e. moving towards, inside and then away from the projection of the radiation) is defined as:

$$S_R = \left(\frac{D_{disc}D}{2D'}\right)^2 \frac{\theta}{2} - \sin(\theta)\frac{D_{disc}D}{2D'}\left(\frac{vtD}{D'} + \sqrt{Ar}\right),$$

$$\theta = \cos^{-1}\left(-\frac{\sqrt{Ar} + \frac{vtD}{D'}}{\frac{D_{disc}D}{2D'}}\right),$$

$$\frac{vtD}{D'} \in \left(\frac{-\sqrt{Ar}}{2} - \frac{D_{disc}D}{2D'}, \frac{-\sqrt{Ar}}{2} + \frac{D_{discD}2D'}{2D'}\right)$$

(4.1.2)

$$S_R = \pi\left(\frac{D_{disc}D}{2D'}\right)^2,$$

$$\frac{vtD}{D'} \in \left(\frac{-\sqrt{Ar}}{2} + \frac{D_{disc}D}{2D'}, \frac{\sqrt{Ar}}{2} - \frac{D_{disc}D}{2D'}\right)$$

(4.1.3)

$$S_R = \left(\frac{D_{disc}D}{2D'}\right)^2 \left(\pi - \frac{\theta}{2}\right) + \sin(\theta)\frac{D_{disc}D}{2D'}\left(\frac{vtD}{D'} - \sqrt{Ar}\right),$$

$$\theta = \cos^{-1}\left(\frac{\sqrt{Ar} - \frac{vtD}{D'}}{\frac{D_{disc}D}{2D'}}\right),$$

(4.1.4)

$$\frac{vtD}{D'} \in \left(\frac{\sqrt{Ar}}{2} - \frac{D_{disc}D}{2D'}, \frac{\sqrt{Ar}}{2} + \frac{D_{disc}D}{2D'}\right)$$

in which D' can be found in Fig. 4.1.2 and θ and D_{disc} can be found in Fig. 4.1.3. The LED radiation angle φ is the angle measured from the radiation to the mid-point of S_R on the axis of the velocity direction, and is calculated as:

$$\cos(\varphi) = \frac{D}{\sqrt{\left(\frac{vt + \frac{\sqrt{Ar}}{2}}{2}\right)^2 + D^2}}$$

(4.1.5)

Since D is much larger than $\frac{vt + \frac{\sqrt{Ar}}{2}}{2}$, $\cos(\varphi)$ does not result in significant

contribution to the signal variance. Thus, when the photodiode is assumed aligned to the LED, $cos(\varphi)$ can be measured from the centre of the photon collection area and approximated to be 1.

The comparison between the calculated continuous power of the disc-hole experimental setup assumption and the theoretical model from section 3.1 is shown in Fig. 4.1.4. To achieve an equivalent length of communication window from the experimental setup to the theoretical model, the speed of the moving hole in (4.1.2)-(4.1.4) is reduced to only 1/200 of the speed of the LED in (3.1.6) while other parameters remain the same; both windows are shown in Fig. 4.1.4. The differences between the model and the experimental setup can be summarized as below:

- The maximum power in the experimental setup is $\pi/4$ of that in the model; the power difference comes from the area difference between the round hole and the square photodiode collection area.

- The shape of the time-varying power signal of the experimental setup is almost triangular, whilst that of the theoretical model is close to a sine wave.
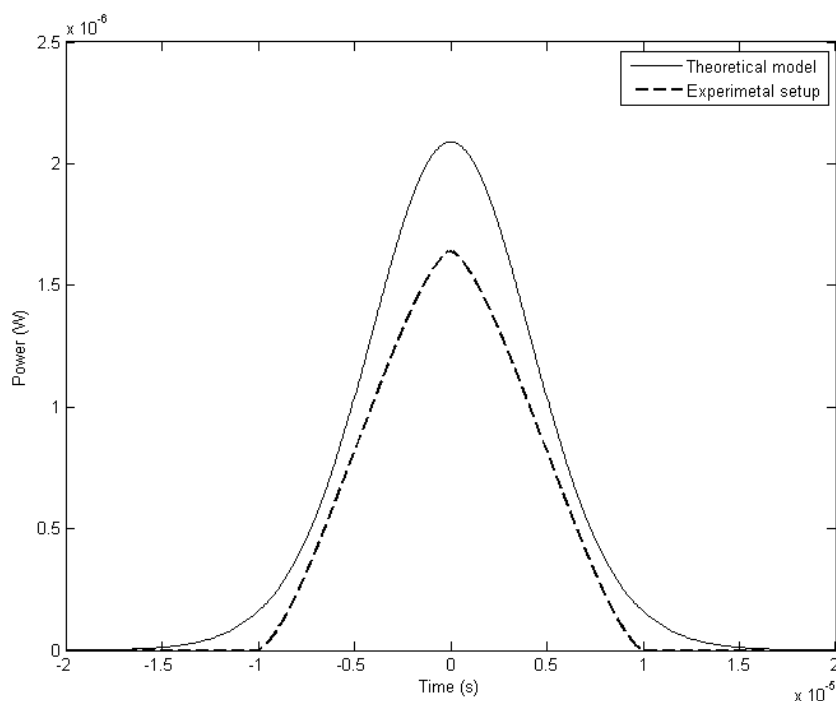
Fig. 4.1.4 Comparison between the experimental setup and the theoretical model time varying power signal (the hole speed is 1/200 of the theoretical LED speed)

The purpose of the experimental setup is to gain practical results on the system performance, such as received power under large signal fluctuations, and then compare with the theoretical results from system modelling, whilst taking into account the difference in geometry between the two systems.

The signal fluctuation SF, of the received power signals, P_R, in Fig. 4.1.4is calculated as the change in the power received over time:

$$SF = \frac{dP_R}{dt}$$ (4.1.6)

and the results in Fig. 4.1.5 are plotted. In the experimental setup SF is reduced and its peaks appear at different times compared to the theoretical model. Therefore, the experimental setup cannot represent the exact signal condition of the model and maintain the same distance between the LED and the photodiode.
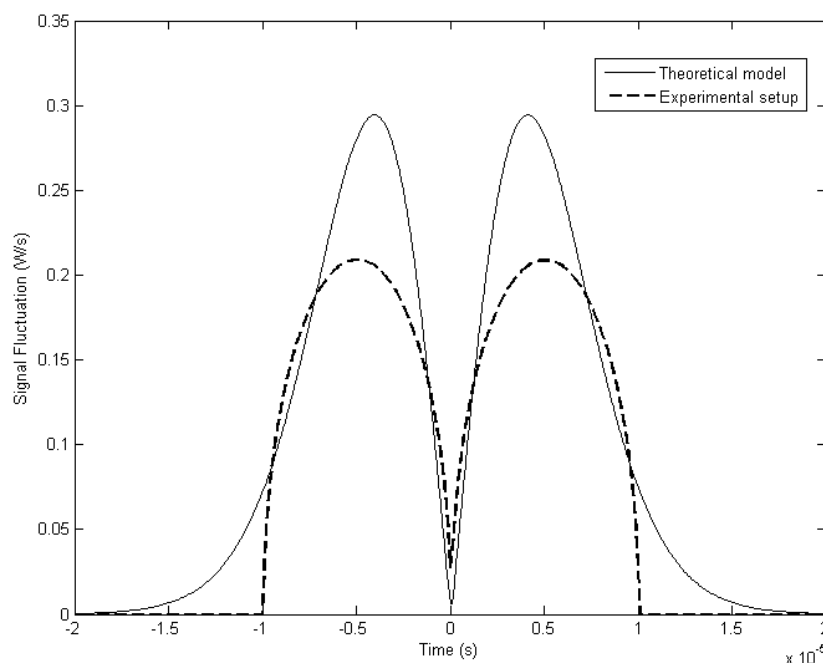
Fig. 4.1.5 Comparison between the fluctuations of the signal shown in Fig. 4.1.4 in the experimental and theoretical systems

However, despite the different times of the maximum SF appearances between

the experimental setup and the theoretical model, if the window of the experimental setup could be considered equivalent to that of the model when their maximum SFs are equal, the window of the experimental setup can be matched to that of the model. Changing the parameters in the experimental setup can generate an equal maximum SF as the model. Deriving (3.1.6) and (4.1.1) in first and second order, the maximum signal fluctuations of the model and the experiment are as follows.

$$\text{SF}_{max} = \frac{n+1}{2\pi} P_E A_r \frac{(n+3)D^{n+1}v^2 \left[\frac{D}{(n+4)^{\frac{1}{2}}}\right]^{\frac{1}{2}}}{\left[D^2 + \frac{v^2 D}{(n+4)^{\frac{1}{2}}}\right]^{\frac{n+5}{2}}} \tag{4.1.7}$$

$$\text{SF}_{max}^{EM} = \frac{n+1}{2\pi} P_E \frac{D_{disc}^2 v}{D'^2 \sqrt{\left(\frac{D_{disc}D}{D'}\right)^2 - \left(\frac{D_{disc}D}{D'} - \sqrt{Ar}\right)^2}} \tag{4.1.8}$$

in which SF_{max} is the maximum signal fluctuation of the model, and SF_{max}^{EM} is that of the experiment. (Please refer to Fig. 4.1.2 on page 81 and Fig. 4.1.3 on page 82 for the symbol definitions)

Defining SF_{max} with the angular factor of the Lambertian pattern gives (4.1.7) another, simpler, form:

$$\text{SF}_{max} = -\frac{n+1}{2\pi D^2} P_E A_r \cos^{n+2}(\varphi_{SF}) \sin^{n+3}(\varphi_{SF}) \tag{4.1.9}$$

φ_{SF} is defined as:

$$\varphi_{SF} = \cos^{-1}\left(\frac{D}{\sqrt{D^2 + \frac{Dv^2}{(n+4)^{\frac{1}{2}}}}}\right) \tag{4.1.10}$$

Minimizing the second stage described by (4.1.3) yields $\frac{D_{disc}D}{D\prime} = \sqrt{Ar}$, which means the diameter of the hole projection is equal to the height and width of the photon collection area. Thus, (4.1.8) can be simplified as:

$$SF_{max}^{EM} = \frac{n+1}{2\pi} P_E \frac{D_{disc}v}{D\prime D} \tag{4.1.11}$$

If the difference between the maximum signal fluctuations is considered to be the result of distance variation, a distance factor F_D could be introduced, which is the ratio of the distance between the LED and the photodiode of the model over that of the experiment when $SF_{max}^{EM} = SF_{max}$:

$$F_D = \frac{D}{D_{EM}} \tag{4.1.12}$$

The results of F_D vs. D_{EM} from 0.1 m to 1 m in Fig. 4.1.6 shows that, when D_{EM} is between 0.1 and 0.2 m, the equivalent distance of the model D is longer than the experimental distance, but from 0.3 to 1 m, the equivalent distance of the model is shorter.

In summary, the setup in the experimental environment does not bring an equal or similar communication window as the model with the same geometrical parameters; differences appear in the speed, maximum power and maximum signal fluctuation. However, through a series of calculations, it is possible to estimate the corresponding window in the model from the experimental setup, or simulate a certain maximum amount of signal fluctuation of a window by adjusting the geometric parameters.
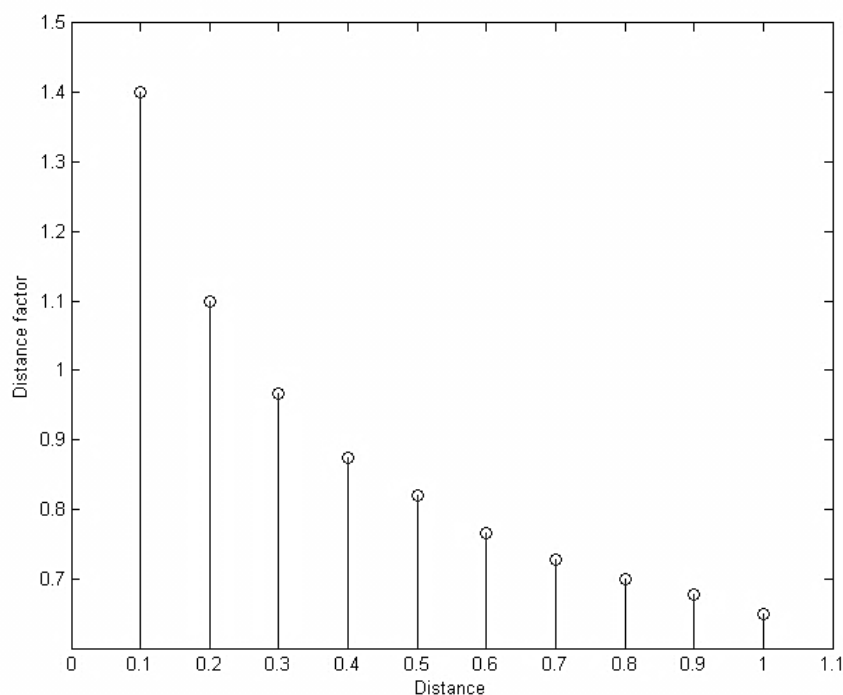
Fig. 4.1.6 Distance factor versus simulation distance from 0.1 m to 1 m

4.2 IR Transceiver Circuit

The functions of the IR transceiver, which provides the optical interface to the communication controller that uses digital modulation, include photoelectric signal conversion and signal processing. To investigate the actual implementations of the AGC amplifier and TIA in the fast fading channel, a transceiver circuit was developed to transfer digital signals wirelessly between two ends on IR channel, the components of which are shown in Fig. 4.2.1.

The circuit includes a transmitter and a receiver, connected to the signal input and output of the communication controller individually. Since the circuit is designed for demonstration purposes, some extra control functions are added. The amplifier in the transmitter is one example, by which the LED emitted power becomes adjustable. The design of the receiver is mainly based on the models described in section 3.1 and 3.2. Because the gain of the TIA comes from the transresistance (please see section 3.2.3.) and its output signal amplitudes changes for each feedback resistor, a gain-adjustable

pre-amplifier is added between the TIA and the AGC amplifier.
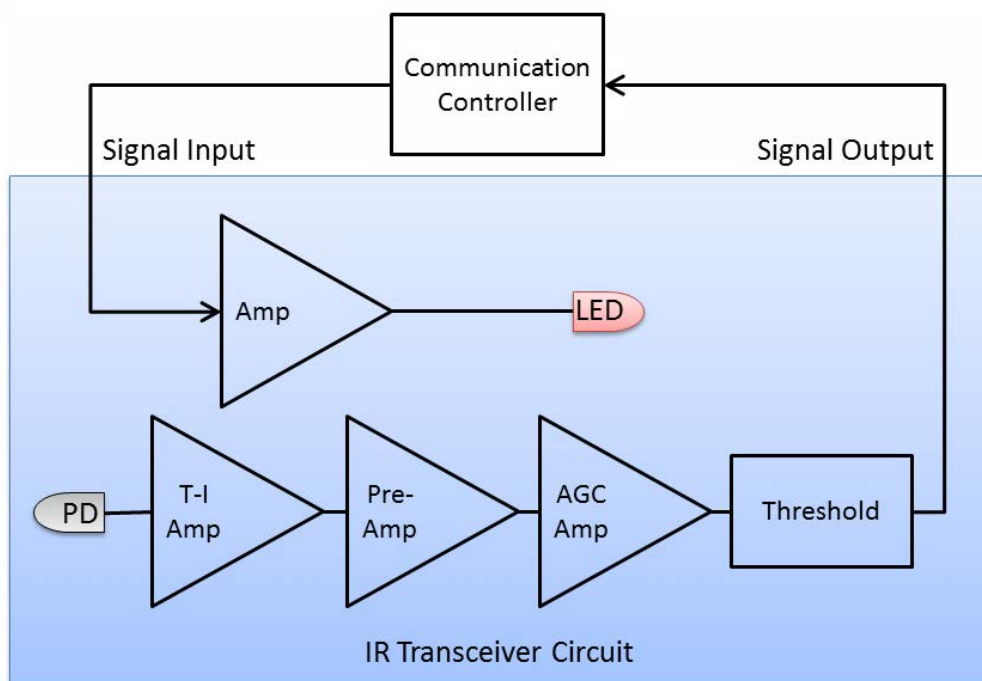
Fig. 4.2.1 The components of IR transceiver circuit. (PD = photodiode, T-I = transimpedance and AGC = automatic gain control)

4.2.1 The Transmitter and the Receiver

Fig. 4.2.2 is the IR transmitter that is modified from [167]. Op-Amp U1 and enhanced MOS-FET Q1 are the key components to modify the input signal to optical signals with different power. By adjusting R3, the gain of U1 is modified; and the voltage of Q1 controls the current flowing into the IR LED D1. U1 supplies the voltage to Q1 as indicated; therefore R3 controls the emitted power of the IR LED from a certain input voltage level.

The TIA and the pre-amplifier are shown in Fig. 4.2.3. The circuit includes two levels of Op-Amp, in which U3 converts the photodiode signal current from D2 into voltage signals. U4 amplifies the signals at different amplitude, and therefore the influence of different feedback resistors can be minimized to some extent. The rest of the signal difference will be reduced further in the following AGC amplifier. In an

actual PCB board, pins of R9, R10, R11, R17 and C4 are mounted with sockets, as a result the configuration can be easily changed for testing different feedback resistors. The gain of the receiver section shown in Fig. 4.2.3 can be calculated as:

$$g_{r1} \approx R9\left(1 + \frac{R11}{R10}\right) \tag{4.2.1}$$
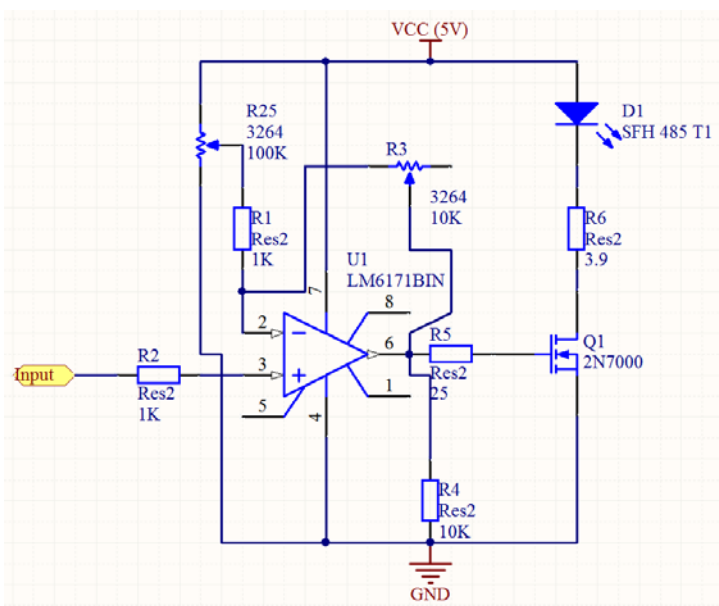
Fig. 4.2.2 The schematic of IR transmitter circuit
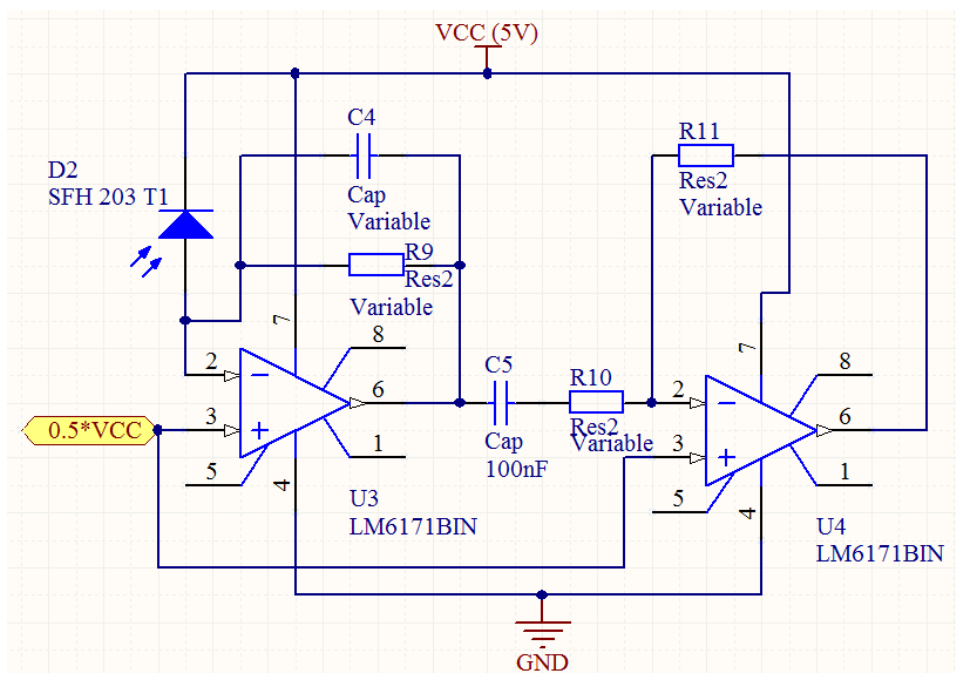
Fig. 4.2.3 The schematic of the TIA and pre-amplifier in the receiver

The rest of the receiver, shown in Fig. 4.2.4, contains the AGC amplifier and threshold that modified from [168].
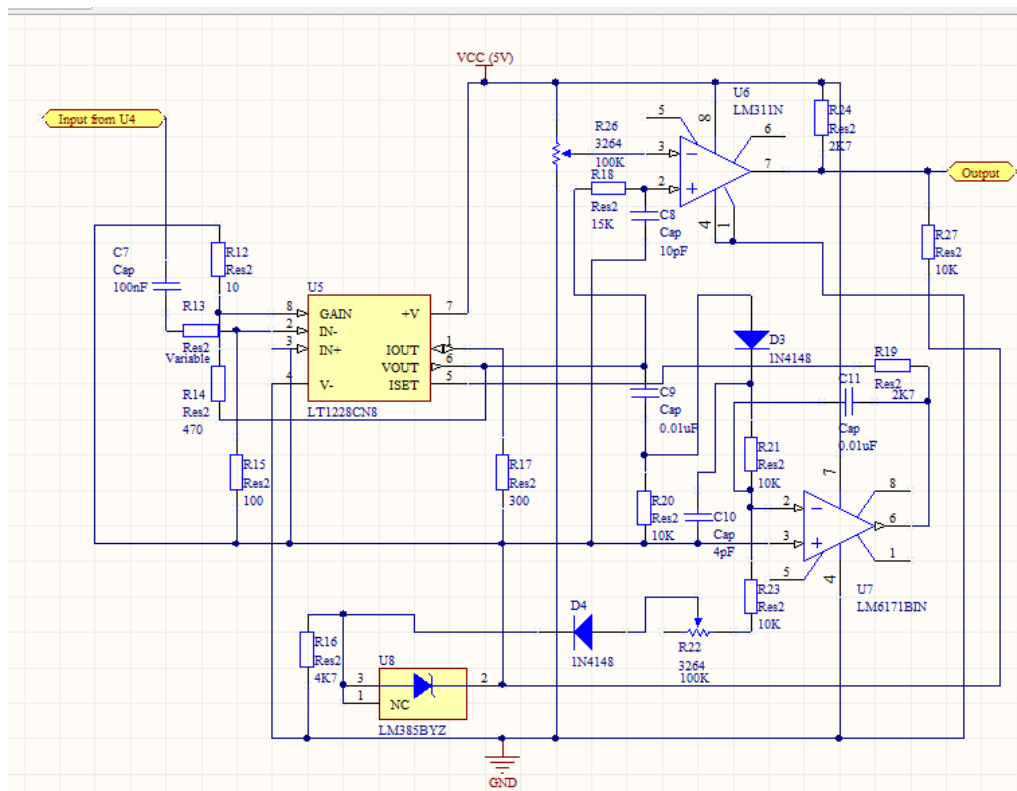
Fig. 4.2.4 The schematic of the AGC amplifier and threshold in the receiver

According to the component specification of U5 [168], the diverse signal range resulting from different feedback resistors from the transimpedance can be further reduced from the partial input at pin 2, by mounting corresponding resistors on R13 and R15. The correspondance of the model in section 3.2.2 and the circuit can be found as follows:

- U5 is the VGA controlled by the current supplied on pin 5, for which the gain of inverting input pin 2 is:

$$g_{VGA} = 10I_{pin5} \tag{4.2.2}$$

- D3 is the detector.
- U7 forms the core of the integrator.

- The reference is set by adjusting R22 to change the current from 1.2V zener diode U8.

Again, from the specification and setup on Fig. 4.2.4, the gain of the AGC amplifier can be calculated as follows [168]:

$$g_{r2} = \frac{R15}{R13 + R15} \cdot 10 \cdot I_{pin5} \cdot R17 \left(1 + \frac{R14}{R12}\right) \tag{4.2.3}$$

where I_{pin5} is defined as:

$$I_{pin5} = \frac{V_{U7} - 2\left(E_g - \frac{akT_n}{q}\right)}{R19} \tag{4.2.4}$$

in which $E_g = 1.25\,V$ and $a = 19.4$ at $27\ ℃$, $E_g - \frac{akT_n}{q}$ represents one diode forward voltage drop. The voltage on pin 5 is equal to that on pin 4 dropped by two diodes (assuming that $E_g - \frac{akT_n}{q}$ and the diode forward voltage is 0.6 V). V_{U7} is the output of the integrator U7, which is defined as:

$$V_{U7} = \frac{\dfrac{1.2 - 0.6}{(R22 + R23)C11} - \dfrac{\left(\dfrac{V_{out(p-p)}}{2} - 0.6\right)H_e(s)}{R21 \cdot C11}}{s}, \tag{4.2.5}$$

$$(V_{out(p-p)} > 1.2\,V)$$

in which $V_{out(p-p)}$ is the peak to peak AGC amplifier output and $H_e(s)$ is the transfer function of the envelope detector. Therefore,

$$g_{r2} = \frac{R15 \cdot R17}{R13 + R15}\left(1 + \frac{R14}{R12}\right) \cdot 10 \tag{4.2.6}$$

$$\cdot \left[\frac{\dfrac{0.6}{(R22 + R23)C11} - \dfrac{\left(V_{out(p-p)}/2 - 0.6\right)H_e(s)}{R21 \cdot C11}}{s \cdot R19} - \frac{1.2}{R19} \right],$$

$$(V_{out(p-p)} > 1.2\ V)$$

From the model in section 3.2.2, the loop gain of the AGC amplifier is:

$$g_{l-AGC} = R17 \left(1 + \frac{R14}{R12}\right) \frac{5 \cdot R15 \cdot H_e(s)}{(R13 + R15)R19 \cdot R21 \cdot C11} \qquad (4.2.7)$$

Taking all the receiver amplifiers into account, the total loop gain between the photodiode current and the output of AGC amplifier is:

$$g_l = \frac{5 \cdot R9 \cdot R15 \cdot R17 \cdot H_e(s)}{(R13 + R15)R19 \cdot R21 \cdot C11} \left(1 + \frac{R14}{R12}\right) \left(1 + \frac{R11}{R10}\right) \qquad (4.2.8)$$

Because the VGA of U5 is controlled by a current that ranges from 1 µA to 1 mA [168], it means that the VGA offers 30 dB dynamic range to the signal fluctuation. According to (3.2.16), the theoretical maximum transimpedance feedback resistor in the channel in chapter 3 with full gain control can be more than 70 kΩ at 1 MHz. Followed by the AGC amplifier is a threshold based on U6, in which the threshold voltage is a full range of the power supply set by R26. At the output terminal, the amplitudes of the signals are converted to that of the power supply VCC.

4.2.2 AGC Gain Selection and Limitation of the Envelope Detector

To reduce the signal fluctuation requires a wide dynamic range from the AGC amplifier. In practice, this dynamic range is limited by the envelope detector more than the VGA. In the schematic shown in Fig. 4.2.4, the forward voltage of envelope detector diode D3 produces the threshold of 0.6 V in the output feedback loop, which means the signal with lowest power level and satisfying the required error rate needs

to be amplified to a value of $V_{out(p-p)}$ higher than 1.2 V. Also, the useable signal should also satisfy $\left[\frac{0.6}{(R22+R23)C11} - \frac{(V_{out(p-p)}/2-0.6)H_e(s)}{R21 \cdot C11} \right] < 0$, matching the signal of the communication session to the lower limit of the AGC amplifier gain controlled range. Considering the gain from the photocurrent I_P to the output of the AGC amplifier V_{out}:

$$\frac{V_{out}}{I_P} = g_{r1} g_{r2} \tag{4.2.9}$$

and g_{r2} is still at the maximum value when $\left[\frac{0.6}{(R22+R23)C11} - \frac{(V_{out(p-p)}/2-0.6)H_e(s)}{R21 \cdot C11} \right] = 0$, the threshold level of I_P is selected by:

$$I_{P(p-p)} > \left[1.2 + \frac{1.2 \cdot R21 \cdot H_e^{-1}(s)}{(R22 + R23)} \right] g_{r1}^{-1} g_{r2(max)}^{-1} \tag{4.2.10}$$

When '$1.2 + \frac{1.2 \cdot R21 \cdot H_e^{-1}(s)}{(R22+R23)}$' is set, the threshold of $I_{P(p-p)}$ is related to $g_{r1} g_{r2(max)}$, which can be modified. The selection of the undetermined components from the circuit is from the following rules:

- The threshold level of $I_{P(p-p)}$ from g_{r1} and $g_{r2(max)}$ needs to satisfy the required error rate.
- To preserve the dynamic range of the AGC amplifier, I_{pin5} needs to be close to the top of the allowed range for U5, which is 1 mA, when I_P reaches the threshold level. At this moment, V_{U7} is still at the maximum that depends on the maximum output of U7 under VCC, which determines R19 using (4.2.4).
- g_l in (4.2.8) needs to be large enough, which is discussed in section 3.2.2.

The forward voltage drop of the diode in the envelope detector limits the selection of $g_{r1} g_{r2(max)}$. For the channels with low noise level for which the

threshold of $I_{P(p-p)}$ can be set at a low level, amplifying $I_{P(p-p)}$ from $g_{r1}g_{r2(max)}$ to higher than the envelope detector's forward voltage drop is not power efficient. The forward voltage of the diode can be reduced to some extent by replacing the D3 with a Schottky diode with lower forward voltage. To extend the dynamic range of the envelope detector, the forward voltage needs to be bypassed by biasing the detector input signal.

The diode detector can be replaced by an FET biased envelope detector discussed in [169], from which, with added R4 and the biasing resistors, the design becomes the one shown in Fig. 4.2.5. In this application, the envelope detector is used on the signal feedback and the output will be integrated; the noise generated by the detector components is not considered as influencing the performance in the range of interest for the application. In this case, the threshold can achieve a small value from the bias voltage and the variance of the forward voltage of the FET from the temperature difference may affect the threshold stability. The temperature effect can be compensated from the bias by introducing a series thermistor (R2) in the biasing resistors. The simulation result of the envelope detector in Fig. 4.2.6 shows that the sensitivity can be 22 mV on the 0.1 V AM signal, the carrier frequency is 1 MHz and the signal frequency is 500 Hz (2 μs period), which can be assumed as the signal frequency is 1 MHz, and the frequency of the communication window is 500 Hz in this application.
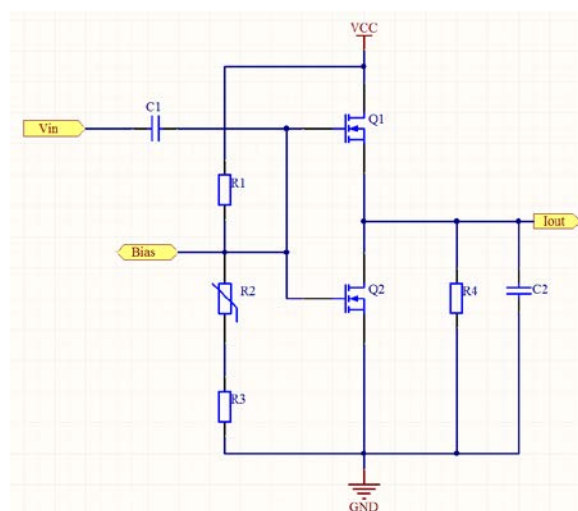
Fig. 4.2.5 The FET envelope detector
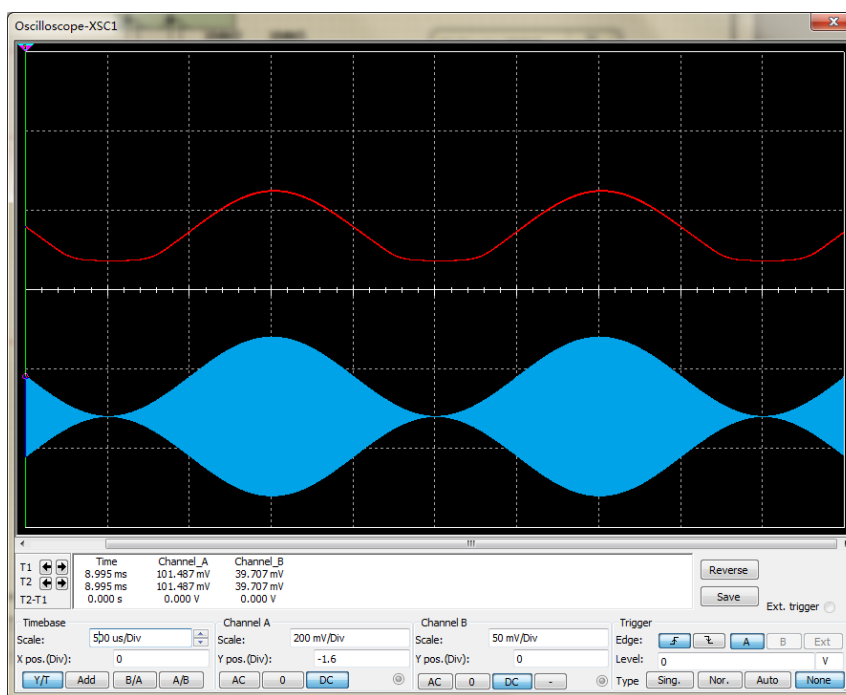
Fig. 4.2.6 Simulation result of the FET envelope detector. Red line: output of the detector; Blue line: AM signal input of the detector.

4.3   Signal Detection and Modulation

4.3.1   Communication Session Boundary Detection and Real-time Condition Monitoring of the Fast Fading Channel

The theoretical, ideal and actual thresholds in the AGC amplified communication window are shown in Fig. 4.3.1. In the theoretical model, the threshold provides a power level to achieve the dedicated error rate on '0'. And the required power level on '1' for the dedicated error rate is approximately double of the theoretical threshold. The gain of the signal in the communication session from the AGC amplifier output is controlled to maintain a stable power level. In the ideal condition, the threshold can be set at the stable power level, therefore only those signals with sufficient power can go through, achieving the dedicate error rate. However, considering the actual case that the signal shape is not square pulse and the signal variation cannot be fully eliminated, setting the actual threshold equal to the ideal one is in high risk of blocking the useful

signals. Therefore, the actual threshold needs to be at a level below the ideal one to avoid the influence from the remaining signal variance. The actual threshold also expands the communication period longer than the actual communication session. In the expanded margin periods, large signal variation still exists and signal power inside does not reach the required power for the dedicated error rate. If the time of communication session varies with the speed of the rotor, to predict the actual boundaries of the communication session is difficult. Thus, the channel condition is necessarily monitored in real time, tracing the boundaries of the communication session.
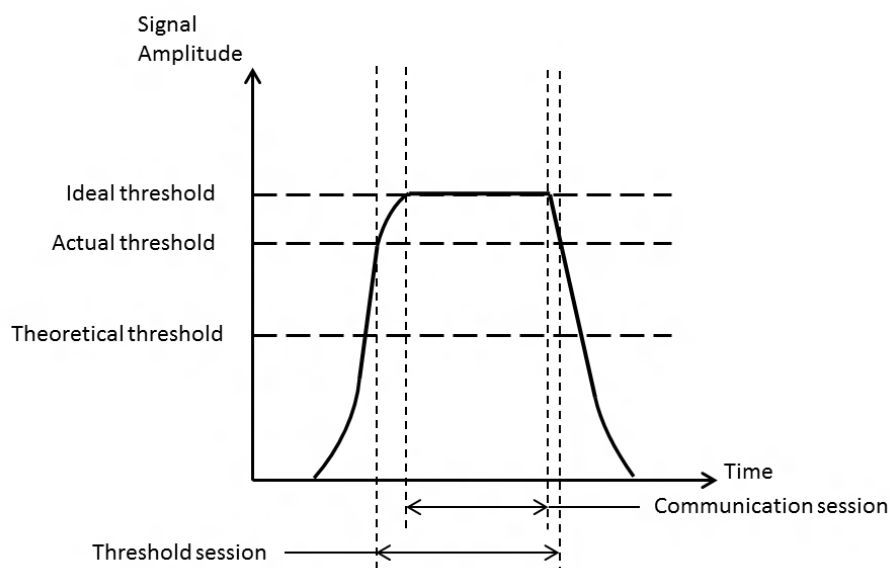
Fig. 4.3.1 The differences between a theoretical, an ideal and an actual threshold in AGC amplified signal.

In the margin periods between the threshold session and the communication session, the large power variation still causes significant difference in the pulse width of the signal. The pulses with width difference only last for a short period and the exact time depends on the actual threshold. Performing communication in these periods can be unreliable, since the power of the signal does not satisfy the required power level of the error rate, and the width difference may cause unexpected errors. But on the positive aspect, the boundaries of the communication session can be known from detecting the pulse width differences.

Limiting the conversation of the devices in the communication session with unexpected ending needs a signal condition monitoring in each of the symbol. As among OOK, MPPM, DPIM and OPPM, only OPPM features with certain and continuous duty cycle in each symbol, therefore it enables a channel condition monitoring according to signal pulse width in each symbol during signal detection. A dual detection identification (DDI) is developed as shown in Fig. 4.3.2, and the actual implementation will be specified in chapter 4.4.3. The incoming pulse is detected twice, in which one captures the pulse on the rising edge and the other on the falling one. The two results are then compared and the current signal status is considered in the communication session if the error between those results is smaller than a certain threshold value. The DDI therefore provides real time channel condition for the communication controller on OPPM, making decisions of entering and exiting the conversation on the boundaries of the communication session. The DDI works as a software latch to limit the communication in the communication session.

Error = abs(D1 - D2)
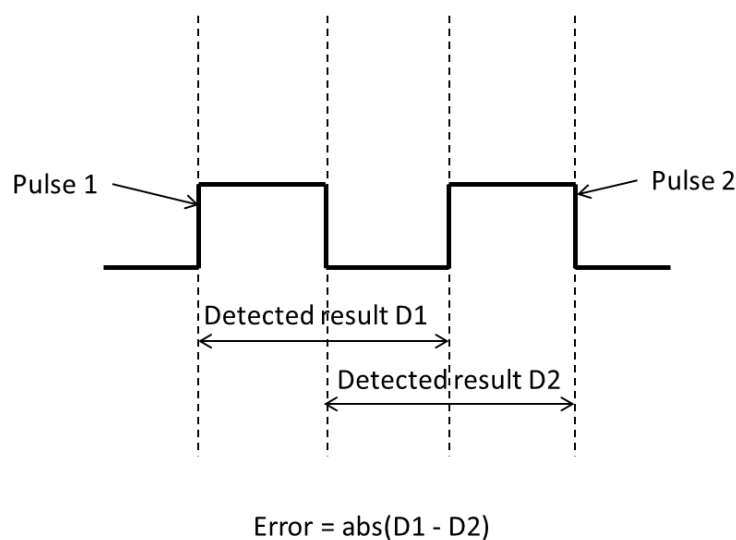
Fig. 4.3.2 The dual detection identification.

The effectiveness of DDI is demonstrated by the system generating the signal pattern, which is shown in Fig. 4.3.3. One IR transceiver, including the signal processing circuit and the communication controller, generates identical IR signal pulses of 50 % duty cycle at 200 kHz, which can be received by the other IR transceiver

through the hole on the rotating disc. The signal processing circuit output is recorded by the oscilloscope that is triggered by the communication controller. In this configuration, the communication controller can be programmed to decide whether to display the received pulses by managing the trigger of the oscilloscope.
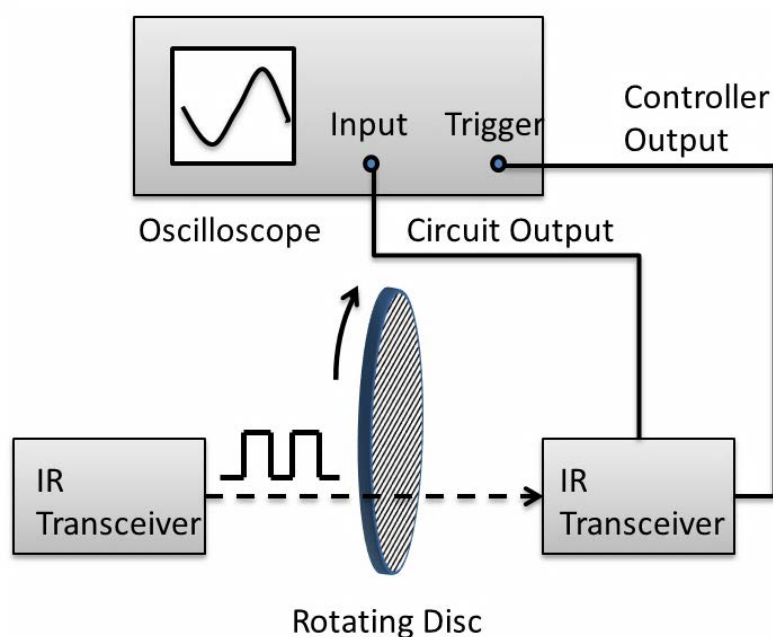
Fig. 4.3.3 The system that generates eye diagrams to demonstrate the DDI function.

Fig. 4.3.4 and Fig. 4.3.5 show two results of signal pattern persisting plot of 10 seconds from the system in Fig. 4.3.3, in which the signal pattern of trigger signal shows on oscilloscope channel 1 and that of the received signals on channel 2, while in Fig. 4.3.5 the communication controller triggers on each pulse it received, but on Fig. 4.3.4 the controller triggers based on DDI, in which the safety value of width difference is 1/8 of the original pulse width of the signal from the transmitter. To avoid extra variation caused by the accumulated error of a long synchronization, on both triggers the communication controller recalibrates on the next pulse after triggering 8 pulses, which assumes a frame of 8 symbols is received. If the received signal pulse is considered the output of the load resistor front end in Fig. 3.1.4, the jitter caused from the width difference of the signal is more significant on the rising edge than on the falling. Therefore, to produce a stable persisting plot, the trigger for signal without

DDI is based on the falling edge. The process of DDI delays the trigger to about 1/2 of the pulse duration, and as a result the trigger of the signal with DDI begins at the 1/2 of the signal pulse.

The persisting plot when DDI is applied, shown in Fig. 4.3.4, indicates much less width variance compared to that of Fig. 4.3.5. Nevertheless, the signal pattern based on DDI still shows considerable jitter on the rising edges, which is not avoidable from the method since at each end of the communication session, the trigger stops after pulses with inappropriate widths are received and identified, therefore the trigger turning off is delayed and the jitter is recorded; since the trigger is more referenced to the falling edge, as a result the rising edges are more affected. But in real communication, the signals with inappropriate widths will be ignored by the communication controller; the error rate will not be affected.

Therefore, the communication does not start and end on the boundaries of the threshold session. The communication beginning and ending is limited inside the communication session based on two effects:

1. The AGC amplifier creates a respectively stable power level of the communication session.

2. The communication controller detects the boundaries of the stable power level using DDI.
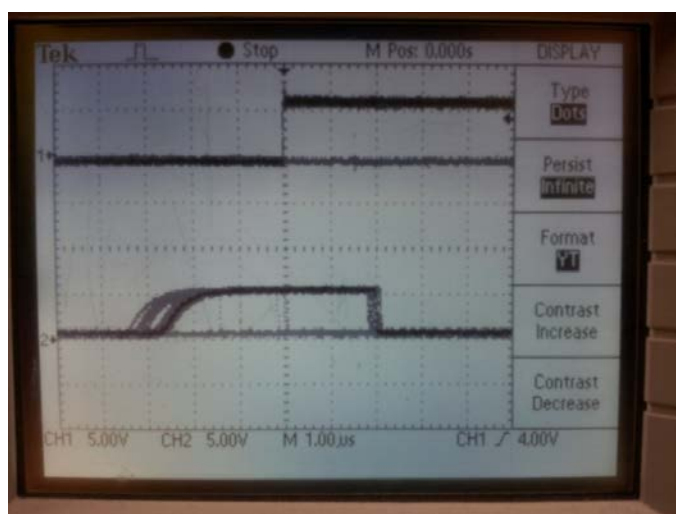
Fig. 4.3.4 Persist plot of system with DDI in Fig. 4.3.3 in 10 s at 200 kHz.
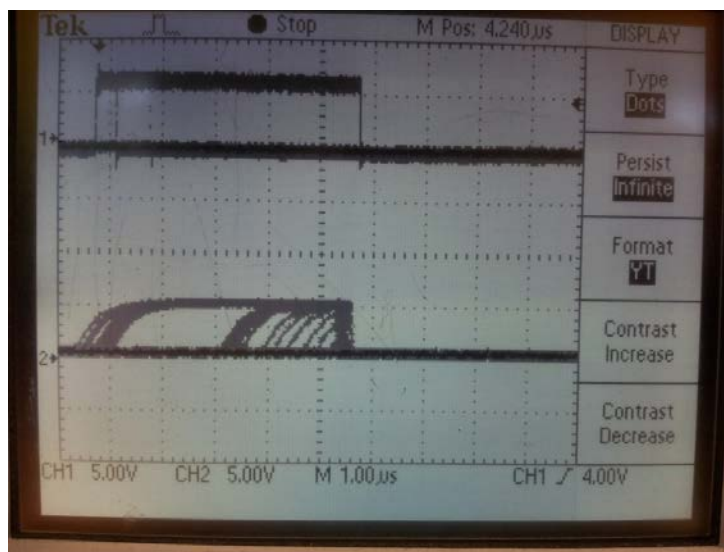
Fig. 4.3.5 Persist plot of system without DDI in Fig. 4.3.3 in 10 s at 200 kHz.

4.3.2   OPPM Power Efficiency

Compared to OOK, the advantage of OPPM is the higher information rate that improves the bit capacity of a communication window with no cost from bandwidth in this case [108, 170]. However, the difference between the symbols of OPPM is smaller than that of OOK, as a result, the minimum power required for a certain bit rate is higher on OPPM than OOK. As OOK is the modulation of the model described in chapter 3, OOK is used as a benchmark to evaluate the power efficiency of OPPM for our application.

According to [106] and [171], the BER of a modulation is dominated by the two nearest signals:

$$BER = Q\left(\frac{d_{min}}{2\sqrt{N}}\right) \tag{4.3.1}$$

in which N is the power spectrum of the Gaussian white noise, and d_{min} is the minimum Euclidean distance between two symbols, defined as:

$$d_{min}^2 = \min_{i \neq j} \int \left[x_i(t) - x_j(t)\right]^2 dt \tag{4.3.2}$$

Assuming no inter-symbol interference (ISI) is present in the channel, the Euclidean distance of OOK and uncoded OPPM with average power P at bit rate R_b are:

$$d_{OOK} = \frac{2P}{\sqrt{R_b}} \qquad (4.3.3)$$

$$d_{OPPM} = \frac{P}{m} \sqrt{\frac{2\,n\log_2 L}{R_b}} \qquad (4.3.4)$$

In (4.3.4), the symbol is divided into n chips, the pulse width is m chips and L is the total number of symbols of OPPM. An OPPM configuration with a duty cycle of 0.5 and leaving one symbol unused as guarding space is considered, therefore:

$$n = 2m \qquad (4.3.5)$$

$$L = n - m = m \qquad (4.3.6)$$

Different to the power analysis described in section 2.2.4, here the bit rate ratio is introduced, which is defined as the bit rate of a modulation over that of OOK when using equal average power to reduce the error rate to the same level. The reason for using the bit rate ratio instead of the average power, to evaluate the power performance of the modulation is as follows. On the periodic fast fading channel and the related threshold strategy, described in section 3.1.3, an adjustment on either power or error rate will result in different lengths of the communication sessions in the theoretical model (based on the Saddlepoint approximation), which has a different impact on the bit capacity than the modulation does.

From the OPPM described in (4.3.5) and (4.3.6), the corresponding bit rate ratio becomes:

$$R_{OPPM/OOK} = \frac{\log_2 m}{m} \tag{4.3.7}$$

The concept of power is different between the theoretical model and the power in (4.3.3) and (4.3.4). The bit power of the theoretical model is the power of symbol '1', while the power in (4.3.3) and (4.3.4) represents the average power of symbol '1' and '0'. Statistically, in OOK $P = \frac{P_R}{2}$ by assuming equal numbers of symbols '1' and '0' are received. Moreover, $P = \frac{P_R}{2}$ is also valid in the $\binom{2m}{m}$ OPPM, as, in each symbol, half of the chips are occupied. Therefore, the communication sessions of OOK and the $\binom{2m}{m}$ OPPM are of the same duration. Since the bit capacity is proportional to the bit rate of the same duration, $R_{OPPM/OOK}$ is also the ratio of the bit capacity.

According to (4.3.7), the bit rate of $\binom{2m}{m}$ OPPM is worse than that of OOK in all selection of m since $\log_2 m < m$ and, with m increased, $\frac{\log_2 m}{m}$ is approaching zero as shown in Fig. 4.3.6. In the periodic fast fading channel, the bit capacity drops if more symbols are generated from one symbol duration for $\binom{2m}{m}$ OPPM compared to OOK, the optimal options for m are $\binom{4}{2}$ for which the bit capacity is half of that of OOK.
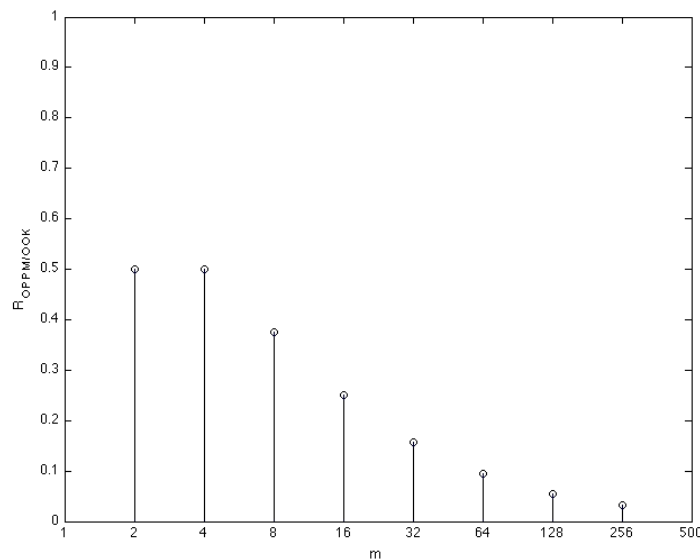
Fig. 4.3.6 The information capacity ratio of OPPM over OOK in different preferences of symbol capacities.

From another point of view, the bit rate of OPPM can be increased if the minimum power level is higher. But higher power level in the periodic fast fading channel also means shorter communication session and error rate reduction. Here it is assumed the threshold strategy remains as that for OOK from the theoretical model and the power requirement for OPPM concerns only (4.3.1) and (4.3.2) with no effect on the error rate. The ratio of the power of OPPM and OOK can then be expressed by (2.2.31) to achieve the same bit rate. In this case, gaining the same bit rate from OPPM only results in loss in the duration of the communication session, from which the bit capacity of OPPM is also decreased. Therefore, from the reduction of bit capacity, the cost of using OPPM in the channel can be evaluated. For $\binom{2m}{m}$ OPPM where $m = 2$, $\frac{P_{OPPM}}{P_{OOK}} = \sqrt{2}$. The results are shown in Fig. 4.3.7 for channels of the front end in Fig. 3.1.4 with 50 Ω load resistor and TIA in Fig. 3.2.6 with 50k Ω feedback resistor.
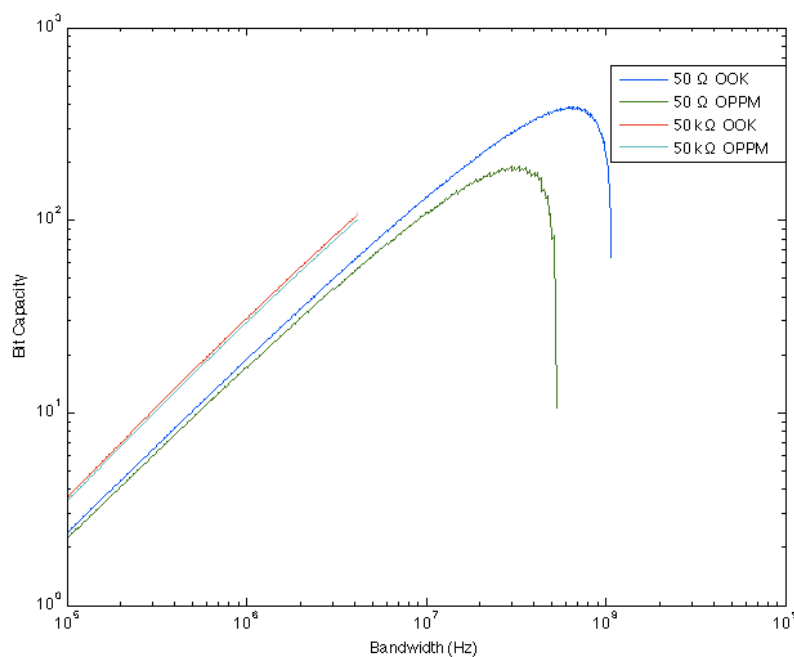
Fig. 4.3.7 The bit capacities for the front end in Fig. 3.1.4 with 50 Ω load resistor and TIA in Fig. 3.2.6 with 50k Ω feedback resistor   using OOK and $\binom{2m}{m}$ OPPM that $m = 2$.

For $m = 2$, none of the channels show significant performance reduction on OPPM. The influence is more significant on 50 Ω since a channel with lower resistor

requires a higher power level and the power raises more in the same proportion $\frac{P_{OPPM}}{P_{OOK}}$. Moreover, the extra power demand of OPPM affects the 50 Ω at higher bandwidth, at which the channel is cut off occurs at a lower frequency for OPPM than that for OOK.

Therefore, applying OPPM as modulation to the periodic fast fading channel does not bring significant bit capacity reduction on channels with high resistors or low resistors at low bandwidth. But in the situation where a high bandwidth with low resistor is necessary, OOK is much more preferable.

4.4 Communication with OPPM Encoding and Decoding with Software Latch on MSP430 Microcontroller

There are two models of MSP430 chipset used in this application, the information of which are shown in Table 4 [172, 173]:

Model	Max Clock Frequency.	Typical Current at 1 MHz on 2.2 V Power Supply
F2418	16 MHz	365 uA
F449	8 MHz	280 uA

Table 4 The MSP430 microcontrollers.

The MSP430 setup in Fig. 4.4.1 shows the connection between the microcontroller and the IR transceiver circuit. The OPPM signal generation and detection are based on the program managed operations of the internal timer A (TA) and B (TB). Therefore, the input and output of the IR transceiver circuit are connected to the I/O of the timer capture/compare registers (CCRs). Those timers are configured to operate on the same frequency of the master clock (16 MHz on F2418 and 8 MHz on F449).

There are three modes of the MSP430 timer [174, 175]: continue, up and up-down. The up mode is used in this application, in which the timer counts to the pre-defined value stored in CCR0 then reset to 0. In each reset a bit is set to '1' in the

control register (CTL). What is more, the I/Os of the timer can be configured from the related capture/compare control register (CCTL) by the program as an input or output. In capturing an input signal, the counter value of rising or falling signal edge is recorded in the CCR, and a capture bit is set in the CCTL.
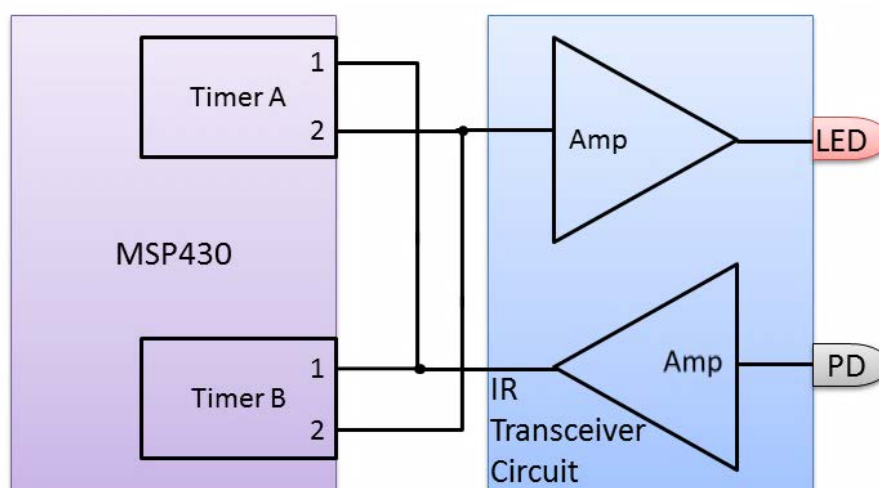
Fig. 4.4.1 The connections between the MSP430 microcontroller and the IR transceiver circuit

4.4.1 Baseband Protocol

The main function of the communication is sensor data transfer from the DT on the rotor to the DR on the stator or the outside, in which the power of the DT is limited. In this case, the protocol needs to be designed to minimize the optical signals from the DT, since emitting optical signal consumes extra power that increases the overall power consumption. Given such a purpose, a specific baseband protocol is proposed, including link control, frame definition and bit stream process.

Since the DR is assumed with no power limitation in this application, it hosts and controls the communication, by taking on the functions of searching, detecting and resetting the communication. The DT reacts to the instructions from the DR and only owns authorization on deciding the beginning and stopping the transmission. The communication is half-duplex, avoiding the interference from unexpected optical signal reflections in an actual environment.

The ordinary workflows of the two devices in a communication window are shown in Fig. 4.4.2, which illustrates the operations from the beginning to the end of the conversation between the DT and the DR.
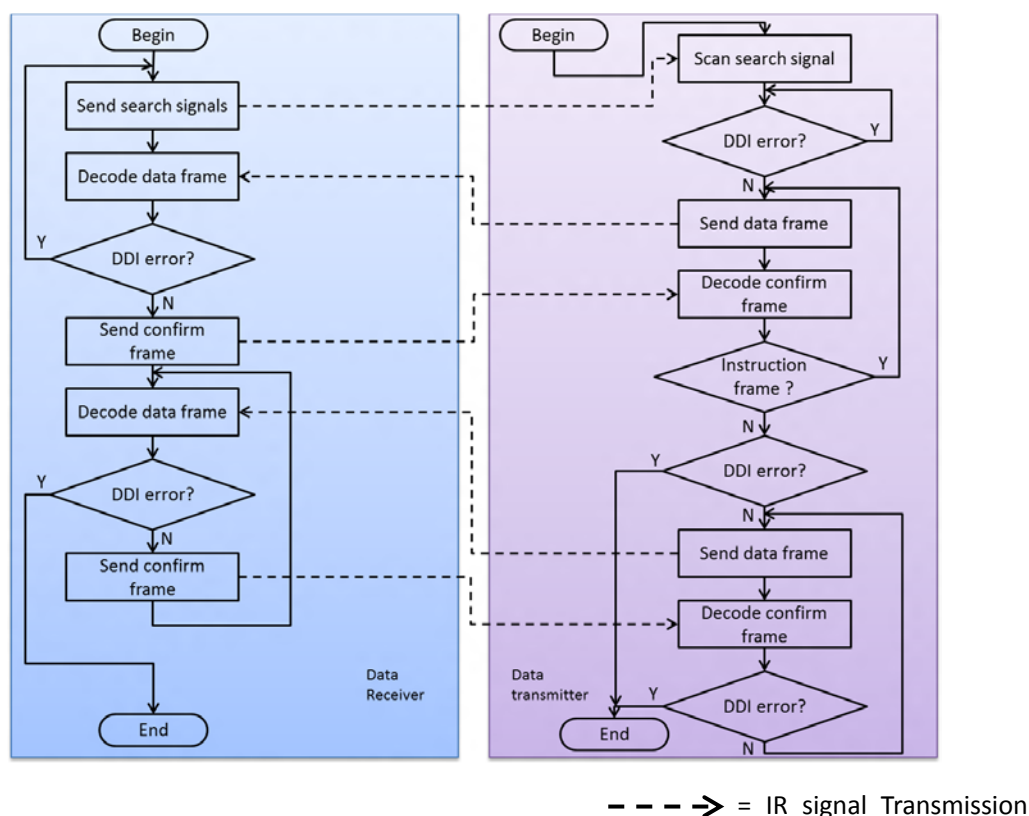
Fig. 4.4.2 Normal Workflow of DT and DR.

Before the communication window, DR sends searching signals continuously. The searching signals are 8 symbols of identical on-off pulses with 50% duty cycle, leaving an interval of 3 symbols for the DT reaction. As soon as the DT receives the searching signals, the DDI is performed on the searching signals and latches the transmitter into communication mode, sending the first data frame in the interval between the searching signals. The DR then processes the first data frame and latches into the communication if the DDI does not return any error, the confirmation frame is then sent to the DT, otherwise the DR waits 3 symbols then resends the searching signal. The DT repeats the above process until the confirmation frame is received. Then the two devices repeat the send-confirm procedure until one of them detects the end of the communication session from DDI. Any of the devices can terminate their conversation based on the

detection of DDI. Once the communication boundary is detected, either device stops sending signals and exits the conversation, while the other waits for the maximum turnaround time and exits because of not receiving any valid signal. The maximum turnaround time for the DR, T_{DR}, is a 2-symbol duration. Considering the clock frequency of the microcontroller on the DT is half of that on the DR, T_{DT} = 4-symbol duration is the maximum turnaround time for the DT, which equals to $2T_{DR}$.

Since the communication is performed on an intermittent channel, there are several factors that may cause failure of the communication. The situation that both devices failed to detect the termination from DDI generates a serious problem when they stop unexpectedly. When the communication window stops right after the data frame sent by the DT, the confirmation frame is blocked. On the DT, it is assumed that the current frame is not successfully received. On the contrary, the DR has already confirmed and expects the next data frame. As a result, a mismatch of data sequence appears between the two devices. To prevent this situation, a sequence symbol is added in each data frame. The frame definitions are shown in Fig. 4.4.3.
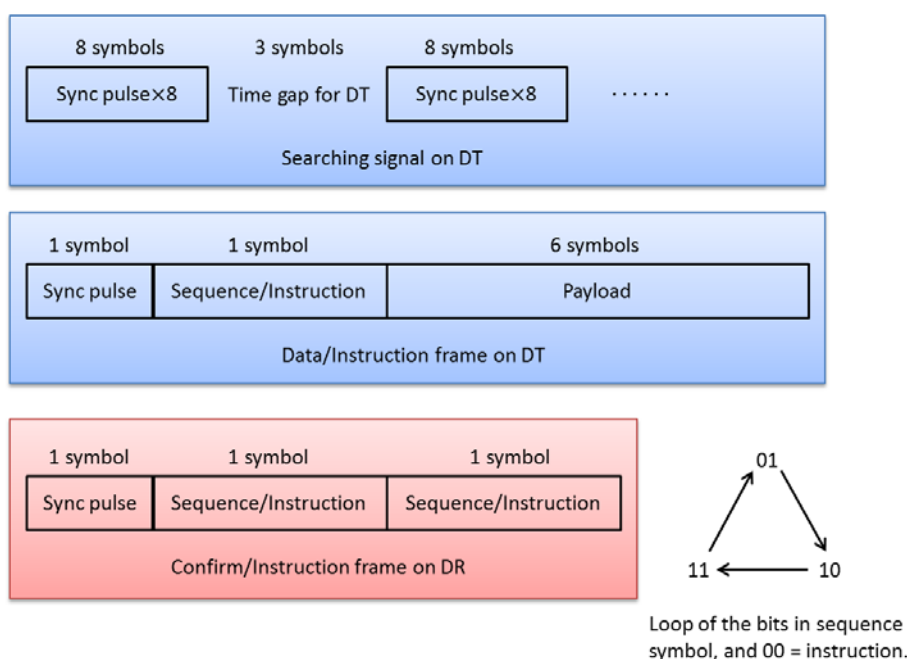
Fig. 4.4.3 Searching signal and frames definitions.

The symbol is defined as the $\binom{4}{2}$ OPPM described in section 4.2.1 that carries

two data bits in a symbol. The sequence symbol follows the synchronization pulse and has four statuses, in which 01, 10 and 11 forms a loop and represents the sequence, while 00 is reserved and signs the frame as an instruction. Therefore, when another communication session comes and the DR recorded a repeated sequence symbol, the data frame is ignored but it still confirms that to the DT. The confirmation frame is defined as in Fig. 4.4.3. It contains only two symbols that simply return the successfully received sequence symbol. Again 00 represents an instruction frame that has special utilities. The number of symbols in confirm/instruction frame is minimized to maximize the throughput efficiency.

In the condition that an error occurs in the sequence symbol of the data frame, the first error is supposed to be from noise and will be ignored. However, persistent errors in the sequence symbol indicates the sequence has been lost. Thus, when the second error occurs, the DR keeps sending instruction frames and the DT resets the sequence. The communication from DT restarts by sending an instruction frame to the DR. The reasons that the sequence symbol is redundant on the confirmation frame are: preventing the sequence loss caused from the error in the sequence symbol and providing enough symbols for the comparison of DDI on the DT.

4.4.2   OPPM Encoding

The OPPM symbols are generated from the timers in' output mode 4' while the timers in 'up' mode, which toggles the output when counting to the value stored in the CCR. An example of the single TA output operation of terminal 1 is shown in Fig. 4.4.4. In this example, the timer counts to TACCR0 and returns to zero in each timer cycle, and, by setting an output toggle at TACCR1, the output is triggered on and off in two cycles, therefore a pulse with 50% duty cycle and position controlled by TACCR1 is generated, the symbol duration of which is two timer cycles. Since the CCR1 value cannot be modified until the falling edge is triggered, it may not leave enough time to store another value before triggering the next rising edge. To avoid the race, TA and TB generate pulses alternatively; so that the CCR restore and pulse output operate

simultaneously on a different timer.
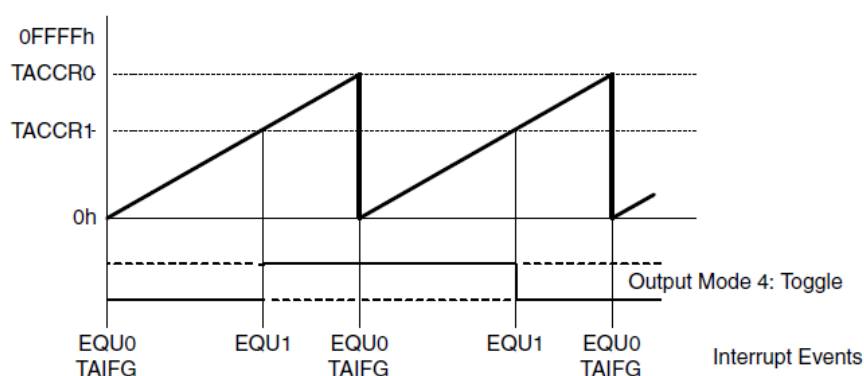
Adapted from [174]

Fig. 4.4.4 A sample of the single timer A output mode 4 operation when in the up mode.

In the actual program, the encoded output is assigned to CCR2. The timer workflow and the corresponding block diagram of the encoding program are shown individually in Fig. 4.4.5 and Fig. 4.4.6 on the following page. In the workflow in Fig. 4.4.5, TA outputs in the current symbol and TB in the next symbol, but the workflow continues and the output timer is switched in each symbol until the entire data frame is generated. In the current symbol period T, TACCR0 of the output timer is set to $\frac{T}{2}$ and then to $\frac{3T}{2}$ after the timer return to 0, which generates a pulse in the current symbol in two $\frac{T}{2}$ timer cycles and counts from $\frac{T}{2}$ to $\frac{3T}{2}$ in the next symbol, since TACCR2 $< \frac{T}{2}$, generating another pulse is avoided. Respectively in the current symbol, the value of next output is encoded and assigned to TBCCR2 of TB that is not used for output. When the next symbol begins, the output timer is switched by setting a TA output flag in the program, which is shown in Fig. 4.4.6. (For the detailed source code of the program, please see Appendix V)
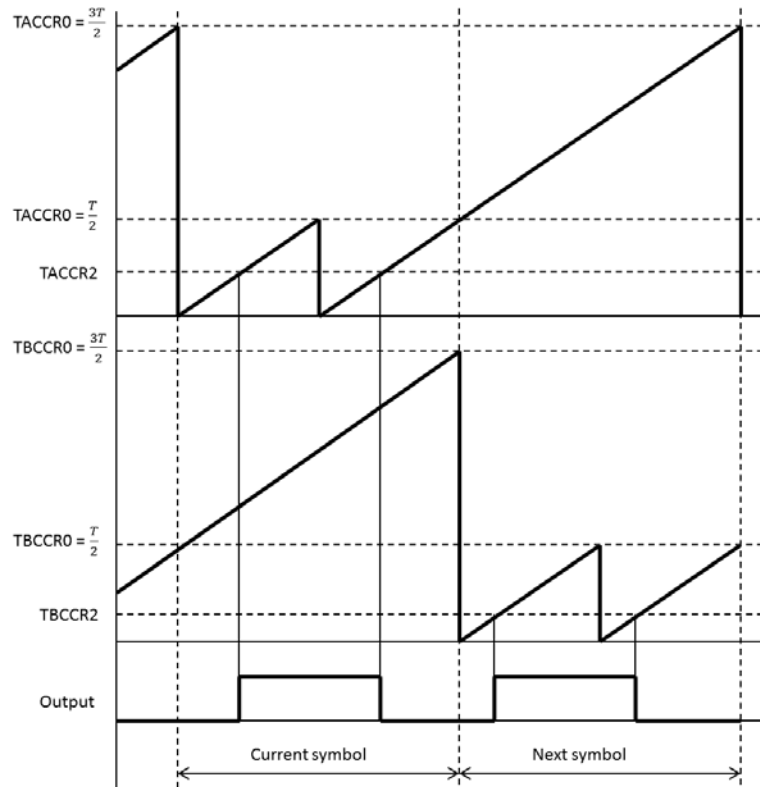
Fig. 4.4.5 Timer A and B alternative output workflow.
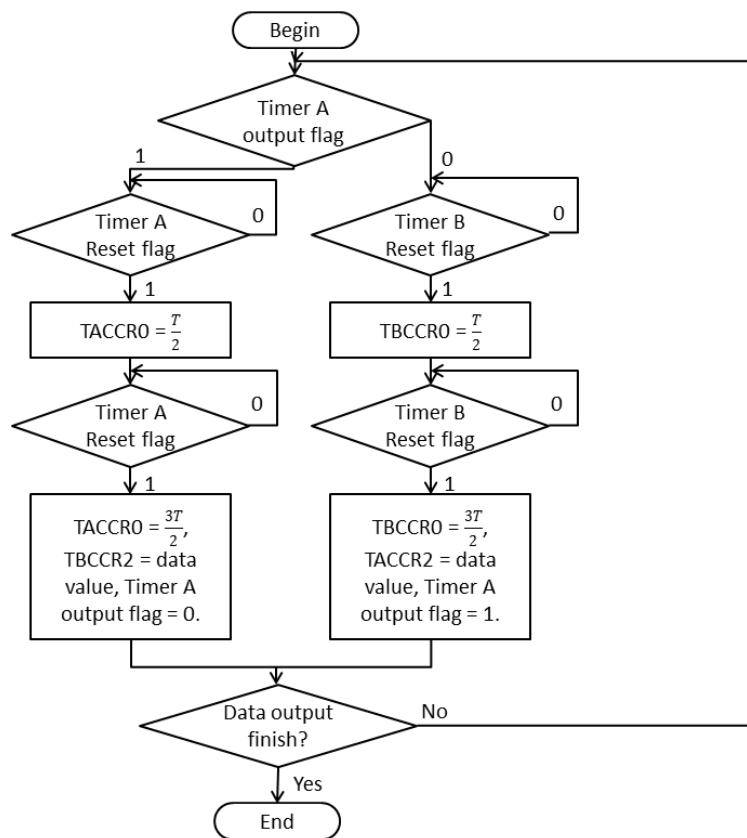
Fig. 4.4.6 Block diagram of the MSP430 microcontroller output program.

4.4.3   Software Latch and OPPM Decoding

Both the software latch and the OPPM decoding involve the DDI, in which the two timers are on the capture mode to trace the rising and falling edges of the input signals independently, the captured timer values are recorded on CCR1 of both timers. The results are then compared in real time after the falling edges of the pulses are captured, from which the microcontroller detects the boundaries of the communication session. The different roles of the DT and DR specified by the baseband protocol define different operations on responding to the first signal from the other using the DDI. Details of these operations are specified in Fig. 4.4.7 as follows and Fig. 4.4.8 on the following page.
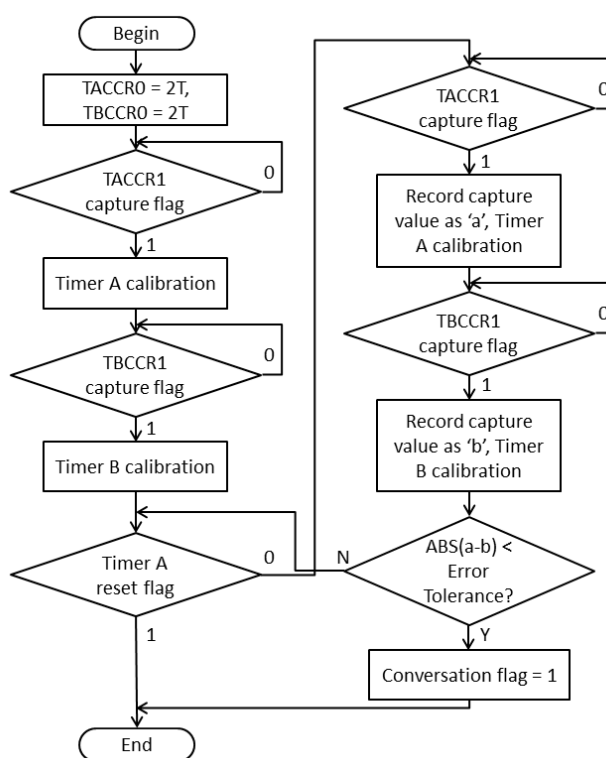
Fig. 4.4.7 Software latch function of DT

On the DT, as the first signal it will receive is the searching signal and the symbols are identical, the TA counts from the rising edge of one symbol to that of the next symbol and records the value in TACCR1, while the TB counts and stores the falling edges in TBCCR1. The difference between the two CCR1 values is computed. The

program latches the device into conversation by setting a conversation flag if the difference is smaller than an error tolerance; otherwise the timers recalibrate and counts the edges of the symbol after next, the procedure repeats until the conversation begins or no signal is detected in two symbol durations.
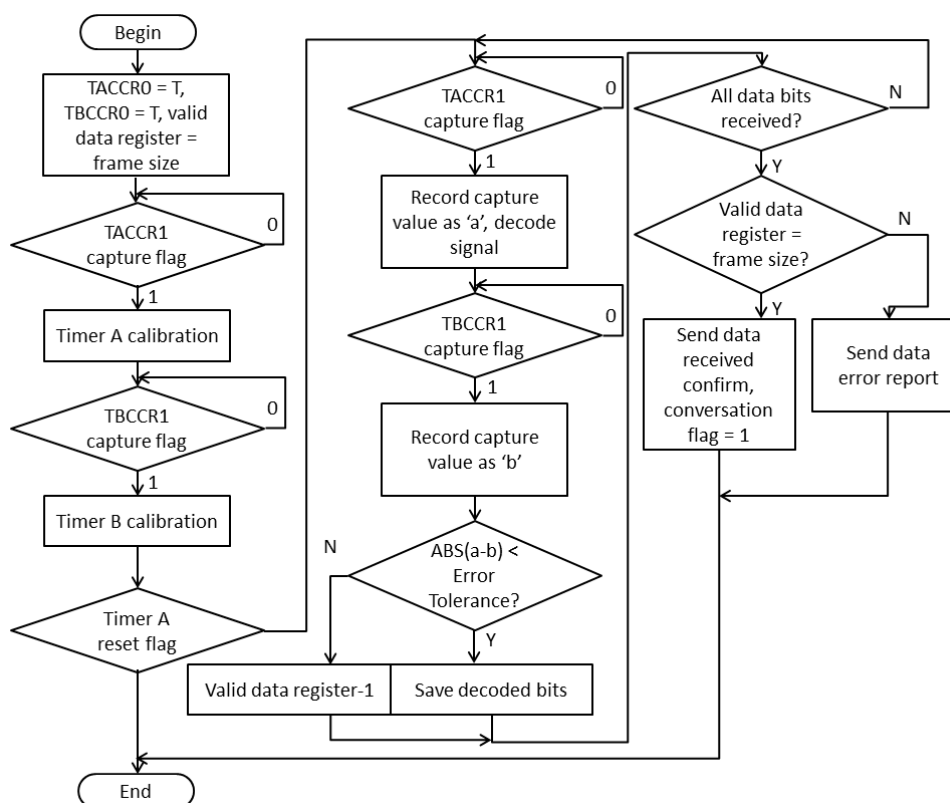
Fig. 4.4.8 Signal decoding and software latch function of DR.

As the first signal received by the DR is from a data frame, the OPPM decoding and the DDI are combined, therefore the timers count up to the symbol period and capture pulse edges of the data symbols in CCR1. Since the rising edge of a signal pulse comes ahead of the falling edge, the symbol is decoded after receiving the rising edge and the error between the two edges is computed when the falling edge is captured, avoiding insufficient time for execution of both the decoding and the DDI after the falling edge is detected. The DR only validates the incoming data frame to the DT by sending the confirmation frame and latches the device into the conversation if all bits in the data frame satisfy the error threshold of the DDI. (For the detailed source code of the program, please see Appendix V.)

The decoding process on the DR inside the conversation is similar to that of the first data frame, the number of symbols with DDI errors in each data frame is subtracted from the total symbol number of a frame, the result is saved in the Valid data register, from which the controller detects the end of the communication session. If two or more symbols in a data frame are received in error from the DDI, the communication session is considered ended. The decoding process of a symbol is the same on the DT, and the difference is the total amount of useful symbol is 2 in a frame compared to 7 on the DR, which is defined by the protocol.

The data rate is limited by the processing speed of the microprocessor on decoding the OPPM symbols, because the symbol needs to be long enough for the microprocessor to finish the decoding and the DDI. The situation can be improved if a different decoding scheme is applied. Instead of decoding when receiving the signal, the microcontroller only compares and saves the captured edge values of the timer from the incoming signal. The decoding is then performed in between the communication windows. In the periodic fast fading channel, the period of the communication window is much shorter than the rest of the time in the rotor spinning cycle. Therefore there is sufficient time to decode symbols with more data or OPPM with more complex codes, for example, Trellis Code. Since decoding is allocated in a different time, the procedure of the microcontroller in signal receiving is reduced to a large extent. Thus, the bandwidth can be extended and the data rate is enhanced.

4.5   Results and Discussions

4.5.1   The Communication Window of the Experimental Setup

The communication windows of the experimental setup are generated from rotating a perforated disc from a DC motor at the specified 12 Volts. The 'persistence mode' plot of the received communication window pattern from the channel fitted with a load resistor of 5k Ω is shown in Fig. 4.5.1.
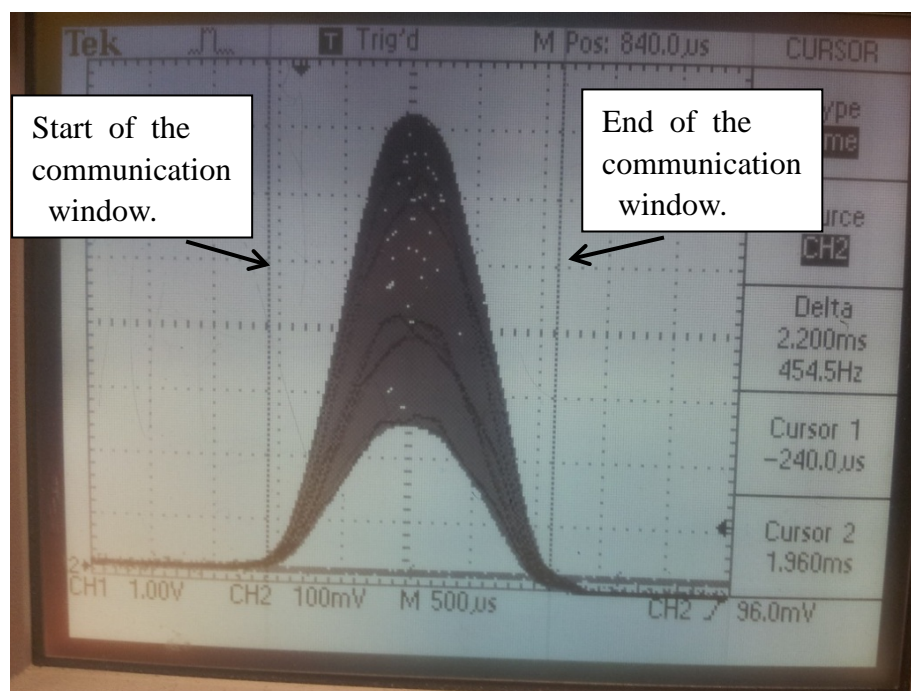
Fig. 4.5.1 Signal amplitude during the rotation period; the presence of the signal indicated the time length of the transmission window simulated experimentally

Due to the vibration from the disc rotation, the received signal varies in amplitude. The communication window is 2.2 ms, and the corresponding interval between communication windows is shown in Fig. 4.5.2, the average time of 10 such intervals is 254 ms, which is also the average time of a rotation cycle. As a result, the CWR of the experimental setup is 1:115, and the rotation speed is approximately 240 rpm. Given the distance between the hole on the disc and the rotation centre is 8.5 cm, the velocity of the hole is estimated to be 2.10 m/s. The analysis in section 4.1 indicates that the speed ratio of this lab simulation over the theoretical model is about 1:200. If an equal communication window is generated in the geometry of the theoretical model, and the distance between rotor rotation centre and the DT is assumed 1 m in the model, the rotation speed of rotor can be approximately 588 rpm. This rotation speed increases if the distance between rotor rotation centre and the DT is greater in the model.
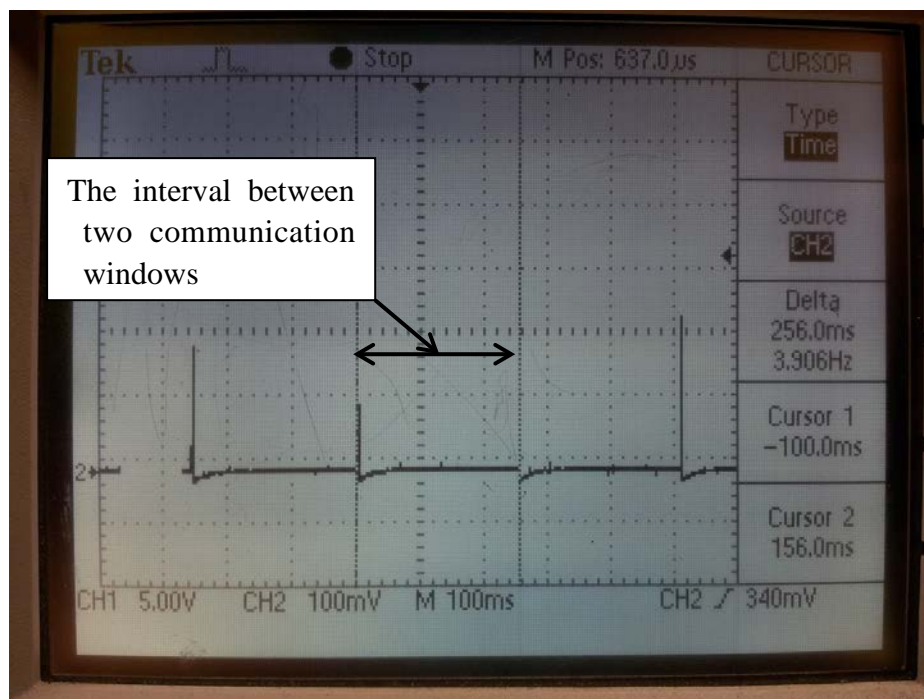
Fig. 4.5.2 The interval measurement between two windows of the experimental setup.

4.5.2   AGC Gain and Error Rate

From the discussion in section 4.3.1, the threshold is from the AGC amplifier and communication controller software, in which the AGC gain determines the power level of the threshold from (3.2.14) in the theoretical model and (4.2.9) in the IR transceiver circuit. As the signal power is related to the error rate, the setup of the pre-amplifier and the AGC amplifier then affects the bit capacity of the channel. As described in section 4.2.2, the threshold power level is related to $g_{r1}g_{r2(max)}$, which is adjustable by changing corresponding components in the circuit. However, due to the fact that the AGC amplifier has a positive feedback, the selections of the components for lower load resistors are found to be limited in the experiments to avoid self-resonance in the AGC amplifier. Thus, the results are from the 5 kΩ and 50 kΩ TIA feedback resistors.

Due to the author's limited experience in circuit design, the signal processing circuits generate cross interference when the duplex channels operate at the same time. As a result, the channel performance is estimated using the method based on one

channel as shown in Fig. 4.5.3.
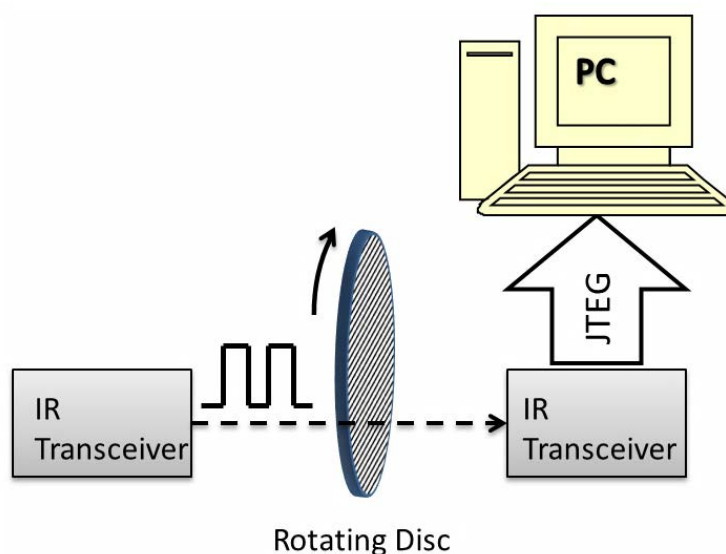
Fig. 4.5.3 The one-channel setup for error rate estimation.

Similar to the setup in Fig. 4.3.3, one IR transceiver generates identical pulse symbol signals at 200 kHz, which are transmitted through the hole on the spinning disc. The resulting data rate from 200 kHz is respectively slow since the DDI process performed in each received symbol on the microcontroller requires a considerable amount of time. The other IR transceiver reads the signal as OPPM symbols. The symbols are processed using DDI and treated as the data frame format in Fig. 4.4.3. The received frames are analysed in the period between the communication windows. As the symbols are identical, they should be the same bits if no error is presented. The errors can be detected if the received data contain different bits. The received bits and the errors are counted and saved in the RAM of the communication controller, which can be shown on the PC that is connected to the microcontroller via a JTAG debugger. The communication controller traps the program into a dead loop and turns on the LED indicator on the microcontroller circuit when collecting enough errors.

The BERs of different $g_{r1}g_{r2(max)}$ are shown in Fig. 4.5.4, in which the results are the averages from the received bits with 5 occurrences of errors. The results indicate that BER is increased on higher $g_{r1}g_{r2(max)}$, the maximum gain of the AGC

amplifier can be used to select the threshold for the photon current. For the two receivers, $g_{r1}g_{r2(max)}$ is 71 dB for the 10^{-6} BER. In Fig. 4.5.4, the BER for the 51 kΩ is lower than that for the 5.1 kΩ in the same $g_{r1}g_{r2(max)}$, but the difference is not significant in most of the gain levels. In the recorded data frames of 1000 rotor cycles from the two load resistors with BERs lower than 10^{-6}, the average amounts of the received equivalent data frames are 7.7 and 7.0 in a rotation cycle
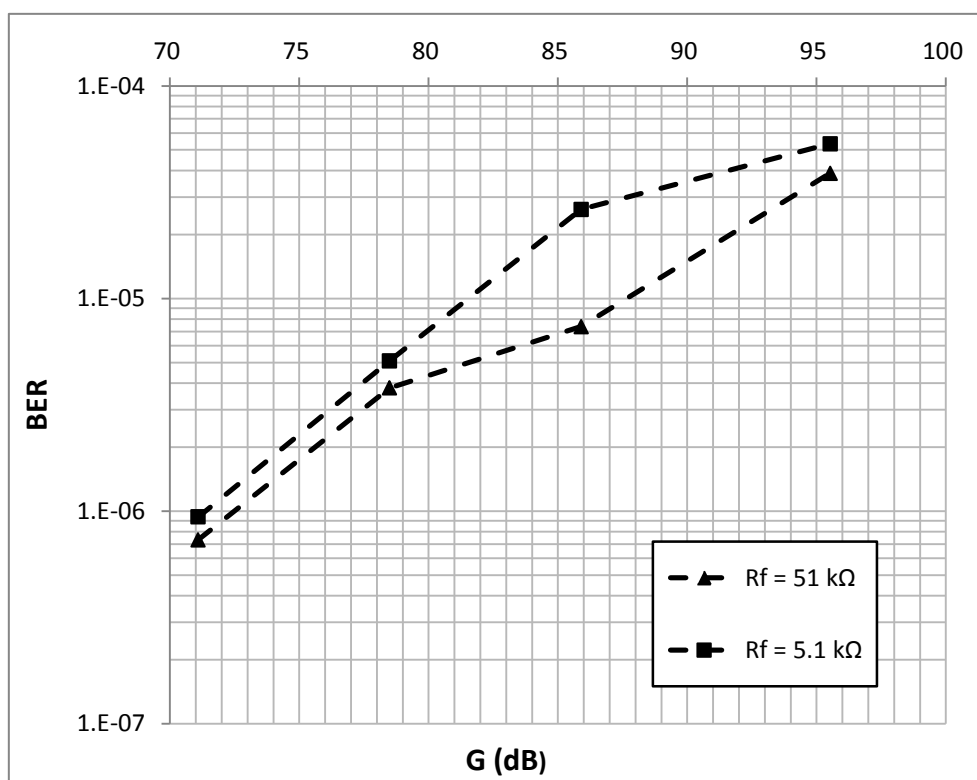
Fig. 4.5.4   The maximum gain of the AGC amplifier and BER of the channels with 5.1 kΩ and 51 kΩ resistors, in which $G = g_{r1}g_{r2(max)}$.

4.5.3   Performance of the Protocol and Power Consumption of DT in the Experimental Setup

While the modulation and the frame are defined in the protocol in section 4.4.1 and the symbol length is programmed, the throughput efficiency in these circumstances is affected by the processing speed of the communication controllers in

the form of turnaround times. Though the maximum turnaround times are defined in the programs of the devices to wait for the response from the other, the actual turnaround time is mainly from the procedures of the communication controller on the received frame and the preparation of sending the frame, which counts on the capacity and the programming of the microcontroller in our case. Connecting the two microcontrollers with wires, the turnaround times of DT and DR are measured via oscilloscope and the results are shown in Fig. 4.5.5. Since the pulse position varies in the useful symbols of the OPPM but the sync pulses are identical, the time between the rising edges of the sync pulses are measured instead of the time from the last symbol of a frame to the next sync pulse.
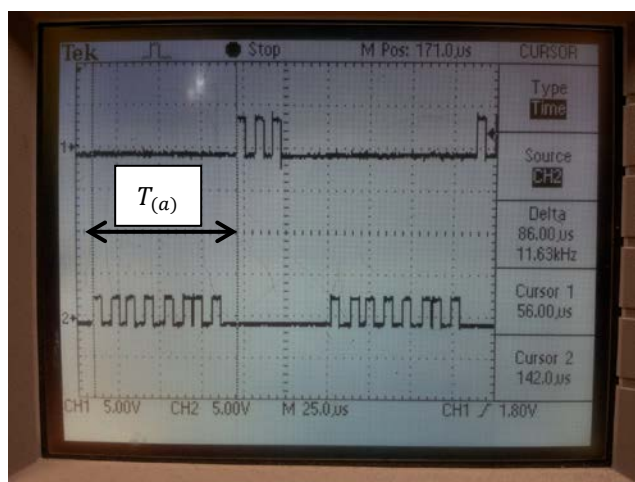
(a) Time from the sync pulse of the data frame to that of the instruction packet.
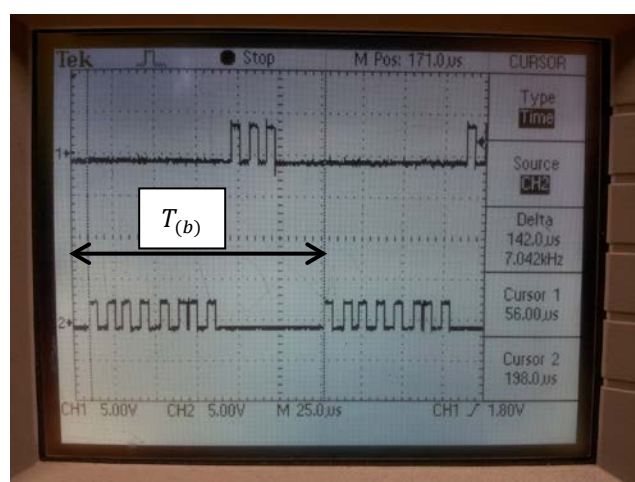
(b) Time between the sync pulses of one data frame to the next.

Fig. 4.5.5 The measurements of the micro controller turnaround times.

The results from (a) and (b) in Fig. 4.5.5 are $T_{(a)} = 86$ µs and $T_{(b)} = 142$ µs, and they contain the components as follows:

$$T_{(a)} = T_{dp} + T_{DR} \tag{4.5.1}$$

$$T_{(b)} = T_{dp} + T_{DR} + T_{ip} + T_{DT} \tag{4.5.2}$$

in which $T_{dp} = 80$ µs is the time of the data frame that the symbol length is 10 µs, $T_{cp} = 30$ µs is the time of the confirmation frame, T_{DR} and T_{DT} is the turnaround time of DR and DT. From (4.5.1) and (4.5.2), $T_{DR} = 6$ µs and $T_{DT} = 26$ µs. The turnaround time of the DT is longer, since the performance of the microcontroller is lower and the process is longer than that of the DR before giving the correct response.

If the delay from the IR transceiver circuit is ignored, the throughput efficiency only concerns the turnaround times of the communication controllers. The resulting information rate $R_i = \gamma r$ can be estimated from (3.1.21) and (3.1.22) if $b_W = b_r$:

$$R_i = \beta \frac{BT}{T_R} \tag{4.5.3}$$

And β of the protocol is:

$$\beta = \frac{2(T_{dp} - 2T_s)}{T_{dp} + T_{DR} + T_{ip} + T_{DT}} \tag{4.5.4}$$

in which T_s is the symbol duration and $T_{dp} - 2T_s$ represents the duration of the information bits in the data frame in which the first two symbols are used for synchronization and sequence. BT is obtained from the results of the average amount of frames in one rotation cycle $\overline{N_p}$ from section 4.5.2, in which:

$$BT = \frac{\overline{N_p} T_{dp}}{T_s} \qquad (4.5.5)$$

Inserting (4.5.4) and (4.5.5) into (4.5.3), R_i becomes:

$$R_i = \frac{2(T_{dp} - 2T_s)\overline{N_p} T_{dp}}{(T_{dp} + T_{DR} + T_{ip} + T_{DT})T_R T_s} \qquad (4.5.6)$$

From the discussion of the DT's power consumption in section 2.3.2, the power consumption of the device is in two conditions, depending on whether the LED is transmitting signals.

The measurement of current using multi-meter recorded 25 mA in receiving mode. The waveform of the voltage on a 3.6 Ω resistor, which is series connected between the DT circuit and the ground, is shown in Fig. 4.5.6, in which the peak and bottom values are 512 mV and 136 mV. If the voltage bias of the series resistor is neglected, the average current of the transmitting mode is approximately 90 mA. On a 5 V power supply voltage, the power consumptions are $P_R = 125$ mW and $P_T = 450$ mW in (2.3.6). r_T can be estimated as:

$$r_T = \frac{\overline{N_p} T_{dp}^2}{(T_{dp} + T_{DR} + T_{ip} + T_{DT})T_R} \qquad (4.5.7)$$

The information rates calculated using (4.5.6) and the estimations of power consumption from (2.3.6) and (4.5.7) are summarized in Table 5. The difference of information rates between the two load resistors is small for a distance of 0.1 m, but both of the channels exhibit a significant reduction for 0.2 m, in which the reduction of the 51 kΩ channel is smaller than that of the 5.1 kΩ channel. As the proportion of communication session period in the time of a rotation cycle is not large, the overall power consumption is not affected by the data transfer of different load resistors, and stays at 126 mW.
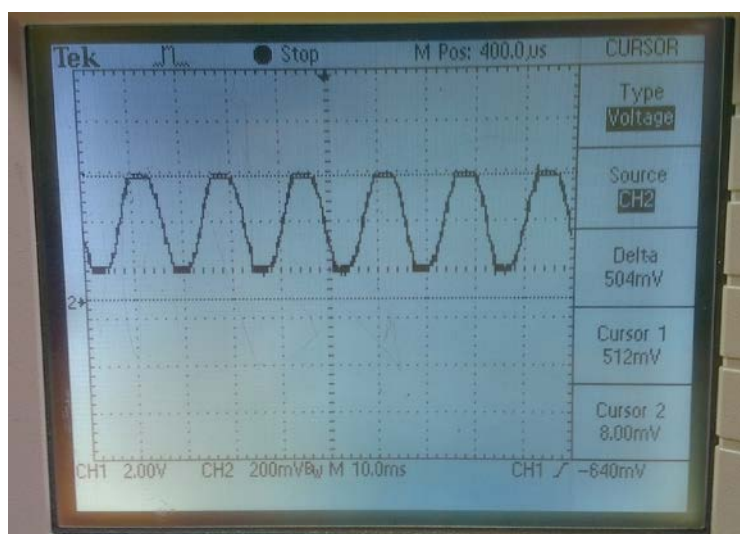
Fig. 4.5.6 The voltage waveform of the 3.6 Ω series resistor.

R_L	$\overline{N_p}$ (0.1m)	$\overline{N_p}$ (0.2m)	R_i(0.1m) (bits/s)	R_i(0.2m) (bits/s)	r_T (0.1m)	r_T (0.2m)	$\bar{P}$ (mW)
5.1 kΩ	6.988	4.608	208	137	1.38E-03	9.13E-04	126
51 kΩ	7.661	5.930	228	176	1.52E-03	1.17E-03	

Table 5 The results of information rates and power consumptions of receivers with feedback resistors of 5.1 kΩ and 51 kΩ.

4.6   Summary and Further Work

In this chapter, the experimental setup to simulate the actual condition of the periodic fast fading channel has been presented, and the difference of the communication window of the experimental setup and the model has been theoretically analysed. What is more, the IR transceiver circuit has been developed and the DDI to determine the edges of the communication session has been demonstrated on OPPM. The baseband protocol is also designed for maintaining the communication of secure and organized data transfer in the periodic channel. The results show that the experimental setup generates a 2 ms communication window, in which the 50 kΩ

channel can transfer data at the information rate up to 228 bit/s in 10^{-6} BER, at a distance of 0.1 m. The error rate and power performance of two load resistors have been compared, and the influence of the AGC threshold gain to the error rate has been presented.

Aiming at developing a commercial product for the application, the following problems needs to solved in further work:

1. The MSP430 microcontroller provides an ideal energy efficient solution, but the bit rate is limited by the processor speed. For an improvement the communication controller on the DT can be developed using the FPGA technique, from which a fast processor of the specific protocol can be implemented and the power consumption can be reduced.

2. The power consumption of the DT needs to be optimized for a longer battery life or adoption of the power scavenging methods.

5 The EM Environment Simulation Model

The working environment of the optical transceivers is the interior of a motor or generator, in which the EM field is generated from the coils on the rotor or stator. The effects of the EM field can be both beneficial and restrictive. On one hand, the EM field is one of the potential power sources for the DT on the rotor. Nevertheless, on the other hand, the EM field may also generate interference to the electronics of the transceiver. Thus, the internal EM field needs to be investigated, so that the effects on the power source and interference can be estimated. The transceivers are located mainly on the surface and near the surface space of the rotor and stator structure, and the distribution of the EM field in this area is the combinative conductive effects of the rotor, stator, shaft and coils. Therefore, for a graphical and detailed analysis, a 3D optimized model of the structure is built to simulate the surface space EM field. The Model is designed in Solidworks with reference to an actual motor and imported into Comsol Multiphysics for the analysis of the magnetic field and electric field of the space on the stator and rotor surface, in which the field source is the coil current.

5.1   The Structural Model

The 3D model designed to investigate the surface space EM field with the basic components of a motor is shown in Fig. 5.1.1. The rotor and stator sizes and designs are referred to a real squirrel cage motor. To reduce the required computing resource to an acceptable level for personal computers and workstations, the structure is reduced to a portion of the real design, only 1/3 of the whole stator is presented. The winding of the coil is integrated as a whole wire. What is more, the coils in the real motor are bundled

and crossed over as shown in Fig. 5.1.2, but this is difficult to represent in the software design. Therefore the top of the mock coils are sliced and 2/3 of each coil is removed, allowing them to cross each other without overlapping. The whole reduced motor structure is surrounded by an air column, in which the EM field is investigated.
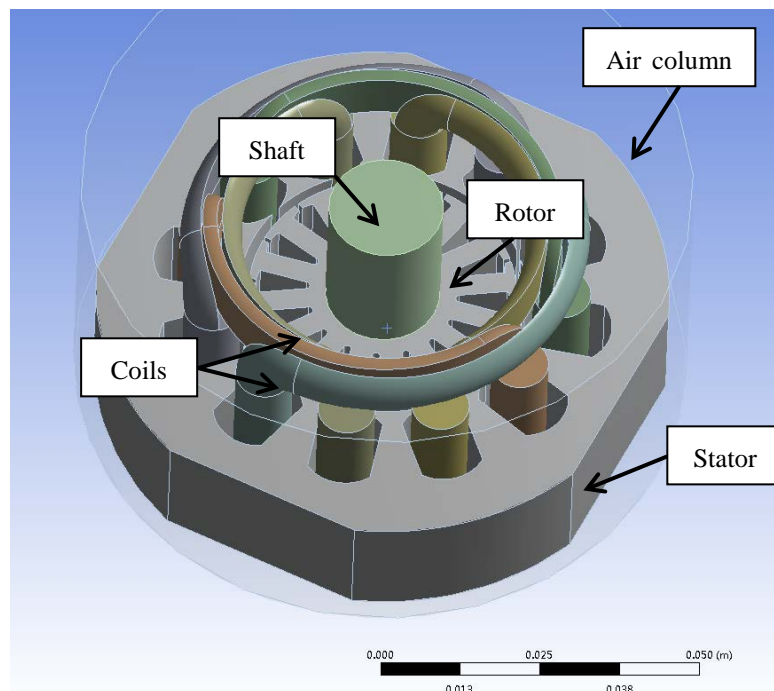
Fig. 5.1.1 The model of a motor with basic components.

Fig. 5.1.2 The bundled and crossed over coils in a real motor

The components of the model are defined as follows. Materials are assigned soft iron for the stator, rotor and shaft, copper for the mock coils. Because the top of coils is only 1/3 of the original size, to reduce the influence from the decreased electric conduction area, the electric conductivity of these sliced parts are modified in the material, which is three times the electric conductivity of copper. Assuming no axial EM field is generated on the cutting surface of the model motor and the whole structure including the air column is absolutely isolated from the outer environment, the configuration of electric and magnetic boundaries can be summarized as:

1. Surfaces with outside contacts are in electrical insulation except the inputs of the coils.

2. The inputs of the coils are set as current input on one end and electrical ground on the other end of each coil. These definitions follow the current directions of the real motor, including the phase differences of the motor three-phase power supply.

3. Surfaces with outside contacts are all in magnetic insulation.

The source of the EM field in the model is the induction from the current in the coils. The simulation is computed in Comsol Multiphysics using FEM, which implies an equivalent electric field from Lorentz force in quasi-static condition and yields:

$$\nabla \times \vec{H} = \sigma\left(\vec{E} + \vec{v} \times \vec{B}\right) - \frac{\partial \vec{D}}{\partial t} + \vec{J_e} \qquad (5.1.1)$$

In which $\vec{H}$ is the magnetic field intensity, σ is electric conductivity, $\vec{E}$ is the electric field intensity, $\vec{v}$ is the velocity, $\vec{B}$ is the magnetic flux intensity, $\vec{D}$ is the electric flux density and $\vec{J_e}$ is the electric current density. According to [176] and [177]:

$$\vec{H} = \frac{\nabla \times \vec{A}}{\mu} \qquad (5.1.2)$$

$$\vec{E} = -\nabla\phi - \frac{\partial\vec{A}}{\partial t} \tag{5.1.3}$$

$$\vec{B} = \mu\vec{H} \tag{5.1.4}$$

$$\vec{D} = \varepsilon\vec{E} \tag{5.1.5}$$

In these formulas, $\vec{A}$ is the magnetic vector potential, μ is the magnetic permeability, ϕ is the magnetic scalar potential and ε denotes the electrical permittivity. Integrating (5.1.2) ~ (5.1.5) into (5.1.1):

$$\nabla\times\left(\frac{\nabla\times\vec{A}}{\mu}\right) = \sigma\left(-\nabla\phi - \frac{\partial\vec{A}}{\partial t} + \vec{v}\times\left(\nabla\times\vec{A}\right)\right) + \frac{\varepsilon\partial(\nabla\phi)}{\partial t}$$
$$+ \frac{\varepsilon\partial^2\vec{A}}{\partial t^2} + \vec{J_e} \tag{5.1.6}$$

For time-harmonic analysis, (5.1.6) becomes:

$$(j\omega\sigma - \omega^2\varepsilon)\vec{A} + \nabla\times\left(\frac{\nabla\times\vec{A}}{\mu}\right) - \sigma\vec{v}\times\left(\nabla\times\vec{A}\right)$$
$$+ (j\omega + \sigma)\nabla\phi = \vec{J_e} \tag{5.1.7}$$

In which ω is the angular frequency of the current source.

To reduce the mesh size for less computing resource and preserve the necessary accuracy and detail, meshing of the FEM model has been optimized, aiming at controlling the densities of mesh in different areas, which is shown in Fig. 5.1.3. Firstly, the symmetrical rotor is meshed regularly using rectangular units, then those rectangular meshes are deformed into triangular ones. Secondly, the mock coils are meshed by triangular units at a finer level than the other components. Furthermore, to coordinate the different meshing methods of the two components, meshing regulations

of shaft, stator and air column are derestricted [178]; therefore in the connections between components the meshes are finer than those in the other areas. Thus, even meshes in the symmetric structures produce similar error amounts, avoiding error concentration; computing processes are reduced in the areas with weaker fields and fewer meshes.
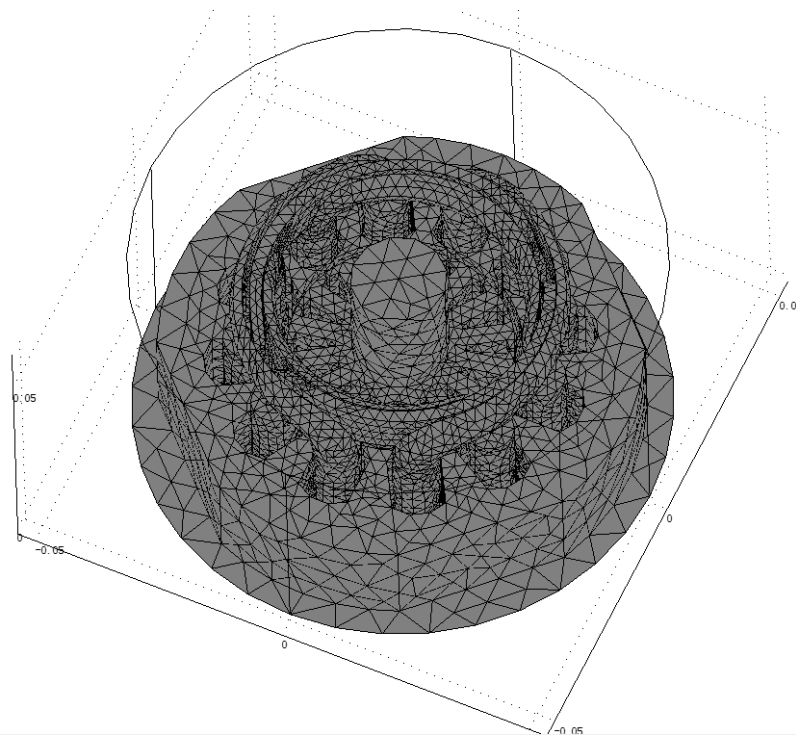
Fig. 5.1.3 The controlled meshing of the motor simulation.

5.2   Results and Discussion

The results are obtained from the harmonic propagation analysis of the model using a stationary solver [179]. With the optimized meshing method, the degree of freedom is reduced to about one million [180, 181]. The rotation speed of the rotor and shaft is set at 1000 rpm, the current source of the coils is assumed 10 A in real coil wire with 100 circles of winding, from which in the model each input current boundary of the mock coils is 1000 A.

The magnetic flux density of the upper surface of the rotor and stator is shown on

page 130 in Fig. 5.2.1 (a) and that of the position 5 mm above the upper surface is shown in Fig. 5.2.1 (b). The magnetic field on the upper surface still shows a strong influence of the rotor and stator structure, and the field is above the air gap between the stator and the rotor. Comparatively, in a 5 mm higher position, the spatial effect is more significant, and the magnetic field is stronger between nearby coupling coils. What is more, the maximum magnetic flux density drops approximately ten fold, from 1.07×10^{-5} T to 1.08×10^{-6} T. Therefore, to scavenge power from the magnetic field, the conductor should be placed close to the air gap.

The potential interference source, the electric field of rotor is shown in Fig. 5.2.2 (a) and (b). Similar to the magnetic field analysis, the upper surface and the position 5 mm above is compared. The distribution of electric field is determined by the coils in both positions. But because of the shield effect of the stator teeth, the electric field of the upper surface is concentrated more near the gaps of the teeth. Thus, to avoid the potential interference from coils, the transceiver should be located near the centre of the motor.
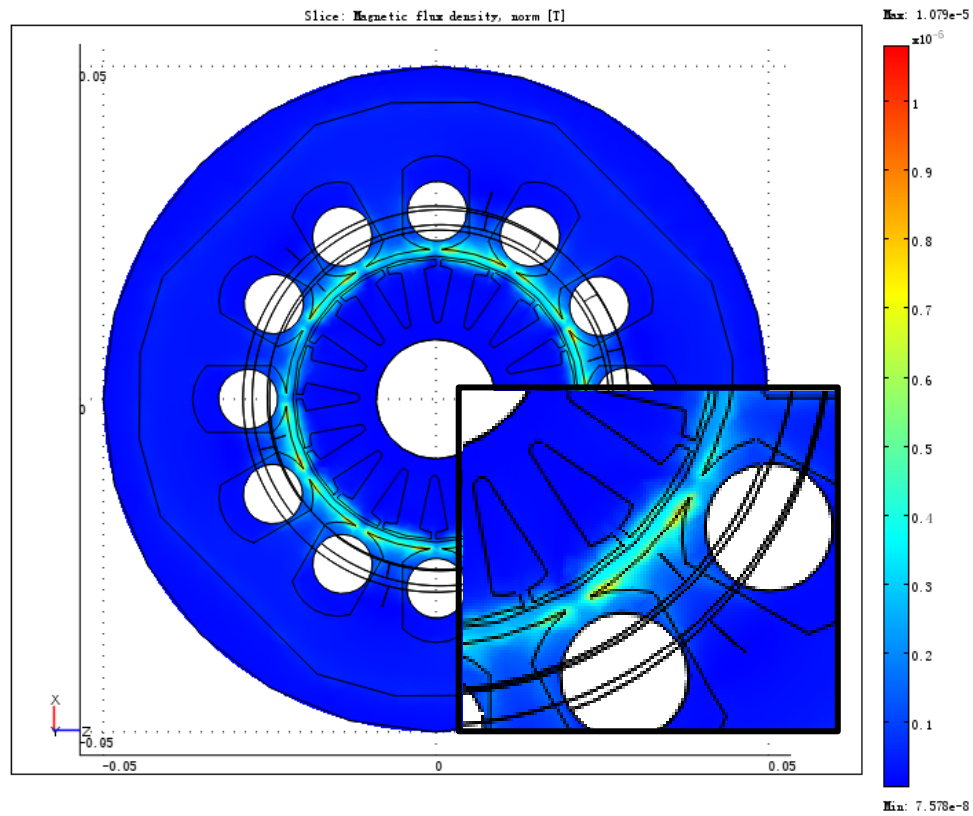
(a) Magnetic flux density of the upper surface of the motor
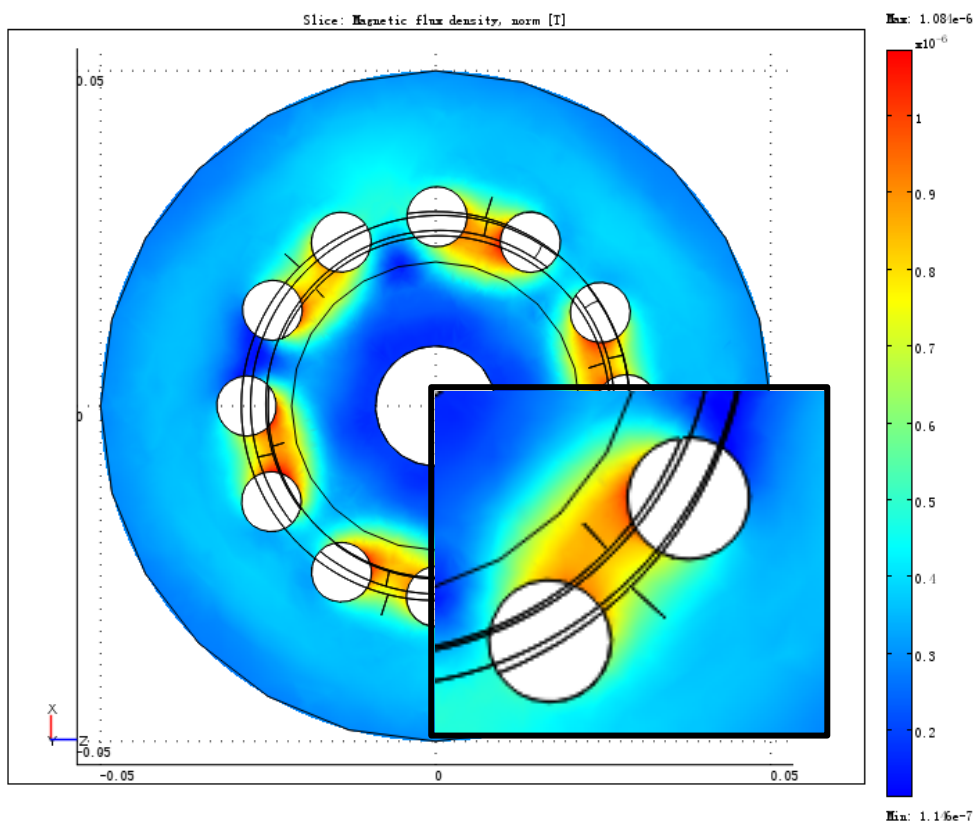
(b) Magnetic flux density of the position 5 mm above the rotor and stator surface

Fig. 5.2.1 The magnetic flux densities.
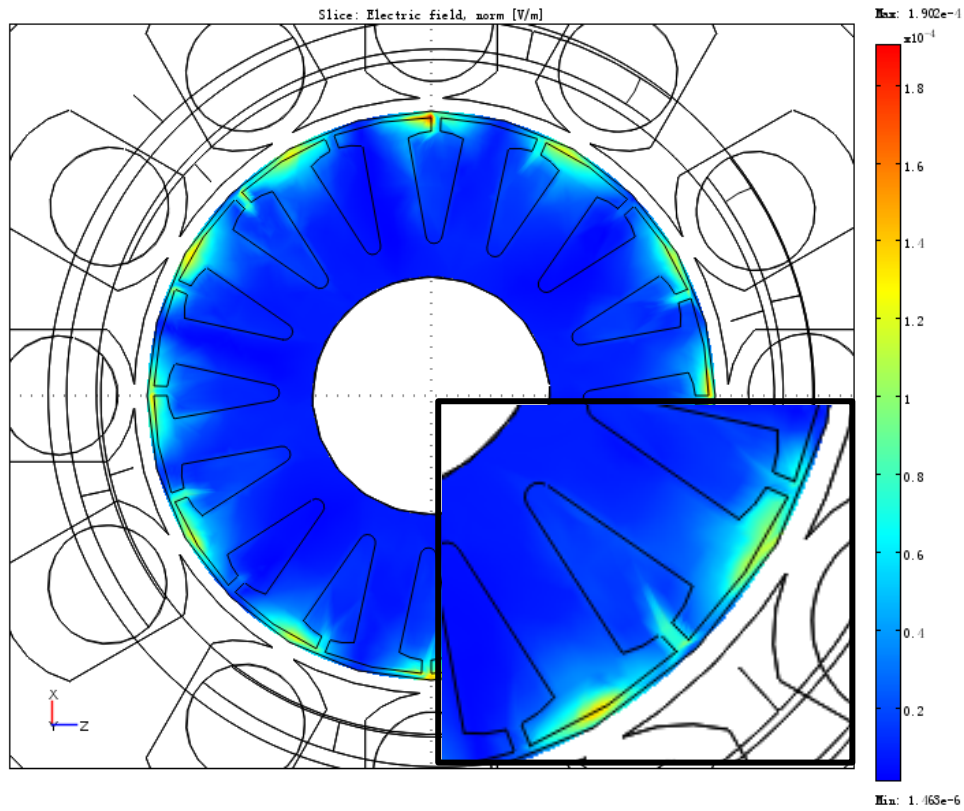
(a) Electric field of the upper surface of the motor
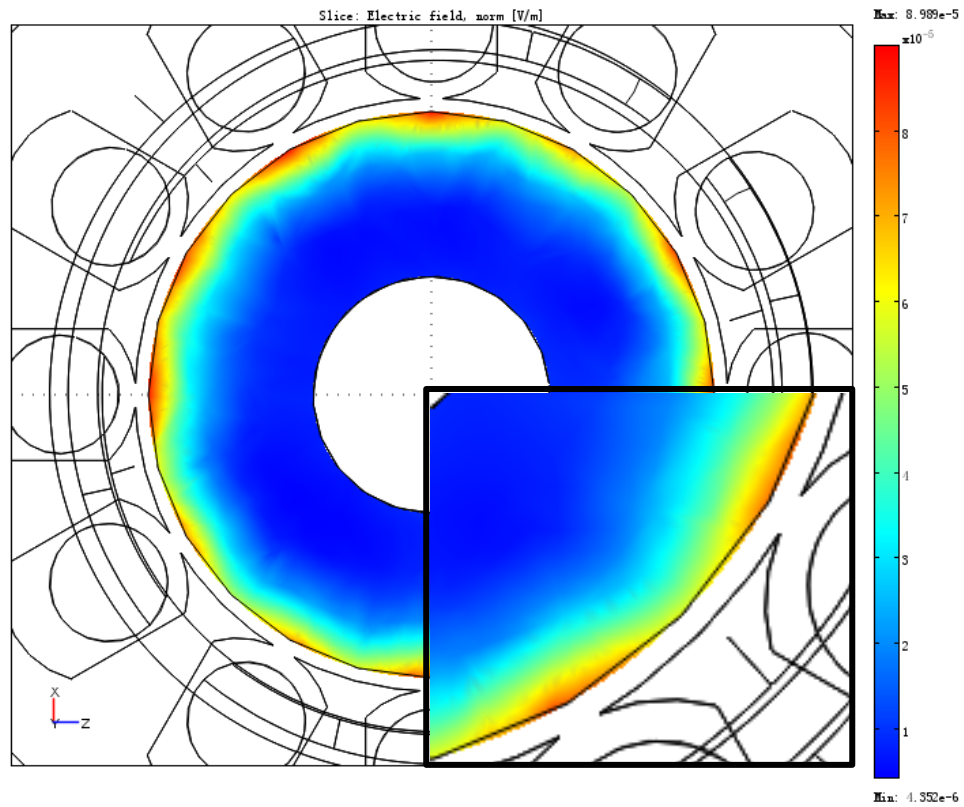
(b) Electric field of the position 5 mm above the upper surface

Fig. 5.2.2 The electric fields.

5.3   Further Work

Due to the considerable amount of errors brought by deformed meshes mainly in the air gap in the resent model mesh size, the EM field transient analysis of rotor rotating simulation cannot converge, which also means that an estimation of the electric induction that can be generated from the magnetic field when the transceiver is spinning with the rotor is not feasible. If the computing resource is sufficient to afford the finer but larger sized mesh with acceptable errors in the transient analysis, the coil structure and corresponding circuit can be mounted and defined in the model, from which an accurate estimation of the scavenged induction electric power from the magnetic field can be calculated.

6 Conclusions and Further Work

This thesis has discussed the sensor data transfer on OW communication for the applications of rotor detection and diagnostics. Aiming for more flexibility on device mounting location, the OW LOS channel is limited to a short period in each rotation cycle and large signal fluctuations are introduced due to the movement of the device. This OW LOS channel has been named the periodic fast fading channel. To investigate the possibility and performance of optical communication in this channel, models for the fast fading channel, the TIA and the AGC amplifier have been developed. What is more, an experimental setup has been implemented to gain practical results and demonstrate the software and hardware designs for the application. An FEM model of the EM environment in the rotor-stator structure has been established to study the EM field and its negative (as interference source) and positive (as a power scavenging source) effects.

In chapter 2, the review of the rotor monitoring methods led to the conclusion that direct methods are more time efficient and need fewer parameters compared to indirect methods, but generated difficulties in powering the device on the rotor and restrictions in the device installation location. This scenario bypasses the restriction of the installation location, but the power consumption estimation for a device containing a microcontroller and a IR transceiver indicated that more than one source is needed to supply the whole device using power scavenging from the surrounding environment.

In chapter 3, the results from the channel model showed that the bit capacity was influenced by several parameters from the receiver and the geometry. The bandwidth cut off of the load resistor receiver front end can be influenced by two factors, which are the -3 dB frequency for high resistors, and insufficient bit power to go through the threshold for low resistors. Therefore, for a certain noise condition and geometry, there is an optimal resistor value for maximizing the bit capacity. With the

consideration of power efficiency, lower resistors can be more suitable for applications that require large bit capacity. But when higher bit capacities are not required, higher resistors are preferred because the distance between transceivers can be longer. From the model of the AGC amplifier, the dynamic range of higher resistors is wider but the integrator delay can be reduced from lower loop gain. The bandwidth extension from the TIA for higher resistors cannot reach the same maximum bit capacity of the lower resistors. But the improvement of bit capacity from TIA is still considerable in a certain resistor range, such as between 5 kΩ and 50 kΩ in simulation.

In chapter 4, the experimental setup for demonstration of the fast fading channel was analysed by comparing the communication windows from the geometry of the experimental setup to that of the theoretical model in chapter 3. In generating a communication window in which the periods are similar, the speed of the hole on the spinning disc in the experimental setup was about 1/200 of the LED speed in the model. Moreover, the functions and setup of the developed IR transceiver circuit were introduced. The forward voltage of the envelope detector diode limited the sensitivity of the AGC amplifier and a biased envelope detector was proposed to enhance the sensitivity. The DDI was developed and demonstrated to detect the boundary of the communication session, and using the DDI requires OPPM as the modulation format. Compared to OOK, OPPM has higher demand on power to achieve the same bit rate. By adapting OPPM to the model in chapter 3, it was shown that the raised power level of OPPM did not influence the bit capacity to a large extent. A baseband protocol is established to realize the data transfer using DDI and OPPM in the fast fading channel. To maximize the data throughput, the frames sent by DR contained fewer symbols than those sent by DT. The sequence symbol implemented in the data frame to protect the data frame order, and the sequence could be reset if an error occurred. The results of the experiments show that lower maximum gain of the AGC amplifier produces higher error rate and that the error rate of the 5 kΩ load resistor is higher than the 50 kΩ on the same maximum gain. What is more, the actual turnaround times of the communication controllers were measured. Based on the turnaround times, the

performance of the device was estimated as: information rate up to 200 bits/s on 126 mW power, with 50 kΩ load resistor.

Results of the FEM motor model in chapter 5 indicated that if the magnetic field inside the rotor was considered as the power scavenging source, the power harvester should be located near the air gap between the stator and the rotor or close to the coils. If the electric field is considered generating EMI, the devices could not be installed near the air gap on the rotor, where the electric field is stronger. These factors should be considered in the design of an actual device.

The solution of the OW data transfer in the fast fading channel included the design of the IR transceiver, the communication controller and the protocol. Since the power of the DT was limited, the selection of the load resistor value for the receiver front end tended to be high, but the receiver bandwidth should be sufficient for the required bit capacity. A TIA may be introduced to extend the bandwidth and reach a higher bit capacity, but the raised power consumption needs to be considered. The AGC amplifier was designed to maintain a respectively stable output level in the communication session. In practice the stable output level was decided by the maximum of the gain and the sensitivity of the detector. In the communication controller, the boundaries of the stable output level were detected by DDI. The specific baseband protocol uses a sequence symbol to prevent the errors in each data frame sequence caused by the periodic transmission. The device power estimation was considered in two scenarios: if the rotor rotation cycles were regulated, the receiver could be turned off in the interval between the communication windows; if not the receiver remained functional in the entire rotation cycle. During the communication window, there were two power conditions for a functioning device, depending on whether the transmitter was in operation; the receiver was on, in both conditions.

Further work could be concentrated in three areas, which are: the model of the OW channel, the hardware development, and the FEM model of the stator-rotor structure. As the model of the OW channel considered an ideal geometry for the transceiver to reduce the parameters for calculations, the more complex geometry in Appendix I needs to be further studied. What was more, the rotation speed of the rotor

is assumed constant in the model, but the jitter caused by mechanical vibrations could affect the fast fading channel, and therefore should be investigated. The problem of the IR transceiver circuit interference must be solved for further development. Power consumption reduction, with improvement on performance, could be realized from further development using FPGA techniques. In the FEM modelling, the static model should be replaced by a dynamic model which includes the effects of the spinning rotor, in order to perform the estimation of electric induction power scavenging.

REFERENCES

[1]   P. Tavner, L. Ran, J. Penman, and H. Sedding, (2008) *Condition Monitoring of Rotating Electrical Machines*. Herts: Institution of Engineering and Technology.

[2]   C. Concari, G. Franceschini, and C. Tassoni, (2008) "Differential Diagnosis Based on Multivariable Monitoring to Assess Induction Machine Rotor Conditions," *Industrial Electronics, IEEE Transactions on,* vol. 55, pp. 4156-4166.

[3]   Z. Huang, M. Xu, and X. Zhou, (2011) "Research for rotor monitoring system based on virtual instrument technology," in *Computer Science & Education (ICCSE), 2011 6th International Conference on*, SuperStar Virgo, Singapore, pp. 508-511.

[4]   W. T. Thomson, (1994) "On-line current monitoring to detect electrical and mechanical faults in three-phase induction motor drives," in *Life Management of Power Plants, 1994., International Conference on*, Edinburgh, UK, pp. 66-73.

[5]   I. Jaksch and J. Bazant, (2005) "Demodulation methods for exact induction motor rotor fault diagnostic," in *Diagnostics for Electric Machines, Power Electronics and Drives, 2005. SDEMPED 2005. 5th IEEE International Symposium on*, pp. 1-5.

[6]   H. Abu-Rub, A. Iqbal, S. K. M. Ahmed, J. Guzinski, M. Adamowicz, and M. Rahiminia, (2011) "Rotor broken bar diagnostics in induction motor drive using Wavelet packet transform and ANFIS classification," in *Electric Machines & Drives Conference (IEMDC), 2011 IEEE International*, pp. 365-370.

[7]   R. Wieser, C. Kral, F. Pirker, and M. Schagginger, (1999) "On-line rotor cage monitoring of inverter-fed induction machines by means of an improved method," *Power Electronics, IEEE Transactions on,* vol. 14, pp. 858-865.

[8]   C. Kral, R. S. Wieser, F. Pirker, and M. Schagginger, (2000) "Sequences of field-oriented control for the detection of faulty rotor bars in induction machines-the Vienna Monitoring Method," *Industrial Electronics, IEEE Transactions on,* vol. 47, pp. 1042-1050.

[9]   R. S. Wieser, C. Kral, and F. Pirker, (1998) "The Vienna induction machine monitoring method; on the impact of the field oriented control structure on real operational behavior of a faulty machine," in *Industrial Electronics Society, 1998. IECON '98. Proceedings of the 24th Annual Conference of the IEEE*, Aachen, Germany, pp. 1544-1549 vol.3.

[10]   G. Zhi, T. G. Habetler, and R. G. Harley, (2005) "A robust rotor temperature estimator for induction machines in the face of changing cooling conditions and unbalanced supply," in *Electric Machines and Drives, 2005 IEEE International Conference on*, San Antonio, USA, pp. 591-596.

[11]   "IEEE Standard Test Procedure for Polyphase Induction Motors and Generators," *IEEE Std 112-2004 (Revision of IEEE Std 112-1996),*

[12]   G. Zhi, T. G. Habetler, R. G. Harley, and R. S. Colby, (2005) "A novel online rotor temperature estimator for induction machines based on a cascading motor parameter estimation scheme," in *Diagnostics for Electric Machines, Power Electronics and Drives, 2005. SDEMPED 2005. 5th IEEE International Symposium on*, Vienna, Austria, pp. 1-6.

[13]   C. Kral, T. G. Habetler, R. G. Harley, F. Pirker, G. Pascoli, H. Oberguggenberger, and C. J. M.

Fenz, (2003) "Rotor temperature estimation of squirrel cage induction motors by means of a combined scheme of parameter estimation and a thermal equivalent model," in *Electric Machines and Drives Conference, 2003. IEMDC'03. IEEE International*, Madison, USA, pp. 931-937 vol.2.

[14] L. Yanqiu and C. Weiliang, (2009) "An online monitoring system of friction fault based on acoustic emission technology," in *Power Electronics and Intelligent Transportation System (PEITS), 2009 2nd International Conference on*, Shenzhen, China, pp. 329-332.

[15] M. S. N. Sdid and M. E. H. Benbouzid, (2000) "H-G diagram based rotor parameters identification for induction motors thermal monitoring," *Energy Conversion, IEEE Transactions on,* vol. 15, pp. 14-18.

[16] M. A. Jarrah and A. R. Al-Ali, (2004) "Web-based monitoring and fault diagnostics of machinery," in *Mechatronics, 2004. ICM '04. Proceedings of the IEEE International Conference on*, Istanbul, Turkey, pp. 525-530.

[17] A. Ordaz-Moreno, R. de Jesus Romero-Troncoso, J. A. Vite-Frias, J. R. Rivera-Gillen, and A. Garcia-Perez, (2008) "Automatic Online Diagnosis Algorithm for Broken-Bar Detection on Induction Motors Based on Discrete Wavelet Transform for FPGA Implementation," *Industrial Electronics, IEEE Transactions on,* vol. 55, pp. 2193-2202.

[18] R. Wieser, C. Kral, F. Pirker, and M. Schagginger, (1997) "Condition monitoring of inverter fed induction machines by means of state variable observation," in *Electrical Machines and Drives, 1997 Eighth International Conference on (Conf. Publ. No. 444)*, Banff, Canada, pp. 336-340.

[19] B. Akin, S. B. Ozturk, H. A. Toliyat, and M. Rayner, (2009) "DSP-Based Sensorless Electric Motor Fault-Diagnosis Tools for Electric and Hybrid Electric Vehicle Powertrain Applications," *Vehicular Technology, IEEE Transactions on,* vol. 58, pp. 2679-2688.

[20] L. A. Pereira and D. da Silva Gazzana, (2004) "Rotor broken bar detection and diagnosis in induction motors using stator current signature analysis and fuzzy logic," in *Industrial Electronics Society, 2004. IECON 2004. 30th Annual Conference of IEEE*, Busan, South Korea, pp. 3019-3024 Vol. 3.

[21] D. Matic, F. Kulic, V. Climente-Alarcon, and R. Puche-Panadero, (2010) "Artificial neural networks broken rotor bars induction motor fault detection," in *Neural Network Applications in Electrical Engineering (NEUREL), 2010 10th Symposium on*, Belgrade, Serbia, pp. 49-53.

[22] K. M. Goh, H. L. Chan, S. H. Ong, W. P. Moh, To, x, D. ws, and K. V. Ling, (2010) "Wireless GMR Sensor Node for Vibration Monitoring," in *Industrial Electronics and Applications (ICIEA), 2010 the 5th IEEE Conference on*, Taichung, Taiwan, pp. 23-28.

[23] S. Korkua, H. Jain, W.-J. Lee, and C. Kwan, (2010) "Wireless health monitoring system for vibration detection of induction motors," in *Industrial and Commercial Power Systems Technical Conference (I&CPS), 2010 IEEE*, Tallahassee, USA, pp. 1-6.

[24] M. Makowski, P. Pietrzak, B. Pekoslawski, and A. Napieralski, (2010) "Measurement synchronization in the vibration diagnostic system of high power electric machines," in *Mixed Design of Integrated Circuits and Systems (MIXDES), 2010 Proceedings of the 17th International Conference*, Warsaw, Poland, pp. 566-569.

[25] M. Kovacic, M. Vražic, and I. Gašparac, (2010) "Bluetooth wireless communication and 1-wire digital temperature sensors in synchronous machine rotor temperature measurement," in *Power Electronics and Motion Control Conference (EPE/PEMC), 2010 14th International*,

Ohrid, Bulgaria, pp. T7-25-T7-28.

[26]   T. Jager, P. Sulzberger, K. Wulff, and L. M. Reindl, (2009) "Integrated low-power RFID-S-system for online temperature and high-resolution displacement monitoring on high speed spindle rotors," in *Wireless Sensing, Local Positioning, and RFID, 2009. IMWS 2009. IEEE MTT-S International Microwave Workshop on*, Cavtat, Croatia, pp. 1-4.

[27]   X. Xin, V. Sundararajan, and W. P. Brithinee, (2007) "The application of wireless sensor networks for condition monitoring in three-phase induction motors," in *Electrical Insulation Conference and Electrical Manufacturing Expo, 2007*, Nashville, USA, pp. 445-448.

[28]   H. Guo and L. Ruan, (2011) "Wireless power supply RF temperature monitoring system applied to the rotor of generators," in *Electronics, Communications and Control (ICECC), 2011 International Conference on*, Ningbo, China, pp. 593-596.

[29]   H. Hafezi and A. Jalilian, (2006) "Design and Construction of Induction Motor Thermal Monitoring System," in *Universities Power Engineering Conference, 2006. UPEC '06. Proceedings of the 41st International*, Newcastle-upon-Tyne, UK, pp. 674-678.

[30]   M. Ganchev, B. Kubicek, and H. Kappeler, (2010) "Rotor temperature monitoring system," in *Electrical Machines (ICEM), 2010 XIX International Conference on*, Rome, Italy, pp. 1-5.

[31]   M. Wurfel and W. Hofmann, (2005) "Monitoring system for the diagnostic of sparking in doubly-fed induction generators," in *Power Electronics and Applications, 2005 European Conference on*, Dresden, Germany, pp. 10 pp.-P.10.

[32]   V. Sarkimaki, R. Tiainen, T. Lindh, and J. Ahola, (2006) "Applicability of ZigBee technology to electric motor rotor measurements," in *Power Electronics, Electrical Drives, Automation and Motion, 2006. SPEEDAM 2006. International Symposium on*, Taormina, Italy, pp. 137-141.

[33]   F. D. Smith and K. L. Hanson, (1975) "Rotor Protection of Large Motors by Use of Direct Temperature Monitoring," *Industry Applications, IEEE Transactions on,* vol. IA-11, pp. 340-343.

[34]   P. Zheng, S. Pan, and Y. Li, (2005) "The research on the network optical fiber sensor of the surface temperature measurement for a large rotor based on IEEE1451.2," in *Electrical Machines and Systems, 2005. ICEMS 2005. Proceedings of the Eighth International Conference on*, Nanjing, China, pp. 2434-2436 Vol. 3.

[35]   H. Guo and L. Ruan, (2011) "Design of wireless powered RF temperature monitoring system applied to the rotor of generators," in *Electrical Machines and Systems (ICEMS), 2011 International Conference on*, Ningbo, China, pp. 1-4.

[36]   J. Wassermann, M. Schneeberger, and F. Höftberger, (2005) "Wireless Data Transfer System for Rotating Machinery - Very Robust Against Electromagnetic Interference," presented at the *1st International Conference on Sensing Technology*, Palmerston North, New Zealand.

[37]   M. J. McCullagh, P. P. Smyth, D. R. Wisely, and P. L. Eardley, (1993) "Optical wireless LANs: applications and systems," in *Cordless Computing - Systems and User Experience, IEE Colloquium on*, London, UK, pp. 8/1-8/3.

[38]   C. Singh, J. John, Y. N. Singh, and K. K. Tripathi, (2005) "Design aspects of high-performance indoor optical wireless transceivers [LAN applications]," in *Personal Wireless Communications, 2005. ICPWC 2005. 2005 IEEE International Conference on*, New Delhi, India, pp. 14-18.

[39]   U. N. Griner and S. Arnon, (2006) "Multiuser diffuse indoor wireless infrared communication

using equalized synchronous CDMA," *Communications, IEEE Transactions on,* vol. 54, pp. 1654-1662.

[40] Q. Jiang, M. Kavehrad, M. R. Pakravan, and M. Tai, (1995) "Wideband optical propagation measurement system for characterization of indoor wireless infrared channels," in *Communications, 1995. ICC '95 Seattle, 'Gateway to Globalization', 1995 IEEE International Conference on*, Seattle, USA, pp. 1173-1176 vol.2.

[41] A. Boucouvalas, (2003) "Editorial: Optical wireless communications," *Optoelectronics, IEE Proceedings -,* vol. 150, pp. 425-426.

[42] A. Mahdy and J. S. Deogun, (2004) "Wireless optical communications: a survey," in *Wireless Communications and Networking Conference, 2004. WCNC. 2004 IEEE*, Atlanta, USA, pp. 2399-2404 Vol.4.

[43] H. Oomori, M. Shiozaki, and H. Kurashima, (2009) "Development of a practical electro-magnetic interference (EMI) simulation in high speed optical transceivers," in *Electronic Components and Technology Conference, 2009. ECTC 2009. 59th*, San Diego, USA, pp. 1908-1913.

[44] J. Chilo, C. Karlsson, P. Angskog, and P. Stenumgaard, (2009) "EMI disruptive effect on wireless industrial communication systems in a paper plant," in *Electromagnetic Compatibility, 2009. EMC 2009. IEEE International Symposium on*, Austin, USA, pp. 221-224.

[45] Z. Lei, M. Jin, P. Qijun, and M. WeiMing, (2010) "Analysis and Diagnosis of Conducted EMI Generated by Automatic Voltage Regulator (AVR) System in Synchronous Generator," in *Power and Energy Engineering Conference (APPEEC), 2010 Asia-Pacific*, Chengdu, China, pp. 1-4.

[46] S. Ogasawara, H. Ayano, and H. Akagi, (1997) "Measurement and reduction of EMI radiated by a PWM inverter-fed AC motor drive system," *Industry Applications, IEEE Transactions on,* vol. 33, pp. 1019-1026.

[47] S. Loyka, (2004) "Electromagnetic interference in wireless communications: behavioral-level simulation approach," in *Vehicular Technology Conference, 2004. VTC2004-Fall. 2004 IEEE 60th*, Los Angeles, USA, pp. 3945-3949 Vol. 6.

[48] D. Kawase, H. Oomori, M. Shiozaki, and H. Kurashima, (2011) "EMI suppression of 10Gbit/s optical transceiver by using EBG structure," in *Electromagnetic Compatibility (EMC), 2011 IEEE International Symposium on*, Rome, Italy, pp. 33-38.

[49] D. J. T. Siyambalapitiya, P. G. McLaren, and P. P. Acarnley, (1987) "A Rotor Condition Monitor for Squirrel-Cage Induction Machines," *Industry Applications, IEEE Transactions on,* vol. IA-23, pp. 334-340.

[50] N. Chand, T. DeLuck, J. H. Andrew, B. M. Eteson, T. M. Daniel, and R. T. Carlson, (2010) "Compact low-cost non-RF communication solutions for unmanned ground vehicles," in *MILITARY COMMUNICATIONS CONFERENCE, 2010 - MILCOM 2010*, San Jose, USA, pp. 1577-1582.

[51] S. Bloom, E. Korevaar, J. Schuster, and H. Willebrand, (2003) "Understanding the performance of free-space optics [Invited]," *J. Opt. Netw.,* vol. 2, pp. 178-200.

[52] M. Gebhart, E. Leitgeb, and J. Bregenzer, (2003) "Atmospheric effects on optical wireless links," in *Telecommunications, 2003. ConTEL 2003. Proceedings of the 7th International Conference on*, Zagreb, Croatia, pp. 395-401 vol.2.

[53] A. Mihaescu and P. Besnard, (2010) "Indoor wireless optical communications," in *Communications (COMM), 2010 8th International Conference on*, Bucharest, Romania, pp. 359-362.

[54] V. Jungnickel, V. Pohl, S. Nonnig, and C. von Helmolt, (2002) "A physical model of the wireless infrared communication channel," *Selected Areas in Communications, IEEE Journal on,* vol. 20, pp. 631-640.

[55] M. V. Lazovic and P. S. Matavulj, (2005) "SPICE Model of P-i-N Photodiode for Heaveside excitation," in *Computer as a Tool, 2005. EUROCON 2005.The International Conference on*, Belgrade, Serbia, pp. 875-878.

[56] M. V. Lazović, P. S. Matavulj, and J. B. Radunović, (2004) "Equivalent electric circuit of the P-i-N photodiode for the pulse incident excitation," *Microwave and Optical Technology Letters,* vol. 41, pp. 468-471.

[57] C. K. Sun, P. K. L. Yu, C. T. Chang, and D. J. Albares, (1992) "Simulation and interpretation of fast rise time light-activated p-i-n diode switches," *Electron Devices, IEEE Transactions on,* vol. 39, pp. 2240-2247.

[58] P. S. Matavulj, D. M. Gvozdic, and J. B. Radunovic, (1997) "The influence of nonstationary carrier transport on the bandwidth of p-i-n photodiode," *Lightwave Technology, Journal of,* vol. 15, pp. 2270-2277.

[59] P. S. Matavulj, D. M. Gvozdic, and J. B. Radunovic, (1997) "Analysis of the linear and nonlinear time response of a P-i-N photodiode by a two-valley model," in *Microelectronics, 1997. Proceedings., 1997 21st International Conference on*, Nis, Yugoslavia, pp. 331-334 vol.1.

[60] Z. Djuríc and B. Radjenović, (1983) "Rise time of silicon p-n-p photodiodes," *Solid-State Electronics,* vol. 26, pp. 1143-1149.

[61] G. George and J. P. Krusius, (1994) "Transient response of high-speed p-i-n photodiodes including diffusion effects," *Solid-State Electronics,* vol. 37, pp. 1841-1847.

[62] J. A. Connelly, (1993) *Low-Noise Electronic System Design*. New York: John Wiley & Sons.

[63] N. Kularatna, (2008) *Electronic Circuit Design: From Concept to Implementation* Boca Raton: CRC Press.

[64] W. M. Leach, Jr., (1994) "Fundamentals of low-noise analog circuit design," *Proceedings of the IEEE,* vol. 82, pp. 1515-1538.

[65] H. Chia-Lu, (1995) "Calculating the performance of optical communication systems with modal noise by saddlepoint method," *Lightwave Technology, Journal of,* vol. 13, pp. 1820-1825.

[66] G. Einarsson, (1996) *Principles of Lightwave Communications* Chichester: John Wiley & Sons.

[67] L. Weiss and W. Mathis, (1999) "Noise equivalent circuit for nonlinear resistors," in *Circuits and Systems, 1999. ISCAS '99. Proceedings of the 1999 IEEE International Symposium on*, Orlando, USA, pp. 314-317 vol.5.

[68] S. Joon-Jea, K. Guen-Soon, and K. Suki, (2003) "A transient noise model for frequency-dependent noise sources," *Computer-Aided Design of Integrated Circuits and Systems, IEEE Transactions on,* vol. 22, pp. 1097-1104.

[69] D. J. Santos and F. J. Fraile-Pelaez, (1999) "Pulse normalisation in optical receiver shot-noise performance," *Optoelectronics, IEE Proceedings -,* vol. 146, pp. 201-203.

[70] X. Jiansheng, D. Yisong, and D. Abbott, (2000) "A complete operational amplifier noise model: analysis and measurement of correlation coefficient," *Circuits and Systems I: Fundamental Theory and Applications, IEEE Transactions on,* vol. 47, pp. 420-424.

[71] G. Giusi, F. Crupi, C. Pace, and P. Magnone, (2009) "Full Model and Characterization of Noise in Operational Amplifier," *Circuits and Systems I: Regular Papers, IEEE Transactions on,* vol. 56, pp. 97-102.

[72] V. Vasudevan, (2004) "A simple technique to evaluate the noise spectral density in operational amplifier based circuits using the adjoint network theory," *Circuits and Systems I: Regular Papers, IEEE Transactions on,* vol. 51, pp. 2175-2178.

[73] E. N. Gilbert and H. O. Pollak, (1960) "Amplitude Distrubtion of Shot Noise," *The Bell System Technical Journal,* vol. 39, pp. 333-350.

[74] R. G. W. Brown and J. P. Dakin, Eds., (2006) *Handbook of Optoelectronics.* New York: Taylor & Francis.

[75] G. P. Agrawal, (2002) *Fiber-Optic Communication Systems.* New York: Wiley-Interscience.

[76] S. S. Walklin and G. D. Cormack, (1993) "Digital optical receiver output voltage probability distribution including gain statistics of an avalanche photodiode," in *Communications, Computers and Signal Processing, 1993., IEEE Pacific Rim Conference on*, pp. 761-764 vol.2.

[77] B. K. Ng, J. P. R. David, R. C. Tozer, M. Hopkinson, G. Hill, and G. J. Rees, (2002) "Excess noise characteristics of $Al_{0.8}Ga_{0.2}As$ avalanche photodiodes," *Photonics Technology Letters, IEEE,* vol. 14, pp. 522-524.

[78] M. Teich, K. Matsuo, and B. Saleh, (1986) "Excess noise factors for conventional and superlattice avalanche photodiodes and photomultiplier tubes," *Quantum Electronics, IEEE Journal of,* vol. 22, pp. 1184-1193.

[79] P. Wright, K. B. Ozanyan, S. J. Carey, and H. McCann, (2005) "Design of high-performance photodiode receivers for optical tomography," *Sensors Journal, IEEE,* vol. 5, pp. 281-288.

[80] R. Green, M. Higgins, H. Joshi, and M. Leeson, (2008) "Bandwidth extension for optical wireless receiver-amplifiers," in *Transparent Optical Networks, 2008. ICTON 2008. 10th Anniversary International Conference on*, Athens, Greece, pp. 201-204.

[81] F. Centurelli, R. Luzzi, M. Olivieri, and A. Trifiletti, (2002) "A bootstrap technique for wideband amplifiers," *Circuits and Systems I: Fundamental Theory and Applications, IEEE Transactions on,* vol. 49, pp. 1474-1480.

[82] P. Khoman and D. A. Johns, (1999) "A CMOS optical preamplifier for wireless infrared communications," *Circuits and Systems II: Analog and Digital Signal Processing, IEEE Transactions on,* vol. 46, pp. 852-859.

[83] J. G. Graeme, (1995) *Photodiode Amplifiers: OP AMP Solutions* Boston: McGraw-Hill.

[84] D. V. Bugg, (2006) *Electronics Circuits, Amplifiers and Gates, Second Edition.* New York: Taylor & Francis.

[85] B. Zand, K. Phang, and D. A. Johns, (1999) "Transimpedance amplifier with differential photodiode current sensing," in *Circuits and Systems, 1999. ISCAS '99. Proceedings of the 1999 IEEE International Symposium on*, Orlando, USA, pp. 624-627 vol.2.

[86] J. Smith, (1986) *Modern Communication Circuits.* New York: McGraw-Hill Higher Education.

[87] L. Anbang, A. Jianping, and W. Aihua, (2010) "Design of a Digital Automatic Gain Control with Backward Difference Transformation," in *Wireless Communications Networking and*

Mobile Computing (WiCOM), 2010 6th International Conference on, Chengdu, pp. 1-4.

[88] J. M. Khoury, (1998) "On the design of constant settling time AGC circuits," *Circuits and Systems II: Analog and Digital Signal Processing, IEEE Transactions on,* vol. 45, pp. 283-294.

[89] D. Zhang, Y. Liu, H. Jiang, S. Li, and B. Tang, (2008) "Study and design on automatic gain control circuit for WCDMA repeater uplink system," in *Microwave and Millimeter Wave Technology, 2008. ICMMT 2008. International Conference on*, Nanjing, pp. 1976-1979.

[90] E. J. Tacconi and C. F. Christiansen, (1993) "A wide range and high speed automatic gain control," in *Particle Accelerator Conference, 1993., Proceedings of the 1993*, Washington, DC, USA, pp. 2139-2141 vol.3.

[91] L. Chien-Chih, S. Muh-Tain, and W. Chorng-Kuang, (2002) "A dual-loop automatic gain control for infrared communication system," in *ASIC, 2002. Proceedings. 2002 IEEE Asia-Pacific Conference on*, Taipei, Taiwan, pp. 125-128.

[92] R. Ramirez-Iniguez, S. M. Idrus, and Z. Sun, (2008) *Optical Wireless Communications*. Boca Raton: Taylor & Francis Group, CRC Press.

[93] C. Ta-Shing and M. Gans, (1987) "High speed infrared local wireless communication," *Communications Magazine, IEEE,* vol. 25, pp. 4-10.

[94] J. M. Kahn, J. R. Barry, W. J. Krause, M. D. Audeh, J. B. Carruthers, G. W. Marsh, E. A. Lee, and D. G. Messerschmitt, (1992) "High-speed non-directional infrared communication for wireless local-area networks," in *Signals, Systems and Computers, 1992. 1992 Conference Record of The Twenty-Sixth Asilomar Conference on*, Pacific Grove, USA, pp. 83-87.

[95] N. D. Chatzidiamantis, A. S. Lioumpas, G. K. Karagiannidis, and S. Arnon, (2010) "Optical Wireless Communications with Adaptive Subcarrier PSK Intensity Modulation," in *GLOBECOM 2010, 2010 IEEE Global Telecommunications Conference*, Miami, USA, pp. 1-6.

[96] Q. Liu and Q. Lu, (2005) "Subcarrier PSK intensity modulation for optical wireless communications through turbulent atmospheric channel," in *Communications, 2005. ICC 2005. 2005 IEEE International Conference on*, Seoul, Korea, pp. 1761-1765 Vol. 3.

[97] S. Meihong, Y. Xinsheng, and Z. Fengli, (2009) "The Evaluation of Modulation Techniques for Underwater Wireless Optical Communications," in *Communication Software and Networks, 2009. ICCSN '09. International Conference on*, Macau, China, pp. 138-142.

[98] J. Armstrong, (2009) "OFDM for Optical Communications," *Lightwave Technology, Journal of,* vol. 27, pp. 189-204.

[99] T. A. Gulliver, (2006) "Modulation and Coding Techniques for Infrared Wireless Local Area Networks," in *Computer Engineering and Systems, The 2006 International Conference on*, Cairo, Egypt, pp. II-1-II-1.

[100] V. Vitsas, P. Barker, and A. C. Boucouvalas, (2003) "IrDA infrared wireless communications: protocol throughput optimization," *Wireless Communications, IEEE,* vol. 10, pp. 22-29.

[101] Z. Ghassemlooy, A. R. Hayes, N. L. Seed, and E. D. Kaluarachchi, (1998) "Digital pulse interval modulation for optical communications," *Communications Magazine, IEEE,* vol. 36, pp. 95-99.

[102] H. Wang, X. Sun, X. Sun, T. Zhang, and Y. Zhu, (2006) "Performance of current digital pulse modulation schemes for optical wireless communications," in *Wireless, Mobile and Multimedia Networks, 2006 IET International Conference on*, Hangzhou, China, pp. 1-4.

[103]   N. Azzam, M. H. Aly, and A. K. AboulSeoud, (2009) "Bandwidth and power efficiency of various PPM schemes for indoor wireless optical communications," in *Radio Science Conference, 2009. NRSC 2009. National*, New Cairo, Egypt, pp. 1-11.

[104]   T. Ohtsuki, I. Sasase, and S. Mori, (1994) "Differential overlapping pulse position modulation in optical direct-detection channel," in *Communications, 1994. ICC '94, SUPERCOMM/ICC '94, Conference Record, 'Serving Humanity Through Communications.' IEEE International Conference on*, New Orleans, USA, pp. 680-684 vol.2.

[105]   A.-p. Huang, Y.-Y. Fan, Y.-K. Liu, M. Jia, B. Bai, and Q.-G. Tan, (2009) "A differential pulse position width modulation for optical wireless communication," in *Industrial Electronics and Applications, 2009. ICIEA 2009. 4th IEEE Conference on*, Xi'an, China, pp. 1773-1776.

[106]   G. A. Mahdiraji and E. Zahedi, (2006) "Comparison of Selected Digital Modulation Schemes (OOK, PPM and DPIM) for Wireless Optical Communications," in *Research and Development, 2006. SCOReD 2006. 4th Student Conference on*, Selangor, Malaysia, pp. 5-10.

[107]   Z. Jinlong, (2000) "Modulation analysis for outdoors applications of optical wireless communications," in *Communication Technology Proceedings, 2000. WCC - ICCT 2000. International Conference on*, Beijing, China, pp. 1483-1487 vol.2.

[108]   P. Hyuncheol and J. R. Barry, (1995) "Modulation analysis for wireless infrared communications," in *Communications, 1995. ICC '95 Seattle, 'Gateway to Globalization', 1995 IEEE International Conference on*, Seattle, USA, pp. 1182-1186 vol.2.

[109]   Infrared-Data-Association. ( ) *About IrDA - IrDA Background*. [cited 09/12/2011].Available from: http://www.irda.org/displaycommon.cfm?an=1&subarticlenbr=25

[110]   S. Williams, (2000) "IrDA: past, present and future," *Personal Communications, IEEE,* vol. 7, pp. 11-19.

[111]   C. D. Knutson and J. M. Brown, (2004) *IrDA principles and protocols: The IrDA Library* vol. 1. Salem: MCL Press.

[112]   I. Millar, M. Beale, B. J. Donoghue, K. W. Lindstrom, and S. Williams. The IrDA Standards for High-Speed Infrared Communications [Online]. Available from: http://www.hpl.hp.com/hpjournal/98feb/feb98a2.pdf

[113]   M. G. Robertson, S. V. Hansen, F. E. Sorenson, and C. D. Knutson, (2001) "Modeling IrDA performance: the effect of IrLAP negotiation parameters on throughput," in *Computer Communications and Networks, 2001. Proceedings. Tenth International Conference on*, Scottsdale, USA, pp. 122-127.

[114]   P. Barker and A. C. Boucouvalas, (1998) "Performance modeling of the IrDA protocol for infrared wireless communications," *Communications Magazine, IEEE,* vol. 36, pp. 113-117.

[115]   P. Barker, A. C. Boucouvalas, and V. Vitsas, (2000) "Performance modelling of the IrDA infrared wireless communications protocol," *International Journal of Communication Systems,* vol. 13, pp. 589-604.

[116]   Texas-Instruments. (2007) *Implementing IrDA With The MSP430*. [cited 13/11/2011].Available from: http://www.ti.com/lit/an/slaa202a/slaa202a.pdf

[117]   Y. Kotsuka, K. Orii, H. Kojima, K. Kamogawa, and M. Tanaka, (1999) "New Wireless Thermometer for RF and Microwave Thermal Therapy Using an MMIC in an Si BJT VCO Type," *IEEE Transaction on Microwave Theory and Techniques,* vol. 47, pp. 2630-2635.

[118]   Y. Liu, J. Xu, X. Zhang, and Y. Dai, (1999) "The extraction of the signals from the transducers in the vehicle under the condition of strong electromagnetic interference," in *Proceedings of*

the IEEE International Vehicle Electronics Conference, Changchun, China, pp. 327-330.

[119]   G. UMANESAN and E. FUJIWARA, (2000) "Single byte error control codes with double bit within a block error correcting capability for semiconductor memory systems," *IEEE International Symposium on   Defect and Fault-Tolerance in VLSI Systems,* pp. 25-27.

[120]   P. Butler, R. Guidotti, L. Moya, and F. Reinhardt, (2002) "High power thermal battery development," presented at the *Conference Record of the Twenty-Fifth International   Power Modulator Symposium, 2002 and 2002 High-Voltage Workshop*, Hollywood, USA.

[121]   S. Kauffman and G. Chagnon, (1992) "Thermal battery for aircraft emergency power," presented at the *IEEE 35th International Power Sources Symposium*, Cherry Hill, USA.

[122]   Micropelt-GmbH. (2008) *Thin Film Thermogenerators and Sensing Devices*. [cited 14/12/2011].Available from: http://www.micropelt.com/down/datasheet_mpg_d651_d751.pdf

[123]   A. L. Rockwood, (1984) "Relationship of thermoelectricity to electronic entropy," *PHYSICAL REVIEW A,* vol. 30, pp. 2843-2844.

[124]   D. M. Rowe, Ed., (2006) *Thermoelectrics Handbook: Macro to Nano*. Boca Raton: CRC Press, Taylor & Francis Group.

[125]   Micropelt-GmbH. (2008) *Ultra-small Pelter Cooler for Fiber Optics and Sensor application*. [cited 14/12/2011].Available from: http://www.micropelt.com/down/datasheet_mpc_d303.pdf

[126]   T. Itoh, T. Muto, and K. Kitagawa, (2006) "Performance of Segmented Thermoelectric Elements Fabricated by Simultaneous Sintering Method," presented at the *IEEE International Conference on Thermoelectrics*, Vienna, Austria.

[127]   J.-P. Fleurial, K. Johnson, J. Mondt, J. Sakamoto, J. Snyder, C.-K. Huang, R. Blair, G. Stapfer, T. Caillat, P. Frye, W. Determan, B. Heshmatpour, M. Brooks, and K. Tuttle, (2006) "Development of segmented thermoelectric multicouple converter technology," presented at the *IEEE Aerospace Conference*, Big Sky, USA.

[128]   H. Xiao, X. Gou, and C. Yang, (2008) "Simulation analysis on thermoelectric generator system performance," presented at the *Asia Simulation Conference - 7th International Conference on System Simulation and Scientific Computing*, Beijing, China.

[129]   M. S. El-Genk and H. H. Saber, (2002) "Predictions of segmented thermoelectric unicouples performance at hot temperatures less than 873 K and cold temperature of 298 K," in *Thermoelectrics, 2002. Proceedings ICT '02. Twenty-First International Conference on*, Long Beach, USA, pp. 408-411.

[130]   P. Khluabwannarat, C. Thammarat, S. Tadsuan, and B. Suechoey, (2007) "The result analysis of the electrical power and temperature of 3-phase induction motor supplied by the PWM inverter," in *International Power Engineering Conference*, Singapore.

[131]   H. Xi, L. Luo, and G. Fraiss, (2007) "Development and applications of solar-based thermoelectric technologies," *Renewable and Sustainable Energy Reviews,* vol. 11, pp. 923–936.

[132]   T. S. Ursell and G. J. Snyder, (2002) "Compatibility of segmented thermoelectric generators," in *Thermoelectrics, 2002. Proceedings ICT '02. Twenty-First International Conference on*, Long Beach, USA, pp. 412-417.

[133]   S. Baglio, S. Gagliano, D. Neri, N. Savalli, and G. Tina, (2008) "Optimal design of Photovoltaic systems for Wireless Sensor Networks," *IEEE International Symposium on Industrial Electronics,* pp. 2108 - 2113.

[134]   G. TREUSCH, T. KOENNING, and B. SHELEF. (2008) High-power Diode Lasers Boost

Powerbeaming Competition. *Laser Focus World*.   pp. 75-76.

[135]   V. Andreev, V. Khvostikov, V. Kalinovsky, V. Lantratov, V. Grilikhes, V. Rumyantsev, M. Shvarts, V. Fokanov, and A. Pavlov, (2003) "High current density GaAs and GaSb photovoltaic cells for laser power beaming," in *3rd World Conference on Photovoltaic Energy Conversion*, Osaka, Japan, pp. 761 - 764

[136]   J. Katz, (1985) "Power conversion efficiency of semiconductor injection lasers and laser arrays in CW operation," *IEEE Journal of Quantum Electronics,* vol. 21, pp. 1854 - 1857

[137]   G. Yan, D. Ye, P. Zan, K. Wang, and G. Ma, (2007) "Micro-Robot for Endoscope Based on Wireless Power Transfer," in *International Conference on Mechatronics and Automation*, Harbin, China, pp. 3577-3581.

[138]   G. Wang, W. Liu, M. Sivaprakasam, J. D. Weiland, and M. S. Humayun, (2005) "High Efficiency Wireless Power Transmission with Digitally Configurable Stimulation Voltage for Retinal Prosthesis," in *2nd International IEEE EMBS Conference on Neural Engineering*, Arlington, Virginia.

[139]   K. Fotopoulou and B. W. Flynn, (2006) "Wireless Powering of Implanted Sensors using RF Inductive Coupling," in *5th IEEE Conference on Sensors*, Daegu, South Korea, pp. 765 - 768.

[140]   C. M. Zierhofer and E. S. Hochmair, (1990) "High-efficiency coupling-insensitive transcutaneous power and data transmission via an inductive link," *Biomedical Engineering, IEEE Transactions on,* vol. 37, pp. 716-722.

[141]   Z. Wenhao, P. Xitian, Z. Xiaolin, L. Hongying, X. Xiao, and P. Chenglin, (2008) "A wireless energy transmission system based on electromagnetism induction for remote controlled capsule," in *Automation Congress, 2008. WAC 2008. World*, Hawaii, USA, pp. 1-4.

[142]   J. G. Webster, Ed., (1999) *Measurement, Instrumentation, and Sensors Handbook* (Electrical Engineering Handbook I). Boca Raton: CRC Press LLC.

[143]   A. Pohl, F. Seifert, L. Reindl, G. Scholl, T. Ostertag, and W. Pietsch, (1994) "Radio signals for SAW ID tags and sensors in strong electromagnetic interference," in *Ultrasonics Symposium, 1994. Proceedings., 1994 IEEE*, Cannes, France, pp. 195-198 vol.1.

[144]   M. Taslakov and V. Simeonov, (2005) "System for a remote readout of multiple passive sensors using 31 THz quantum cascade laser," in *Frequency Control Symposium and Exposition, 2005. Proceedings of the 2005 IEEE International*, Vancouver, USA, pp. 897-901.

[145]   P. J. Winzer and R. J. Essiambre, (2006) "Advanced Optical Modulation Formats," *Proceedings of the IEEE,* vol. 94, pp. 952-985.

[146]   D. C. C. Norman, D. J. Webb, and R. D. Pechstedt, (2005) "Interferometric sensor interrogation using an arrayed waveguide grating," *Photonics Technology Letters, IEEE,* vol. 17, pp. 172-174.

[147]   M. Jimenez and M. Nunez-Arzuaga, (2004) "Implementing Irda on the Msp430: a project development under the undergraduate research/co-op education model," in *Frontiers in Education, 2004. FIE 2004. 34th Annual*, pp. S1B/6-S1B/9 Vol. 3.

[148]   Texas-Instruments. (1999) *MSP430 IrDA SIR Encoder/Decoder Application Report*. [cited 2011/13/11].Available from: http://www.ti.com/lit/an/slaa044/slaa044.pdf

[149]   Y. Zhang, (2010) "Design of Low-Power Wireless Communication System Based on MSP430 and nRF2401," in *Measuring Technology and Mechatronics Automation (ICMTMA), 2010 International Conference on*, Changsha, China, pp. 1008-1010.

[150]   H. Sheng-Ta, (2011) "RFID medical information system: A system implementation on

MSP430 platform," in *Consumer Electronics, Communications and Networks (CECNet), 2011 International Conference on*, Xianning, China, pp. 1-4.

[151]   Z. Hou and G. Gu, (2008) "Wireless rotor temperature measurement system based on MSP430 and nRF401," in *Electrical Machines and Systems, 2008. ICEMS 2008. International Conference on*, Wuhan, China, pp. 858-861.

[152]   Micropelt-GmbH. (2009) *TE-Power NODE. Self-Sufficient Wireless Sensor System Thermoharvesting Explorer*.Available from:
http://www.micropelt.com/down/datasheet_te_power_node.pdf

[153]   R. Otte, L. P. d. Jong, and A. H.M, (1999) *Low-power wireless infrared communications* Boston: Kluwer Academic Publishers.

[154]   H. Kressel, Ed., (1980) *Semiconductor devices for optical communication*. Berlin: Springer-Verlag.

[155]   OSRAM-Opto-Semiconductors-GmbH. (2010) *High Power Infrared Emitter (850 nm) SFH 4550*.Available from:
http://catalog.osram-os.com/catalogue/catalogue.do;jsessionid=5B462E4737056132D5A6231
AF692899A?act=downloadFile&favOid=020000030000cb8a000100b6

[156]   H. Uno, K. Kumatani, H. Okuhara, I. Shirakawa, and T. Chiba, (1997) "Low power architecture for high speed infrared wireless communication system," in *Low Power Electronics and Design, 1997. Proceedings., 1997 International Symposium on*, Monterey, USA, pp. 255-258.

[157]   B. Epple, (2010) "Simplified Channel Model for Simulation of Free-Space Optical Communications," *Optical Communications and Networking, IEEE/OSA Journal of,* vol. 2, pp. 293-304.

[158]   O. Gonzalez, S. Rodriguez, R. Perez-Jimenez, B. R. Mendoza, and A. Ayala, (2005) "Error analysis of the simulated impulse response on indoor wireless optical channels using a Monte Carlo-based ray-tracing algorithm," *Communications, IEEE Transactions on,* vol. 53, pp. 124-130.

[159]   C. Helstrom, (1979) "Performance Analysis of Optical Receivers by the Saddlepoint Approximation," *Communications, IEEE Transactions on,* vol. 27, pp. 186-191.

[160]   C. W. Helstrom, (1988) "Computing the performance of optical receivers with avalanche diode detectors," *Communications, IEEE Transactions on,* vol. 36, pp. 61-66.

[161]   M. S. Leeson, (2000) "Performance analysis of direct detection spectrally sliced receivers using Fabry-Perot filters," *Lightwave Technology, Journal of,* vol. 18, pp. 13-25.

[162]   T. Ohtsuki, I. Sasase, and S. Mori, (1994) "Trellis coded overlapping multi-pulse pulse position modulation in optical direct detection channel," in *Communications, 1994. ICC '94, SUPERCOMM/ICC '94, Conference Record, 'Serving Humanity Through Communications.' IEEE International Conference on*, New Orleans, USA, pp. 675-679.

[163]   R. Y. Chen and C. Ming-Jen, (2009) "A CMOS Variable-gain Fully-differential Transimpedance Amplifier for Multimedia Data Links," in *Intelligent Information Hiding and Multimedia Signal Processing, 2009. IIH-MSP '09. Fifth International Conference on*, Kyoto, Japan, pp. 402-405.

[164]   F. Normandin, M. Sawan, and J. Faubert, (2004) "Front-end of a non-invasive wireless real-time brain imaging system based on near-infrared spectroreflectometry," in *Biomedical Circuits and Systems, 2004 IEEE International Workshop on*, Singapore, pp. S3/1-S1-4.

[165]   M. K. Achuthan and K. N. Bhat, (2007) *Fundamentals of Semiconductor Devices*. New Delhi: Tata McGraw-Hill Education.

[166]   Texas-Instruments. (2005) *High Speed Analog Design and Application Seminar*. [cited 12/14/2011].Available from: http://www.ti.com/lit/ml/slyp169/slyp169.pdf

[167]   Linear-Technology. (1997) *LT1328 - 4Mbps IrDA Infrared Receiver*. [cited 05/05/2012].Available from: http://cds.linear.com/docs/Datasheet/1328f.pdf

[168]   Linear-Technology. (2007) *LT1228 - 100MHz Current Feedback Amplifier with DC Gain Control*. [cited 10/09/2011].Available from: http://cds.linear.com/docs/Datasheet/1228fc.pdf

[169]   E. Nilsson and C. Svensson, (2011) "Envelope detector sensitivity and blocking characteristics," in *Circuit Theory and Design (ECCTD), 2011 20th European Conference on*, Linkoping, Sweden, pp. 773-776.

[170]   I. Bar-David and G. Kaplan, (1984) "Information rates of photon-limited overlapping pulse position modulation channels," *Information Theory, IEEE Transactions on,* vol. 30, pp. 455-464.

[171]   D. Jupeng, H. Zhitong, and J. Yuefeng, (2010) "Indoor white light wireless data transmission based on new generation environment-friendly solid state lighting," in *Wireless Communications, Networking and Information Security (WCNIS), 2010 IEEE International Conference on*, Beijing, China, pp. 87-91.

[172]   Texas-Instruments. (2009) *MSP430x43x, MSP430x43x1, MSP430x44x Mixed Signal Microcontroller* [cited 13/11/2011].Available from: http://www.ti.com/lit/ds/symlink/msp430f449.pdf

[173]   Texas-Instruments. (2011) *MSP430F241x, MSP430F261x Mixed Signal Microcontroller*. [cited 31/11/2011].Available from: http://www.ti.com/lit/ds/symlink/msp430f2418.pdf

[174]   Texas-Instruments. (2004) *MSP430x2xx Family User's Guide*. [cited 13/11/2011].Available from: http://www.ti.com/lit/ug/slau144h/slau144h.pdf

[175]   Texas-Instruments. (2010) *MSP430x4xx Family User's Guide*. [cited 13/11/2011].Available from: http://www.ti.com/lit/ug/slau056j/slau056j.pdf

[176]   C. Christopoulos, (2007) *Principles and Techniques of Electromagnetic Compatibility, Second Edition*. Boca Raton: CRC Press.

[177]   F. T. Ulaby, E. Michielssen, and U. Ravaioli, (2010) *Fundamentals of Applied Electromagnetics (6th Edition)*. Upper Saddle River: Pearson.

[178]   Comsol. (2008). *Comsol Multiphysics User's Guide*.

[179]   Comsol. (2008). *AC/DC Module User's Guide*.

[180]   Comsol. (2008). *Comsol Multiphysics Modeling Guide*.

[181]   S. S. Rao, (2005) *The Finite Element Method in Engineering*, 4 ed. Burlington: Elsevier Butterworth-Heinemann.

APPENDICES

Appendix I A More Precise Model of the IR Transceiver

The model described in section 3.1.2 assumes linear motions of the both DT and DR. In the case of Fig. 3.1.1 (a), the model is only valid on a comparatively large scale of geometry. A more precise model shown in Fig. A.1 considers the motions as rotations, taking account more of the geometry parameters in the analysis compared to that of Fig. 3.1.3.

Here φ and θ are redefined in the geometry of Fig. A.1 to larger extents. Since the axes of the optical channels on both directions are geometrically parallel, the radiation angle of the LED equals to the angle of the photodiode angular factor on the same device, they can be represented using one parameter. Thus, φ is both the radiation angle of the LED and $cos(\varphi)$ is the angular factor of the photodiode of DT, φ is then named the Eigen angle. θ is the Eigen angle of DR. What is more, the rotation radius of the optical transceiver on DT is R_{DT}, the distance between the rotation centre of DT and the optical transceiver of DR is R_{DR}. An assistant distance d_A is also introduced as indicated in the figure. Here the time that DT and DR are in opposition is defined as t_0, as a result, the directional angular separation of the transceivers can be explained as $\omega(t - t_0)$ and d_A becomes:

$$d_A = R_{DT}\ sin[\omega(t - t_0)] \tag{A.1}$$

And θ and φ are:

$$\theta = \tan^{-1}\left(\frac{R_{DR} - R_{DT}\cos[\omega(t - t_0)]}{d_A}\right) \tag{A.2}$$

$$= \tan^{-1}\left(\frac{R_{DR} - R_{DT}\cos[\omega(t - t_0)]}{R_{DT}\sin[\omega(t - t_0)]}\right)$$

$$\varphi = \theta + \omega(t - t_0)$$

$$= \tan^{-1}\left(\frac{R_{DR} - R_{DT}\cos[\omega(t - t_0)]}{R_{DT}\sin[\omega(t - t_0)]}\right) + \omega(t - t_0) \tag{A.3}$$

The distance between the two transceivers d is:

$$d = \frac{d_A}{\sin(\theta)}$$

$$= \frac{R_{DT}\sin[\omega(t - t_0)]}{\sin\left[\tan^{-1}\left(\frac{R_{DR} - R_{DT}\cos[\omega(t - t_0)]}{R_{DT}\sin[\omega(t - t_0)]}\right)\right]} \tag{A.4}$$

Recalling (3.1.1) to (3.1.4):

$$P_R = \frac{P_P A_r \cos(\theta)}{d^2} \tag{A.5}$$

$$P_P = \frac{n + 1}{2\pi} P_E \cos^n(\varphi) \tag{A.6}$$

In (A.5), if all parameters are replaced by those from (A.2) to (A.6), the photodiode received power on the channel from the LED on DT to the photodiode on DR becomes:

$$P_R = \frac{(n + 1)P_E A_r \cos^n(\varphi)\cos(\theta)}{2\pi d^2} \tag{A.7}$$

$$= (n + 1)P_E A_r$$

$$\cdot \frac{\cos^n \left[\tan^{-1} \left(\dfrac{R_{DR} - R_{DT} \cos[\omega(t - t_0)]}{R_{DT} \sin[\omega(t - t_0)]} \right) + \omega(t - t_0) \right]}{2\pi \left(\dfrac{R_{DT} \sin[\omega(t - t_0)]}{\sin \left[\tan^{-1} \left(\dfrac{R_{DR} - R_{DT} \cos[\omega(t - t_0)]}{R_{DT} \sin[\omega(t - t_0)]} \right) \right]} \right)^2}$$

$$\cdot \cos \left[\tan^{-1} \left(\frac{R_{DR} - R_{DT} \cos[\omega(t - t_0)]}{R_{DT} \sin[\omega(t - t_0)]} \right) \right]$$

Switching the positions of θ and φ in (A.6) will give the received power of the photodiode on DT. Since the beam of the LED is assumed to be a Lambertian radiation pattern, the received power depends more on the noumenal Eigen angle than the one of the other device. From (A.3), $\varphi > \theta$ in all the time except t_0, therefore the communication window is longer on the optical channel from DR to DT. From another point of view, the time for communication relies on the channel from the LED of DT to the photodiode of DR. Compared the geometry of Fig. A.1 to that of Fig. 3.1.3, D is:

$$D = R_{DR} - R_{DT} \tag{A.8}$$

If R_{DR} and R_{DT} is far longer than D, the effect of $\omega(t - t_0)$ becomes negligible as the difference in θ and φ, because the communication window is limited in a very short period around t_0, but the geometry in this case also produces a small CWR, which matches the assumption in chapter 3.
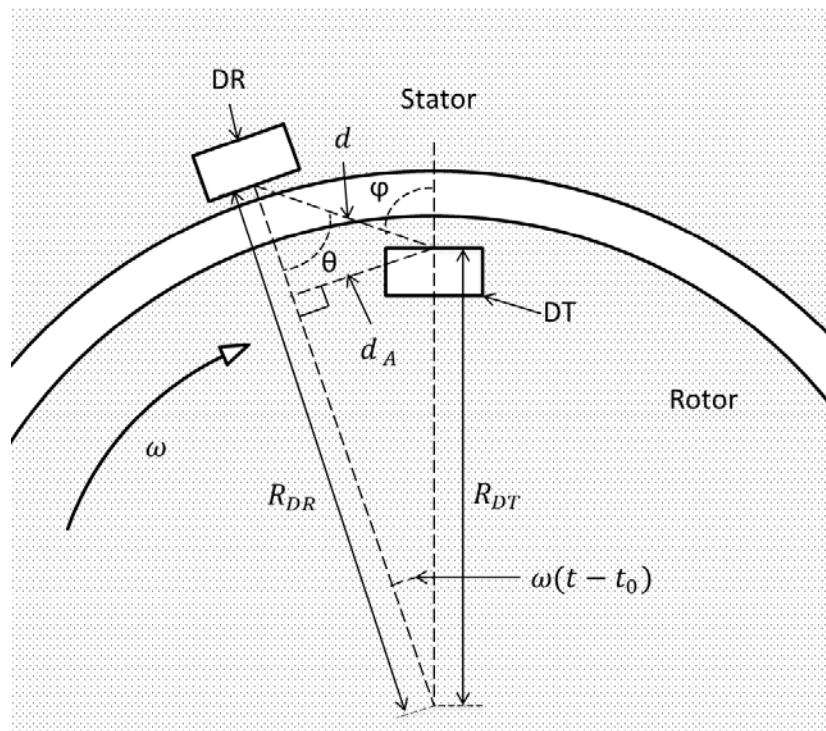
Fig. A.1 The precise model of IR transceiver

Appendix II Matlab Source code samples of Simulations in Chapter 3 and 4

Deriving bit capacities of different load resistors

```
t = -0.2e-4:1e-7:0.2e-4;
t0 = 0;
D1 = 0.2;
Pe = 25e-3;
Ar = 1e-6;
v = 10000;
n1 = 20;
n2 = 10;
heth = 0.89;
q = 1.602e-19;
kappa = 1.38e-23;
Tn = 300;
Rl = logspace(1,4,100);
Rl = Rl*5;
h = 6.6261e-34;
f = (3e8)/(850e-9);
T = 1/(10^5);
B = logspace(5,9,1000);
D = 0.1:0.01:1;
Cd = 11e-12;
Pe2 = logspace(-2,log10(0.05),500);


Pr1 = radipattern(n1,Pe,Ar,v,t,D1);


sigma = zeros(length(Rl),length(B));
for j = 1:length(Rl)
   for i = 1:length(B)
      sigma(j,i) = (Sn(j)/B(i))^0.5;
   end
end


syms s


temp_s = zeros(1,length(sigma));
temp_qmin = zeros(1,length(sigma));
time_limit = zeros (length(Rl),length(sigma));
```

```
BT = zeros(length(Rl),length(sigma));
cutoff = zeros(1,length(Rl));
for k = 1:length(Rl)
    if 1/(2*pi*Rl(k)*Cd)<B(length(B))
        for l = 1:length(B)
            if B(l)>(1/(2*pi*Rl(k)*Cd))
                if cutoff(k)==0
                cutoff(k) = l;
                end
            end
        end
    else
        cutoff(k) = length(B);
    end
    parfor i = 1:cutoff(k)
    for j= 1:length(t)
        temp_m = Pr1(j)*heth/(h*f*B(i));
        if temp_m >(sigma(k,i)*4.76)
            [temp_s(i),fval2] = fzero(@(s)
temp_m*exp(s)+s*((sigma(k,i))^2)-sigma(k,i)*4.76-1/s,1);
            temp_qmin(i) =
exp(temp_m*(exp(temp_s(i))-1)+(temp_s(i)^2)*((sigma(k,i))^2)/2-temp_s
(i)*sigma(k,i)*4.76-log(abs(temp_s(i)))))/((2*pi*(temp_m*exp(temp_s(i)
)+(sigma(k,i))^2+1/(temp_s(i)^2)))^0.5);
            if temp_qmin(i) < 10^(-6)
                if time_limit(k,i) == 0
                    time_limit(k,i) = abs(t(j))*2;
                    BT(k,i) = time_limit(k,i)* B(i);
                end
            end
        end
    end
    end
k
end
```


Deriving bit capacities with higher precision and calculating power

efficiency related parameters

```
%%%%%%%%%%%%%%%%%%%%%%%%%%%%%%%%%%%%%%%%%%%%%%%%%%%%%%
% Warning: The codes below are designed to be run in Matlab %
%          parallel computing mode. Running it in normal     %
%          mode may need more than 24 hours.                 %
%%%%%%%%%%%%%%%%%%%%%%%%%%%%%%%%%%%%%%%%%%%%%%%%%%%%%%

Rl_need = 50;
rl_num = 0;
for i = 1:length(Rl)
    if Rl(i)>=Rl_need
        if rl_num == 0
            rl_num = i;
        end
    end
end
BT5 = zeros(length(Pe2),length(B2));
EPB5 = zeros(length(Pe2),length(B2));
temp_limit = zeros(1,length(Pe2));
temp_s = zeros(1,length(Pe2));
temp_qmin = zeros(1,length(Pe2));
temp_t1 = zeros(1,length(Pe2));
temp_t2 = zeros(1,length(Pe2));
cutoff2 = 0;


if 1/(2*pi*Rl(rl_num)*Cd)<B2(length(B2))
        for l = 1:length(B2)
            if B2(l)>(1/(2*pi*Rl(rl_num)*Cd))
                if cutoff2 ==0
                cutoff2 = l;
                end
            end
        end
else
        cutoff2 = length(B2);
end
for i = 1:cutoff2
    parfor k = 1:length(Pe2)
        temp_t1(k) = 0;
        temp_t2(k) = 0;
        for j= 1:length(t)
        temp_mm = 0;
        if
radipattern(n1,Pe2(k),Ar,v,t(j),D1)*heth/(h*f*B2(i))>(sigma(rl_num,i)
*4.76)
```

```
            if temp_t1(k) == 0
                temp_t1(k) = t(j);
            end
        end
        if
radipattern(n1,Pe2(k),Ar,v,t(j),D1)*heth/(h*f*B2(i))>(sigma(rl_num,i)
*4.76*2.5)
            if temp_t2(k) == 0
                temp_t2(k) = t(j);
            end
        end
        end
    for j= 1:200
        temp_mm = 0;
            temp_mm =
radipattern(n1,Pe2(k),Ar,v,(temp_t1(k)+(temp_t2(k)-temp_t1(k))*j/200)
,D1)*heth/(h*f*B2(i));
            [temp_s(k),fval2] = fzero(@(s)
temp_mm*exp(s)+s*(sigma(rl_num,i)^2)-sigma(rl_num,i)*4.76-1/s,1);
            temp_qmin(k) =
exp(temp_mm*(exp(temp_s(k))-1)+(temp_s(k)^2)*(sigma(rl_num,i)^2)/2-te
mp_s(k)*sigma(rl_num,i)*4.76-log(abs(temp_s(k))))/((2*pi*(temp_mm*exp
(temp_s(k))+sigma(rl_num,i)^2+1/(temp_s(k)^2)))^0.5);
            if BT5(k,i) == 0
                if temp_qmin(k)<10^(-6)
                    BT5(k,i) =
abs(temp_t1(k)+(temp_t2(k)-temp_t1(k))*j/200)*2*B2(i);
                    EPB5(k,i) = Pe2(k)/B2(i);
                    break;
                end
            end
    end
    end
end

maxBT5 = zeros(1,length(Pe2));
maxB5 = zeros(1,length(Pe2));
Bneed5 = zeros(1,length(Pe2));
B2need5 = zeros(1,length(Pe2));
maxEPB5 = zeros(1,length(Pe2));
for i = 1:length(Pe2)
    for j = 1:length(B2)
        if BT5(i,j)>maxBT5(i)
            maxBT5(i) = BT5(i,j);
```

```
            maxB5(i) = B2(j);
            maxEPB5(i) = EPB5(i,j);
        end
        if Bneed5(i) == 0
            if BT5(i,j)>(20e3*20e-3)
                Bneed5(i) = B2(j);
            end
        end
        if B2need5(i) == 0
            if BT5(i,j)>(300*20e-3)
                B2need5(i) = B2(j);
            end
        end
    end
end
```

Deriving bit capacities from the transimpedance amplified front end

```
%%%%%%%%%%%%%%%%%%%%%%%%%%%%%%%%%%%%%%%%%%%%%%%%%%%%%%%%%%%
% Warning: The codes below are designed to be run in Matlab %
%          parallel computing mode. Running it in normal     %
%          mode may need more than 24 hours.                 %
%%%%%%%%%%%%%%%%%%%%%%%%%%%%%%%%%%%%%%%%%%%%%%%%%%%%%%%%%%%


cf = zeros(1,length(Rl));
gain4 = zeros(length(B2),length(Rl));
for i=1:length(Rl)
cf(i)=sqrt(Cd/(2*pi*Rl(i)*GBP));
end
for j = 1:length(Rl)
    for i = 1:length(B2)
    gain4(i,j) = abs(1/(1+1i*2*pi*B2(i)*Rl(j)*cf(j)));
    if gain4(i,j)<0.9
        gain4(i,j)=0;
    end
    end
    j
end

Rl_need = 5000;
```

```matlab
rl_num = 0;
for i = 1:length(Rl)
    if Rl(i)>=Rl_need
        if rl_num == 0
            rl_num = i;
        end
    end
end


EPB12 = zeros(length(Pe2),length(B2));
temp_limit = zeros(1,length(Pe2));
temp_s = zeros(1,length(Pe2));
temp_qmin = zeros(1,length(Pe2));
BT12 = zeros(length(Pe2),length(B2));
cutoff2 = 0;
if 1/(2*pi*Rl(rl_num)*cf(rl_num))<B2(length(B2))
        for l = 1:length(B2)
            if gain4(l,rl_num) == 0
                if cutoff2 == 0
                cutoff2 = l;
                end
            end
        end
    else
        cutoff2 = length(B2);
end
for i = 1:cutoff2
    parfor k = 1:length(Pe2)
    for j= 1:length(t)
        temp_mm = 0;
        if
radipattern(n1,Pe2(k),Ar,v,t(j),D1)*heth/(h*f*B2(i))>(sigma2(rl_num,i
)*4.76)
            temp_mm =
gain4(i,rl_num)*radipattern(n1,Pe2(k),Ar,v,t(j),D1)*heth/(h*f*B2(i));
            [temp_s(k),fval2] = fzero(@(s)
temp_mm*exp(s)+s*(sigma2(rl_num,i)^2)-sigma2(rl_num,i)*4.76-1/s,1);
            temp_qmin(k) =
exp(temp_mm*(exp(temp_s(k))-1)+(temp_s(k)^2)*(sigma2(rl_num,i)^2)/2-t
emp_s(k)*sigma2(rl_num,i)*4.76-log(abs(temp_s(k))))/((2*pi*(temp_mm*e
xp(temp_s(k))+sigma2(rl_num,i)^2+1/(temp_s(k)^2)))^0.5);
            if BT12(k,i) == 0
                if temp_qmin(k)<10^(-6)
                    BT12(k,i) = abs(t(j))*2*B2(i);
```

```
                    EPB12(k,i) = Pe2(k)/B2(i);
                    break;
                end
            end
        end
    end
    end
end
```

Analysis of the AGC amplifier

```
Out_range = zeros(length(Rl),length(B));
for i = 1:length(B)
    for j = 1:length(Rl)
        Out_range(j,i) =
10*log10(q*radipattern(n1,Pe,Ar,v,0,D1)*heth/(h*f*9.52*sigma(j,i)*B(i
)*q));
    end
end


K = logspace(5,13,1000);
Vcmax = 100;
Vout = zeros(length(B),length(Rl),length(t));
t_point = zeros(1,6);
V_delta = zeros(6,length(K));
Vout2 = zeros(length(K),length(t));
for ii = 1:6
    switch ii
        case 1,
        j = 1;
        i = 510;
        Vdef = v;
        case 2,
            j = 24;
            i = 471;
            Vdef = v;
        case 3,
            j = 67;
            i = 429;
            Vdef = v;
```

```
        case 4,
            j = 1;
            i = 510;
            Vdef = v*10;
        case 5,
            j = 24;
            i = 471;
            Vdef = v*10;
        case 6,
            j = 67;
            i = 429;
            Vdef = v*10;
    end
    Vin2 = radipattern(n1,Pe,Ar,Vdef,t,D1)*heth/(h*f)*q*Rl(j);
    for l = 1:length(K)
        for k = 1:length(t)
            if Vin2(k) < 12*sigma(j,i)*B(i)*q*Rl(j)
                Vout2(l,k) = Vin2(k)*Vcmax;
            else
                if t_point(ii) == 0
                    t_point(ii) = k-1;
                end
                Vout2(l,k) =
(Vin2(k)-Vin2(k-1))/(Vin2(k-1))*exp(-K(l)*Vin2(k-1)*(t(k)-t(t_point(i
i))))*Vout2(l,k-1)+Vout2(l,k-1);
                if Vout2(l,k)< Vin2(k)*(Vcmax/1000)
                    Vout2(l,k) = Vin2(k)*(Vcmax/1000);
                end
            end
        end
        V_delta(ii,l) =
10*log10(max(Vout2(l,(t_point(ii)+3):(length(t)-1-t_point(ii)-3)))/mi
n(Vout2(l,((t_point(ii)+3):(length(t)-1-t_point(ii)-3)))));
    end
end
```

Functions for calculating power from the Lambertian pattern in the

model and in the experimental setup

```
function [Pr]=radipattern(n,Pe,Ar,v,t,D)
```

```
Pr =
((n+1).*Pe.*Ar.*(D.^(n+1)))./((((D.^2)+((v*t).^2)).^((n+3)/2)).*2*pi)
;


function [PR_em] = radipattern_em(n,Pe,Ar,v,t,D,D_d,d_d)
syms Phi  Phi_0;
Pr_em = (n+1)/(2*pi*D)*Pe*sqrt(Ar)*(cos(Phi))^(n+3);
PR_em = zeros(1,length(t));
for i = 1:length(t)
    if
(atan((v*t(i)+d_d/2)/D_d)>atan(-sqrt(Ar)/(2*D)))&&(atan((v*t(i)-d_d/2
)/D_d)<atan(sqrt(Ar)/(2*D)))
        if
(atan((v*t(i)+d_d/2)/D_d)<atan(sqrt(Ar)/(2*D)))&&(atan((v*t(i)-d_d/2)
/D_d)>atan(-sqrt(Ar)/(2*D)))
            PR_em(i) =
abs(int(Pr_em,Phi,atan((v*t(i)+d_d/2)/D_d),atan((v*t(i)-d_d/2)/D_d)))
;
        else
            if atan((v*t(i)+d_d/2)/D_d)<=atan(sqrt(Ar)/(2*D))
                PR_em(i) =
abs(int(Pr_em,Phi,atan((v*t(i)+d_d/2)/D_d),atan(-sqrt(Ar)/(2*D))));
            else
                PR_em(i) =
abs(int(Pr_em,Phi,atan(sqrt(Ar)/(2*D)),atan((v*t(i)-d_d/2)/D_d)));
            end
        end
    end
end
```

Appendix III Transimpedance Amplifier Model and Simulation

Recalling Fig. 3.2.6 and introducing one more parameter that the voltage of Op-amp inversed input is $-\frac{U_o}{A}$ is Fig. A.1, which yields the current function of the inversed input:

$$\frac{U_o + \frac{U_o}{A_{OL}}}{Z_f} = I - \frac{sC_dU_o}{A_{OL}} \tag{A.8}$$

in which:

$$Z_f = \frac{R_f}{1 + sR_fC_f} \tag{A.9}$$

Inserting (A.9) into (A.8) derives a function as follows:

$$U_o = I\left(\frac{A_{OL}}{1 + A_{OL}}\right)\left(\frac{R_f}{1 + sR_fC_f} - \frac{sC_dU_o}{A_{OL}} \cdot \frac{R_f}{1 + sR_fC_f}\right) \tag{A.10}$$

If the part $\frac{sC_dU_o}{A_{OL}} \cdot \frac{R_f}{1+sR_fC_f}$ is not significant and can be ignored due to the effect of A_{OL}, the rest of (A.10) forms (3.2.18). And for the second order transfer function, the gain of the transimpedance amplifier from (A.10) is:

$$\frac{U_o}{I} = R_f \cdot \frac{A_{OL}}{1 + A_{OL} + A_{OL}sR_fC_f + sR_f(C_f + C_d)} \tag{A.11}$$

Inserting (3.2.24) into (A.11), the second order transfer function becomes:

$$\frac{U_o}{I} = R_f \cdot \frac{\omega_o^2}{s^2 + s\frac{\omega_o}{Q} + \omega_o^2}$$

$$= R_f$$

(A.12)

$$\cdot \frac{\frac{A_0\omega_p}{R_f(C_f + C_d)}}{s^2 + s\left[\omega_p\left(1 + \frac{A_0 C_f}{C_f + C_d}\right) + \frac{1}{R_f(C_f + C_d)}\right] + \frac{(A_0 + 1)\omega_p}{R_f(C_f + C_d)}}$$

Let A_0 in $\frac{A_0\omega_p}{R_f(C_f+C_d)}$ approximate $A_0 + 1$, ω_o and Q can be derived from (A.12).
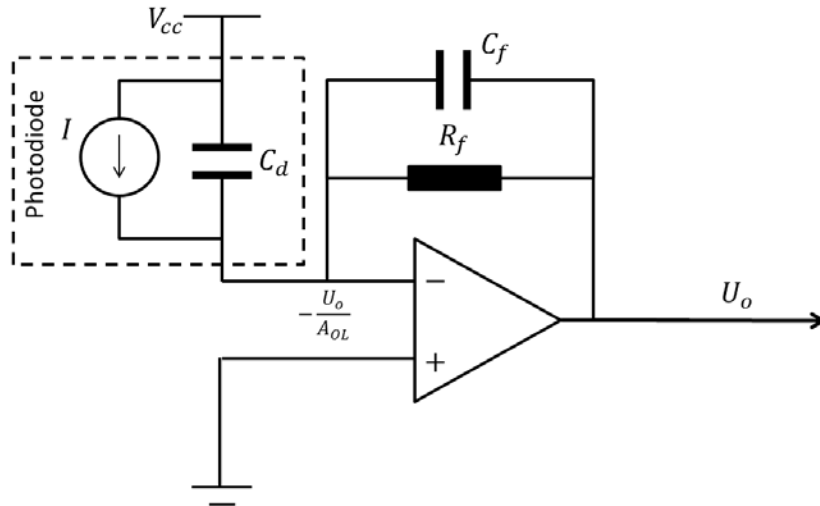
Fig. A.2 The transimpedance amplifier model with $-\frac{U_o}{A}$.

The results in Fig. 3.2.8 are generated from the circuit simulation of the model in Fig. A.1 using Multisim, the setup of which is shown in Fig. A.2. The photodiode signal is generated from the combination of a current signal source and a capacitor, which represents a 10 uA photodiode signal current and a diode capacitor of 11 pF. The rest of the circuit is formed as an actual transimpedance amplifier, in which the Op-amp is OPA842 that the GBW is at 200 MHz. For $R_L = 50$ kΩ C_f from (3.2.23) and (3.2.27) are at 0.42 pF and 0.60 pF.
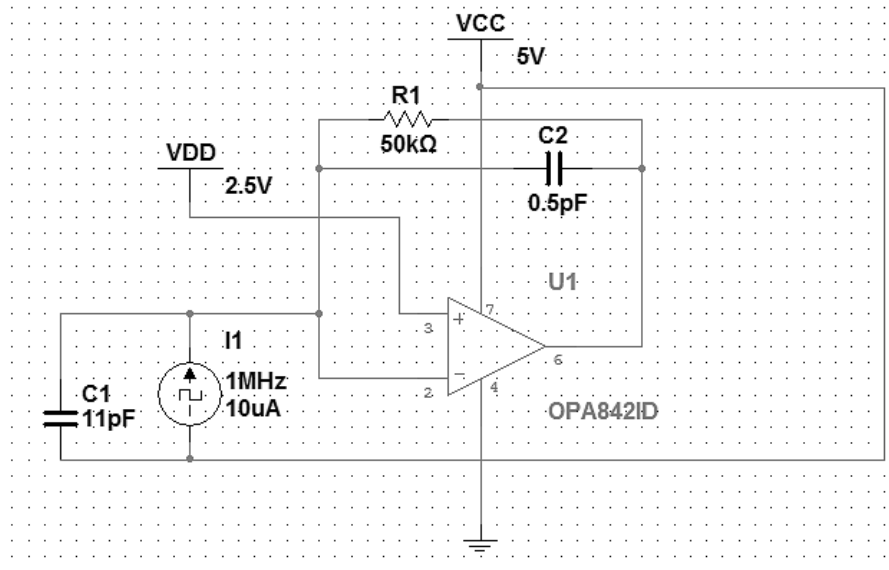
Fig. A.3 The circuit simulation of transimpedance amplifier in Multisim.

Appendix IV   The   Motor   System   Design   of   the   Experimental Setup in Solidworks

The motor system is shown in Fig. A.4, which was designed by Seb Dangerfield.
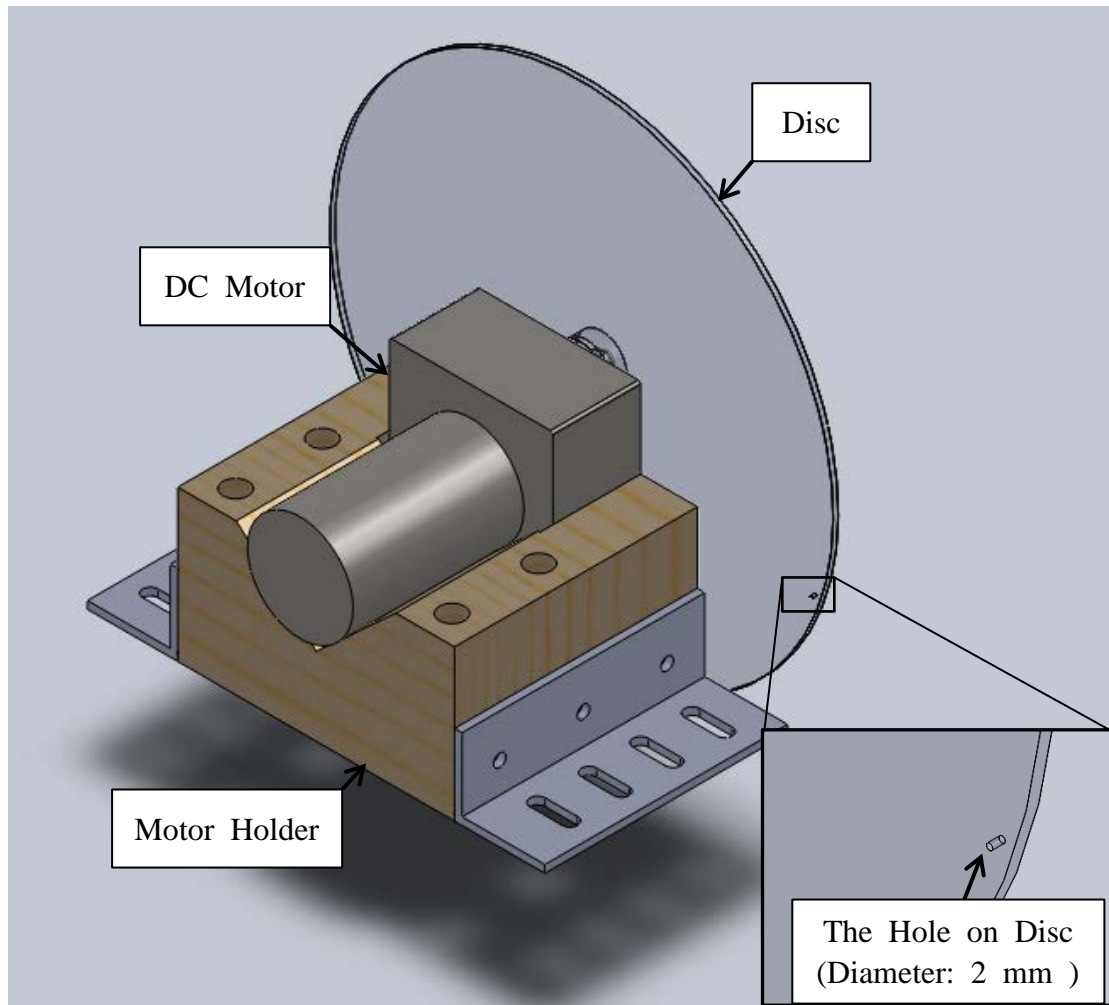
Fig. A.4 The Solidworks motor experimental setup

Appendix V C Source Code Samples of the Programs on MSP430

MSP430 initialization

```c
/***********************************************************/
//                        MSP430F2418
//                        -----------------
//                       |                 |
//                       |                 |
//      IR Circuit Output -->|P1.2        P1.3|--> IR Circuit Input
//      IR Circuit Output -->|P4.1        P4.3|--> IR Circuit Input
//                       |                 |
/***********************************************************/

#include "msp430x241x.h"

void main(void)
{
  WDTCTL = WDTPW + WDTHOLD; //stop the watchdog timer to prevent system rest
  if (CALBC1_16MHZ ==0xFF || CALDCO_16MHZ == 0xFF)
  {
    while(1);                              // If calibration constants erased
                                           // do not load, trap CPU!!
  }
/* DCO clock calibration data loaded*/
  DCOCTL = CALDCO_16MHZ;
  BCSCTL1 = CALBC1_16MHZ;

  P1OUT=0x00;   // termination of unused pins
  P1DIR=0xFB;   // P1.0=LED#1, P1.2=CCR1A input
  P2OUT=0x00;
  P2DIR=0xFF;
  P3OUT=0x00;
  P3DIR=0xFF;
  P4OUT=0x00;
  P4DIR=0xFD;   // P4.1 = CCR1B input, P4.3 = CCR3B Output
  P5OUT=0x00;
  P5DIR=0xFF;
  P6OUT=0x00;
  P6DIR=0xFF;

/* Disable P1 and P2 interrupt*/
```

```
    P1IES=0x00;
    P1IE=0x00;
    P2IES=0x00;
    P2IE=0x00;

    BCSCTL2 = SELM_0+DIVM_0+DIVS_0;      //MCLK=SMCLK=DCO=16Mhz
    TACCTL1 = CM_1+CAP+SCS;              //Capture on rising edge, input P1.1 CCI1A
    TBCCTL1 = CM_2+CAP+SCS;              //Capture on falling edge, input P4.0 CCI1B
    TACTL = TASSEL_2+MC_1+TACLR;                     // TimerA on SMCLK, cont-mode,
clear
    TBCTL = TBSSEL_2+MC_1+TBCLR;    //TimerB on SMCLK, off, clear
    TACCR0 = 0;
    TBCCR0 = 0;

    Delay();
    P1SEL = 0x0C;   //P1.2=Timer A capture input, P1.3=Timer A output
    P4SEL = 0x0A;   //P4.1=Timer B capture input, P4.3=Timer B output
    while (1)
    {} // Main program in side, not included
}


----------------------------------------------------------------------------------------------------------------


/**********************************************************/
//                           MSP430F449
//                          -----------------
//                         |                 |
//                         |                 |
//        IR Circuit Output -->|P1.2         P2.2|--> IR Circuit Input
//        IR Circuit Output -->|P2.0         P2.3|--> IR Circuit Input
//                         |                 |
/**********************************************************/
#include "msp430F449.h"
void main( void )
{
    // Stop watchdog timer to prevent time out reset
    WDTCTL = WDTPW + WDTHOLD;
    // Set frequency to 8MHz
    FLL_CTL0 |= DCOPLUS + XCAP18PF;                  // DCO+ set, freq = xtal x D x N+1
    SCFI0 |= FN_4;                                   // x2 DCO freq, 8MHz nominal DCO
    SCFQCTL = 121;                                   // (121+1) x 32768 x 2 = 7.99 MHz

    P1OUT=0x00;   // termination of unused pins
    P1DIR=0xFF;   // P1.0=LED#1, P1.2=CCI1A input
```

```
    P2OUT=0x00;
    P2DIR=0xFF;
    P3OUT=0x00;
    P3DIR=0xFF;
    P4OUT=0x00;
    P4DIR=0xFF;
    P5OUT=0x00;
    P5DIR=0xFF;
    P6OUT=0x00;
    P6DIR=0xFF;

    P1IES=0x00;
    P1IE=0x00;
    P2IES=0x00;
    P2IE=0x00;

    P2SEL = 0x09;   //P1.2=Timer A capture input, P1.3=Timer A output
//  P4SEL = 0x06;   //P4.1=Timer B capture input, P4.2=Timer B output


    TACTL = TASSEL_2+MC_1+TACLR;
    TBCTL = TBSSEL_2+MC_1+TBCLR;
    while (1)
    {} // Main program in side, not included
}
```

Trigger control programs in DDI demonstration

Trigger without DDI:

```
void main(void)
{
/***********************************************************/
// Controller initialization not included
/***********************************************************/
  while (1)                              if(TBCCTL1 & CCIFG)
  {                                      {
    TACCR0 = 0x51;                         TAR = 4;
    TBCCR0 = 0xA3;                         TBCCTL1 &= ~(CCIFG+COV);
    TACCR2 = 0x01;                         TBR = 0x7C;
    TBCCTL1 &= ~(CCIFG+COV);               TACTL &= ~TAIFG;
    while(1)                               TBCTL &= ~TBIFG;
    {                                      TACCTL2 = OUTMOD_4;
```

```
        TBCCTL1 &= ~CCIFG;                              if(bit_count==8)
        while(!(TBCTL & TBIFG));                          {
        {}                                                  TAR = 0x29;
        TBCTL &= ~TBIFG;                                    TBR = 0x22;
        while(!(TBCTL & TBIFG));                            bit_count = 0;
        {                                                  }
          if(TBCCTL1 & CCIFG)                          }
          {                                          }
            TBCCTL1 &= ~CCIFG;                      TACCTL2 = 0;
            bit_count++;                          }
            while(!(TBCTL & TBIFG))             }
            {}                                 }
            TBCTL &= ~TBIFG;               }
```

Trigger with DDI

```
void main(void)
{
/*************************************************************/
// Controller initialization not included
/*************************************************************/
   while (1)
   {
      if (win_open == 0)
      {
         Pulse_FilterDT16();
      }
      else
      {
         Trigger();
      }
   }
}


void Trigger(void)
{                                              {
   bit_count = 0;                                 TBCCTL1 &= ~(CCIFG+COV);
   TACCR2 = 0x01;                                 TBR = TAR + 0xA0;
   TACCR0 = 0xA3;                                 TBCTL &= ~TBIFG;
   TBCCTL1 = CM_3+CAP+SCS;                        pulse_start = TACCR1;
   TACCTL1 &= ~CCIFG;                             TAR = TAR - pulse_start;
   while(win_open)                                TACCTL2 = OUTMOD_4;
   {                                              TACCTL1 &= ~CCIFG;
      if(TACCTL1 & CCIFG)                         while(!(TBCCTL1 & CCIFG))
```

```
      {
        if(TBCTL & TBIFG)
        {
          win_open = 0;
          break;
        }
      }
      TBCCTL1 &= ~CCIFG;
      pulse_stop = TBCCR1;
      while(!(TBCTL & TBIFG))
      {}
      TBCTL &= ~TBIFG;
      TBCCR0 = 0xA3;
      while(win_open)
      {
        while(!(TBCCTL1 & CCIFG))
        {
          if(TBCTL & TBIFG)
          {
            win_open = 0;
            break;
          }
        }
        TBCCTL1 &= ~CCIFG;
        if (P4IN & 0x02)
        {
          pulse_start = TBCCR1;
        }
        else
        {
          win_open = 0;
          break;
        }
        while(!(TBCCTL1 & CCIFG))
        {
          if(TBCTL & TBIFG)
          {
            win_open = 0;
            break;
          }
        }
        TBCCTL1 &= ~CCIFG;
        if (!(P4IN & 0x02))
        {

            pulse_stop = TBCCR1;
          }
          else
          {
            win_open = 0;
            break;
          }
          if
((pulse_stop-pulse_start)<(pulse_width-0x0
5))
          {
            win_open = 0;
            break;
          }
          else
          {
            while(!(TBCTL & TBIFG))
            {}
            TBCTL &= ~TBIFG;
            bit_count++;
          }
        }
        if(bit_count==8)
        {
          while(!(TBCCTL1 & CCIFG))
          {
            if(TBCTL & TBIFG)
            {
              win_open = 0;
              break;
            }
          }
          TAR = 12;
          TBCCTL1 &= ~CCIFG;
          while(!(TBCCTL1 & CCIFG))
          {
            if(TBCTL & TBIFG)
            {
              win_open = 0;
              break;
            }
          }
          TBR = 0x94;
          TBCCTL1 &= ~CCIFG;
          while(!(TBCTL & TBIFG))
```

```
        {}                                          }
        TBCTL &= ~TBIFG;                        }
        bit_count = 0;                          TACCTL2 = 0;
      }                                         TBCCTL1 = CM_2+CAP+SCS;
    }                                       }
```

Software latches of DT and DR under the protocol

```
void main(void)
{
/***********************************************************/
// Controller initialization not included
/***********************************************************/
   while (1)
   {
     if (win_open == 0)
     {
       Pulse_FilterDT16();
...

void Pulse_FilterDR16(void)
{                                             if (TACCTL1 & CCIFG)
  TBCCTL3 = OUTMOD_4;                          {
  TBCCR3 = 0x45;                                 pulse_start = TACCR1;
  TBCCR0 = 0x51;                                 TAR = TAR - pulse_start;
  while(win_open == 0)                           TBCTL                    =
  {                                       TBSSEL_2+MC_1+TBCLR;
    if(TBCTL & TBIFG)                            TACCTL1 &= ~CCIFG;
    {                                            TACCR0 = 0xA3;
      bit_count++;                               TACTL &= ~TAIFG;
      TBCTL &= ~TBIFG;                           win_stable = 6;
    }                                            while(!(TBCCTL1 & CCIFG))
    if(bit_count==17)                            {
    {                                              if(TACTL & TAIFG)
      TBCCTL3 = 0;                                 {
      TACCR0 = 0x1DF;                                win_stable--;
      TBCCR0 = 0x1DF;                                TBCCR1 = 0x51;
      TACCTL1 &= ~(COV+CCIFG);                       break;
      TBCCTL1 &= ~(COV+CCIFG);                     }
      while (!(TBCTL & TBIFG))                    }
      {                                          TBCCTL1 &= ~CCIFG;
```

```
pulse_stop = TBCCR1;
TBR = TBR - pulse_stop;
TBCCR0 = 0xA3;
TBCTL &= ~TBIFG;
bit_count = 6;
while(!(TACTL & TAIFG))
{}
TACTL &= ~TAIFG;
while (!(TACCTL1 & CCIFG))
{
   if(TACTL &TAIFG)
   {
      win_open = 0;
      break;
   }
}
TACCTL1 &= ~CCIFG;
phase_switch = TACCR1;
if (phase_switch <= 0x14)
{
   bit_order = 0x00;
}
else
{
   if (phase_switch <= 0x28)
   {
      bit_order = 0x01;
   }
   else
   {
      if (phase_switch <= 0x3C)
      {
         bit_order = 0x02;
      }
      else
      {
         bit_order = 0x03;
      }
   }
}
while (!(TBCCTL1 & CCIFG))
{
   if (TACTL &TAIFG)
   {
         win_open = 0;
         break;
      }
   }
}
TBCCTL1 &= ~CCIFG;
if (TBCTL & TBIFG)
{
   TBCTL &= ~TBIFG;
   if (phase_switch > TBCCR1)
   {
      if    ((phase_switch -
TBCCR1) > 0x05)
      {
         win_stable--;
      }
   }
   else
   {
      if    ((TBCCR1 -
phase_switch) > 0x05)
      {
         win_stable--;
      }
   }
}
else
{
   win_open = 0;
   bit_count = 0;
}
while (bit_count)
{
   if (TACTL & TAIFG)
   {
      TACTL &= ~TAIFG;
      while    (!(TACCTL1    &
CCIFG))
      {
         if(TACTL &TAIFG)
         {
            win_open = 0;
            break;
         }
      }
```

```c
TACCTL1 &= ~CCIFG;
phase_switch = TACCR1;
if (phase_switch <= 0x14)
{
  bit_data<<=2;
  bit_data |= 0x00;
}
else
{
  if (phase_switch <= 0x28)
  {
    bit_data<<=2;
    bit_data |= 0x01;
  }
  else
  {
    if (phase_switch <= 0x3C)
    {
      bit_data<<=2;
      bit_data |= 0x02;
    }
    else
    {
      bit_data<<=2;
      bit_data |= 0x03;
    }
  }
}
while (!(TBCCTL1 & CCIFG))
{
  if (TACTL &TAIFG)
  {
    win_open = 0;
    break;
  }
}
TBCCTL1 &= ~CCIFG;
if (TBCTL & TBIFG)
{
  TBCTL &= ~TBIFG;
  if (phase_switch > TBCCR1)
  {
    if ((phase_switch - TBCCR1) > 0x05)
    {
      win_stable--;
      bit_count--;
    }
    else
    {
      bit_count--;
    }
  }
  else
  {
    if ((TBCCR1 - phase_switch) > 0x05)
    {
      win_stable--;
      bit_count--;
    }
    else
    {
      bit_count--;
    }
  }
}
else
{
  win_open = 0;
  bit_count = 0;
}
}
}
if (win_stable == 6)
{
  win_open = 1;
  rec_data = bit_data;
  if(er_flag==2)
  {
    trans_data = 0;
  }
  else
  {
```

```
            trans_data = bit_order;
        }
        TACCR0 = 0x51;
        TAR = 0;
        TBCCR0 = 0xF5;
        TACTL &= ~TAIFG;
        TBCTL &= ~TBIFG;
        TACCR2 = 0x01;
        TBR = TAR;
        TBR = TBR+3;
        TACCTL2 = OUTMOD_4;
        while(1)
        {
          if (TACTL & TAIFG)
          {
            TACTL &= ~TAIFG;
            if (trans_data & 0x01)
            {
              if (trans_data & 0x02)
              {
                TBCCR3 = 0x48;
              }
              else
              {
                TBCCR3 = 0x22;
              }
            }
            else
            {
              if (trans_data & 0x02)
              {
                TBCCR3 = 0x35;
              }
              else
              {
                TBCCR3 = 0x0B;
              }
            }
            TBCCTL3 = OUTMOD_4;
            while(!(TACTL & TAIFG))
            {}
            TACTL &= ~TAIFG;
            TACCR0 = 0xF5;
            TBCTL &= ~TBIFG;
            while (!(TBCTL & TBIFG))
            {}
            TBCCR0 = 0x51;
            TBCTL &= ~TBIFG;
            pulse_start = TBCCR3;
            TACCR2 = pulse_start;
            while (!(TBCTL & TBIFG))
            {}
            TBCTL &= ~TBIFG;
            TBCCR0 = 0xF5;
            while(!(TACTL & TAIFG))
            {}
            TACTL &= ~TAIFG;
            TACCR0 = 0x51;
            TBCCR3 = 0x13F;
            while(!(TACTL & TAIFG))
            {}
            TACTL &= ~TAIFG;
            TACCR0 = 0xF5;
            while (!(TBCTL & TBIFG))
            {}
            TBCCTL3 = 0;
            TACCTL2 = 0;
            TACCTL1 &= ~CCIFG;
            TACCR0 = 0x3C0;
            TBCCR0 = 0x3C0;
            if ((bit_order=ex_order))
            {
              er_flag = 0;
              switch(ex_order)
              {
                case(0x01):
                ex_order = 0x02;
```

```
                    break;                                        er_flag++;
                case(0x02):                                   }
                  ex_order = 0x03;                          if(er_flag == 2)
                  break;                                       {
                case(0x03):                                    if(bit_order==0)
                  ex_order = 0x01;                              {
                  break;                                            ex_order = 0x01;
                }                                                  er_flag = 0;
              }                                                 }
            else                                             }
            {                                              }
              if(ex_order==0)                                 break;
              {                                          }
                switch(bit_order)                      }
                {                                     }
                  case(0x01):                       }
                    ex_order = 0x02;              }
                    break;                      if(win_open ==0)
                  case(0x02):                   {
                    ex_order = 0x03;              TBCCTL3 = OUTMOD_4;
                    break;                        TBCCR0 = 0x51;
                  case(0x03):                     bit_count = 0;
                    ex_order = 0x01;              TACCR0 = 0;
                    break;                      }
                }                             }
              }                             }
            else                          }
            {

void main(void)
{
/*************************************************************/
// Controller initialization not included
/*************************************************************/
   while (1)
   {
      if (win_open == 0)
      {                 //pulse then jump to pulse operation.
         TACTL &= ~TAIFG;
         while(1)
         {
            if (TACCTL1 & CCIFG)
            {
               break;
```

```
        }
    }
    Pulse_FilterDT8();
…

void Pulse_FilterDT8(void)
{
  TACCR0 = 0x9F;
  TACTL = TASSEL_2+MC_1+TACLR;
  TACCTL1 &= ~(COV+CCIFG);
  while(((TACTL                    &
TAIFG)|win_open)==0)
  {
    if (TACCTL1 & CCIFG)
    {
      TACCTL1 &= ~CCIFG;
      pulse_start = TACCR1;
      TAR = TAR - pulse_start;
      TBCCR0 = 0x9F;
      TBCCTL1 &= ~(COV+CCIFG);
      while(!(TBCCTL1 & CCIFG))
      {}
      if (TACCTL1 & CCIFG)
      {
        TACCR0 = 0xEF;
        TACTL                      =
TASSEL_2+MC_1+TACLR;
        TBCCR0 = 0;
        TACCTL1 &= ~(COV+CCIFG);
        TBCCTL1 &= ~(COV+CCIFG);
        break;
      }
      else
      {
        TBCCTL1 &= ~CCIFG;
        pulse_stop = TBCCR1;
        TBR = TBR - pulse_stop;
        while(!(TACTL & TAIFG))
        {
          if (TACCTL1 & CCIFG)
          {
            TACCTL1 &= ~CCIFG;
            pulse_start = TACCR1;
            TAR = TAR - pulse_start;

            while(!(TBCCTL1        &
CCIFG))
            {}
            if (TACCTL1 & CCIFG)
            {
              TACCR0 = 0xEF;
              TACTL                =
TASSEL_2+MC_1+TACLR;
              TBCCR0 = 0;
              TACCTL1              &=
~(COV+CCIFG);
              TBCCTL1              &=
~(COV+CCIFG);
              break;
            }
            TBCCTL1 &= ~CCIFG;
            pulse_stop = TBCCR1;
            TBR = TBR - pulse_stop;
            if (pulse_start>0x38)
            {
              if    (pulse_start    >=
pulse_stop)
              {
                if    (((pulse_start    -
pulse_stop) <= 0x03))
                {
                  win_open = 1;
                  break;
                }
                else
                {
                  TACCR0 = 0xEF;
                  TBCCR0 = 0;
                  break;
                }
              }
              else
              {
```

```
                    if      (((pulse_stop          -
pulse_start) <= 0x03))
                      {
                        win_open = 1;
                        break;
                      }
                      else
                      {
                        TACCR0 = 0xEF;
                        TBCCR0 = 0;
                        break;
                      }
                  }
                }
            break;
              }
          }
        }
      }
    }
}
```